HYDROGEN EFFECTS ON DISLOCATION STRUCTURES AND INTERACTIONS

A Dissertation
Presented to
The Academic Faculty

By

Luke L. Costello

In Partial Fulfillment
of the Requirements for the Degree
Doctor of Philosophy in the
School of Mechanical Engineering

Georgia Institute of Technology

December 2020

HYDROGEN EFFECTS ON DISLOCATION STRUCTURES AND INTERACTIONS

Approved by:

Dr. David L. McDowell, Advisor
George W. Woodruff School of Mechanical Engineering
Georgia Institute of Technology

Dr. Ting Zhu
George W. Woodruff School of Mechanical Engineering
Georgia Institute of Technology

Dr. Richard Neu
George W. Woodruff School of Mechanical Engineering
Georgia Institute of Technology

Dr. Remi Dingreville
Center for Integrated Nanotechnologies
Sandia National Laboratories

Dr. Gustavo Castelluccio
School of Aerospace, Transport and Manufacturing
Cranfield University

Date Approved: November 18, 2020

ACKNOWLEDGEMENTS

This work would not have been possible without the generous support and guidance of my advisor Professor David L. McDowell. His broad vision and advice have shown me what is possible in the wider world of research. I would also like to acknowledge my committee members Professor Ting Zhu, Professor Richard Neu, Dr. Remi Dingreville, and Professor Gustavo Castelluccio who have been invaluable collaborators, instructors, and mentors throughout this experience. I also thank my lab mates, past and present, Dr. Shuozhi Xu, Dr. Matthew Priddy, Dr. Shreevant Tiwari, Dr. Dengke Chen, Dr. Tang Gu, Dr. Aaron Tallman, Adrienne Muth, Kris Stopka, Gary Whelan, Ted Zirkle, Alex Selimov, and Kevin Chu who have made this experience all the better.

This work has been generously supported by Fluor Marine Propulsion, LLC (Naval Nuclear Laboratory). I particularly thank Dr. Clint Geller and Dr. Benjamin Anglin for their open minded leadership of the overall research program. This program has fostered engaging collaborations across universities and I thank my colleagues at Purdue University, particularly Professor Anter El-Azab and Dr. Peng Lin.

Lastly I thank my family and friends, particularly my parents, my brothers; Zak and Blaine, Matt, Alex, Max and Sara, and especially my partner Claire for her enthusiastic and unrelenting support.

TABLE OF CONTENTS

LIST OF TABLES

LIST OF FIGURES

SUMMARY

Hydrogen embrittlement (HE) is a complex process, in which the interactions of H atoms, vacancies, and dislocations lead to a macroscopic loss of ductility. Although this phenomenon is commonly observed, its microscopic origins remain unclear. In this thesis we study the process of HE, starting from the microscale, using atomistic simulations and modeling to connect with higher length scales. Passing information from physically realistic atomic scale simulations allows for improved understanding of the underlying mechanisms of H embrittlement and specifically how effects attributed to H contribute at the meso and macroscale. We begin by studying the direct interaction of H with dislocations. A method for computing the distribution of H around an edge dislocation is presented and compared to an alternative approach. The presented method is then exercised in an example, studying the effect of H on the stacking fault width (SFW) of an extended edge dislocation. It is shown that H acts to decrease the SFW. Further, only the H very locally around and inside the dislocation cores and stacking fault contribute significantly to the observed decrease in the SFW.

In addition to dislocations, H interacts significantly with vacancies and can act to lower their formation energy. Vacancies are produced in concentrations far greater than equilibrium values in regions of high plastic deformation. Inspired by a model which attributes the production of excess vacancies to dislocation-dislocation interaction is persistent slip bands (PSBs) we develop a vacancy balance model for the production of excess vacancies which is integrated in a macroscopic crystal plasticity finite element (CP-FEM) framework. The CP-FEM simulations are exercised to study the role of vacancy production around a blunted fatigue crack. The production of excess vacancies results in a competition between dominant modes of H transport, with transport being dominated by dislocation pipe diffusion in the low vacancy concentration regime and by the vacancy trapping effect in the high vacancy concentration regime. Lastly, we study the role of H on nanovoid nucleation.

Methods for computing the formation energy and structures of small vacancy clusters (up to 15 vacancies) and large voids (up to 500 vacancies), both with H, are presented. It is found that H lowers the formation energy for vacancy clusters. For large voids the decrease in formation energy due to H can be modeled through the H effect on the void surface energy. This H-effected surface energy can be integrated into mesoscopic simulations as a way of incorporating H effects into the void nucleation criterion. It is also used to calculate the critical void nucleation size. The critical size decreases with increasing H. At high H concentrations the critical void size becomes sufficiently small to allow for spontaneous void nucleation implying that in macroscopic simulations only void growth need be considered.

CHAPTER 1
INTRODUCTION

Hydrogen embrittlement (HE) has been a long standing problem in physical metallurgy with works dating back to the 1870s [1, 2]. Generally, HE refers to a decrease in ductility due to the presence of H. Particular emphasis has been placed on associated effects on the decrease of fracture toughness and fatigue crack growth resistance. The underlying microscopic mechanisms governing the HE response remain unclear. Several possible mechanisms have been proposed and these mechanisms as well as their potential validity have been discussed in detailed reviews [3, 4]. Perhaps the most prominently studied mechanism is the hydrogen enhanced localized plasticity (HELP) mechanism [5]. The HELP mechanism is based on a few important experimental observations. It was observed in α-Ti that with H present dislocation velocity tends to increase [6]. Notably, this process is reversible, and when H is removed from the system the dislocation velocity returns to normal. In another experiment [7] on 310S stainless steel, H played the role of reducing the interaction between dislocations leading to a decrease in the spacing between neighboring dislocations in pileups. In yet another experiment [8], in austenitic stainless steel, it is inferred through an observed increase in stacking fault width that H lowers the stacking fault energy in extended dislocations. The HELP mechanism holds that H acts through its direct interaction with dislocations, leading to increases in dislocation mobility and decreased interaction between dislocations and other obstacles.

Along with HELP, hydrogen enhanced decohesion (HEDE) [9] has been studied thoroughly as another possible mechanism. HEDE posits that H acts to lower the bond strength between layers of metal atoms, lowering the energy barrier for decohesion. For example, H trapped in a grain boundary will lower the bonding strength across the boundary, promoting fracture along such a boundary. For H segregating into the high stress region

ahead of a crack tip, the decreased bond strength may promote crack growth. Unlike the HELP mechanism, it is difficult to measure the effects of HEDE experimentally; it is not currently possible to resolve the positions of H with available experimental methods. However, attempts have been made to infer the HEDE type effects on intergranular fracture from experimental data using S impurities instead of H [10] by studying fracture surfaces.

Over the last 20 years a significant body of research has emerged, indicating that H does not always act alone in HE effects. Instead it has been suggested that H-vacancy complexes can play a significant role [11]. Alongside this observation, during heavy plastic deformation, concentrations of vacancies much greater than equilibrium levels are produced [12, 13, 14]. Following these observations, hydrogen enhancement of the strain-induced generation of vacancies (HESIV) [15, 16] has been proposed. HESIV holds that the high concentrations of vacancies generated by plasticity are enhanced with H present [17], and that the effect of the resultant damage accumulation is consistent with experimental observations [16]. Compounding this effect, it has been observed in a variety of metals that H can lower the formation energy of vacancies, thereby stabilizing these high vacancy concentrations [18, 19, 20]. Unlike HELP and HEDE, HESIV considers the interaction between vacancies and H to play a significant role in HE with dislocations driving the production of excess vacancies.

A significant limitation in the study of HE mechanisms has been length scales accessible to experimental measurements. It is not currently possible to measure the spatial distribution of small atoms, like H in a crystal, nor is it possible to measure details of the mesoscopic features (like the distribution of dislocation sources in a wall). Specific mechanisms occurring at the microscale can often only be inferred from measurements and cannot be directly observed. Detailed computation is often the only way of directly testing the hypotheses put forth by proposed mechanisms. A wide variety of computational methods have been applied to study HE mechanisms including density functional theory (DFT) [21, 22], molecular dynamics (MD), molecular statics (MS), and a variety of

Monte Carlo (MC) methods [23]. Significantly, MD simulations have been used to study the HELP mechanism [24] in α-Fe. They found that in the presence of H, there is no observable change in the spacing between dislocations in a pile up, contradicting the HELP mechanism. On the other hand, the HEDE mechanism has been studied using atomistic simulations in both grain boundaries [25] and around a crack tip [26], finding that H can reduce the bonding strength between atomic layers along planes in a lattice, supporting the HEDE mechanism. Addressing the lack of experimental capability to observe atomic H in a metal lattice, atomistic simulation tools and modeling approaches have been leveraged to study the thermodynamic details of the distribution of H in the elastic field of a dislocation [27, 28]. Finally, the production of excess vacancies can be modeled in persistent slip bands (PSBs) [29] and the role of H on lowering the formation energy of single and di vacancies has been demonstrated in density functional theory (DFT) calculations [30, 31, 32, 33]. While the production of excess vacancies has been studied in PSBs, the same logic can be applied to other structures consisting of dislocation rich (and thus dislocation source rich) regions separated by dislocation sparse regions. This work is concerned with refined, cellular microstructures which are formed in high stress regions in FCC crystals under cyclic loads and we apply these concepts developed for PSBs to this system. Together these works emphasize the critical role of atomic scale simulation in understanding HE and filling gaps where experiments cannot probe. Inspired by this foundation of atomistic modeling, in this thesis we leverage atomistic simulation techniques along with model development to study the processes underlying HE.

We focus first on studying the distribution of atomic H around dislocations but note that this technique is general and allows for sampling H distribution on interstitial sites. Following this, we focus on the production of excess vacancies and the role of H on formation energy of vacancy clusters. In Chapter 2 we begin by addressing the distribution of H in the elastic field of an extended dislocation. A sampling method based on the binding energy of H to sites around the dislocation is introduced and applied to study the effect of the H

field on the core structure of an extended edge dislocation, enabling the observation of a system which is otherwise not measurable. In chapter 3 we turn our attention to vacancies. Chapter 3 develops a model for the production of excess vacancies in PSBs which is designed with the purpose of being used upscale in a crystal plasticity finite element model (CP-FEM) [34]. This allows for the integration of vacancy production (as a new module) into an existing FEM framework. Lastly, Chapter 4 connects the effects of H with the production and clustering of vacancies by integrating H effects through computational studies of the formation energy and geometric structure of both small and large H-vacancy clusters. This information is then intended to pass to mesoscale dislocation dynamics simulations to enable the integration of H effects into nanovoid nucleation.

The body of work in this thesis supports a broader research program, Environmentally Influenced Crack Evolution Modeling (EICEM), sponsored by Fluor Marine Propulsion, LLC (Naval Nuclear Laboratory), aimed at the development of predictive design tools for quantifying HE effects on fatigue crack growth in autenitic stainless steels. The EICEM program integrates research thrusts across a wide range of scales, from interatomic potential development up to fatigue crack propagation. The overarching goal of the work in this thesis and the role of this work within the broader EICEM program is to act as a bridge between scales to provide new, physically-based approaches of integrating HE effects into higher length and time scale models.

CHAPTER 2

HYDROGEN DISTRIBUTIONS AT DEFECTS IN CRYSTALS

The phenomenon of H embrittlement is believed to be largely controlled by atomic scale mechanisms. One of the most prominent proposed mechanisms is the HELP mechanism [35]. A central claim of the HELP mechanism is that H atmospheres, which form around dislocations, screen the interactions between dislocations, leading to increased dislocation mobility and increased stacking fault width (SFW); this promotes slip planarity. There has been limited detailed atomistic study of this particular effect, notably by Song and Curtin [24]. They concluded that H atmospheres around perfect edge dislocations in body centered cubic (bcc) Fe had no discernible effect on the pile up spacing of dislocations. While indicating that the proposed screening mechanism may be incorrect (at least for perfect dislocations), this leaves open the question of the effect of H atmospheres on partial dislocations.

In addition to affecting dislocations, H can segregate into grain boundaries, potentially altering their response to mechanical loading. Specifically, it has been proposed that H can act to lower the cohesive strength of a grain boundary, promoting decohesion [36, 25, 37]. Under shear loading grain boundaries may migrate [38], moving perpendicular to the boundary plane. Atomistic calculations have been used in survey type studies of grain boundaries (GBs) [39, 40, 41, 42, 43] with the aim of determining trends in properties of GBs as a function of misorientation. Particular attention is placed on trends in the GB energy and mobility. Additionally, hydrogen effects on GBs have been studied in atomistic simulations [44], with a focus on measured bulk mechanical response (stress-strain curves) as well as the intergranular fracture at boundaries but with H added in an ad-hoc manner.

To address the various effects H may have on dislocations and grain boundaries with atomistic calculations, we must first be able to construct physically realistic H distributions

around these defects. This chapter begins with a discussion of methods for calculation of discrete distributions of H. The proposed energy-based method is then compared with an existing stress-based method. H distributions calculated by the energy-based method are then used to generate structures for atomistic calculations of the H effect on the structure of extended edge dislocations at various background concentrations.

2.1 H distributions around dislocations

In order to compute the distribution of H around a dislocation core, we consider two different approaches; stress-based methods and energy-based methods. Stress-based methods consider the lattice to be a continuous medium, with insertion of defect atoms being modeled as Eshelby inclusions [45]; the distribution profile is determined by the work required to perform such an insertion. Recently, such Eshelby methods have been used to predict distributions of H in the vicinity of dislocations [27, 37]. Further, an alternative stress-based approach has been proposed [28] based on the Larche-Cahn open system theory [46, 47], which we will call the LC method. It has been shown [28] that predictions of the LC method correspond closely to results of Monte Carlo (MC) simulations for distributions of substitutional defects around a dislocation core, while the Eshelby method overestimates the distribution profile.

Energy-based methods consider the segregation energy, i.e., the difference in binding energy between a bulk site and a particular site of interest, to determine the distribution profile. These methods have not been considered as extensively in microscale modeling. This is likely due to their higher computational cost associated with calculation of the full set of site binding energies and site locations over a given structure of interest. However, energy-based methods can be readily used in systems for which the stress field due to the defect decays within roughly a few lattice parameters. Grain boundaries in a bicrystal are examples of such systems and have recently been studied in this way [48]. Energy based methods offer the advantage of calculating the binding to a specific site on the lattice, where

stress based methods require some approximation as they use a continuous stress field to calculated the occupancy. This, however, comes with a higher computational cost. Despite their higher computational cost, application of energy-based methods in the context of atomistic study has a strong advantage in applications to detailed atomic systems where single site resolution is important, such as near a dislocation core. Moreover, it is challenging to represent the stress field at dislocation cores, as required by stress-based methods, giving rise to uncertainty.

Typically the distribution of interstitial solute atoms among available sites is described by the site occupation, $\chi = n_i/n_s$, where n_i is the number of interstitial atoms, and n_s is the total number of sites. In the case of the Eshelby model, one can obtain the site occupancy from the conditions of mechanical equilibrium as

$$\chi_{Esh}(x,y) = \left\{1 + \frac{1-\chi_0}{\chi_0} \exp\left[-\frac{1}{k_B T}\left(\sigma_{ii}(x,y)\Delta V\right)\right]\right\}^{-1} \tag{2.1}$$

where $\sigma_{ii}(x,y)$ is the hydrostatic stress, ΔV is the misfit volume of the solute, χ_0 is the bulk site occupancy, k_B is Boltzmann's constant, and T is the temperature. From isotropic linear elasticity, the hydrostatic stress field around an edge dislocation can be written as [49]

$$\sigma_{ii}(x,y) = \frac{Gb(1+\nu)}{3\pi(1-\nu)}\left(\frac{y}{x^2+y^2}\right) \tag{2.2}$$

where G is the shear modulus, ν is Poisson's ratio, and b is the Burgers vector.

Although Equation 2.1 has been perhaps the most commonly used site occupancy expression in the literature, its use presents some difficulty. In the Eshelby model the misfit volume, ΔV, for an interstitial inclusion is taken to be the stress free atomic volume of that inclusion outside the host lattice. For H this is not a well-defined quantity. Instead, ΔV is often calculated from the partial molar volume of H [50, 27], $\Delta v/\Omega$, where Ω is the average volume of an atom comprising the host lattice and we can take Δv to be an alternative to

the misfit volume, ΔV, defined in the Eshelby model [51]. This may be measured experimentally [52, 53]. Similar to its experimental determination, it can be calculated using atomistic simulations under the small strain approximation by,

$$\epsilon_{ii} = n_H \frac{\Delta v}{\Omega} \tag{2.3}$$

where n_H is the number of H and ϵ_{ij} is the total strain tensor. Summation over repeated indices is implied. If the strain is only due to the insertion of solute atoms (zero external stress) and the deformation is isotropic then,

$$\epsilon_{ij} = \left(\frac{\partial \epsilon_{ij}^c}{\partial n_H} \right) n_H = \alpha \delta_{ij} n_H \tag{2.4}$$

where $\alpha = \frac{1}{a} \frac{\partial a}{\partial n_H}$ is the size factor, a is the lattice constant, and δ_{ij} is the Kronecker delta. Combining Equations 2.3 and 2.4 gives

$$\Delta v = 3\alpha\Omega \tag{2.5}$$

Conveniently, an analogous term to the Eshelby ΔV arises in the LC theory, V^*, which is equivalent to Δv, lending some validity to the approximation of ΔV using the partial molar volume [28]. If we take the approximation that $\Delta V = \Delta v$, then it can be determined directly by computation of α and Ω [54].

In the LC theory, a coupled chemo/mechanical equilibrium problem is solved, resulting in modification of the elastic constants by a concentration dependent term. The linear theory is used here, details of which will be omitted as they are discussed thoroughly elsewhere [54, 55]. For the purpose of this study, the LC theory results in modification of the ΔV term in Eqn. 2.1 and a change in the constant pre-factor of Eqn. 2.2 owing to the substitution of the open system Poisson's ratio. The resultant hydrostatic stress field is given

by

$$\sigma_{ii}^{*}(x,y) = \frac{Gb(1+\nu)}{3\pi(1-\nu+4G\lambda(1+\nu))}\left(\frac{y}{x^2+y^2}\right) \tag{2.6}$$

where

$$\lambda = \alpha^2\omega\left(\frac{\partial\mu}{\partial n_i}\right)_0^{-1} \tag{2.7}$$

is the modifying factor on the adiabatic compliance in the LC theory, μ is the chemical potential, and ω is the per atom volume of the stress free host matrix. Combining Eqns. 2.1, 2.6, and 2.7, and replacing ΔV with V^*, gives the LC site occupancy as

$$\chi_{LC} = \left\{1 + \frac{1-\chi_0}{\chi_0}\exp\left[-\frac{1}{k_BT}\left(\sigma_{ii}^{*}(x,y)V^*\right)\right]\right\}^{-1} \tag{2.8}$$

An expression similar to Eqn. 2.1, but in terms of the binding energy of interstitial sites, can be derived in the Grand Canonical ensemble, yielding

$$\chi_{BE}(\epsilon_i) = \left\{1 + \frac{1-\chi_0}{\chi_0}\exp\left[-\frac{\Delta\epsilon_i}{k_BT}\right]\right\}^{-1} \tag{2.9}$$

Notably, instead of a stress/volume work term driving the concentration profile, the profile is determined by the segregation energy, $\Delta\epsilon_i = \epsilon_i - \epsilon_0$, where ϵ_i is the binding energy at a particular interstitial site of interest, and ϵ_0 is the binding energy to a bulk interstitial site. Forms similar to this have been studied previously [56, 57]. Although χ_{BE} appears somewhat simpler than χ_{LC}, the calculation of the set of binding energies and locations of the corresponding interstitial sites can quickly become computationally intractable, due to the large number of energy minimizations which must be carried out. In this work, we will find the interstitial sites and their binding energies through energy minimization using relevant Embedded Atom Method (EAM) potentials [58]. While energy minimization can provide estimates of the binding energies, it is important to bear in mind that such energies

are approximate and depend on the chosen interatomic potential. To demonstrate this effect, results are compared using several available EAM potentials for Ni and Pd with interstitial H.

2.1.1 Calculating discrete H distributions from the energy-based site occupancy

The main effort in computing χ_{BE} is finding all of the stable interstitial binding sites and computing their energies. To do so, we systematically insert single H atoms into the initial structure, energy minimize that structure allowing the H atom to relax into a favorable interstitial site, and compute the total energy of the system, E_H. This is then compared to the total energy of the edge dislocation structure with no hydrogen atoms, E_0. To generate the full field of energies, a single H atom is rastered through the structure on a grid, and energy is minimized at each position. From the values of E_H and E_0, the binding energy of each interstitial site can then be calculated as

$$\epsilon_i = E_H - E_0 \tag{2.10}$$

It should be noted that this procedure neglects any H-H interactions, since the binding energies are all calculated for a single, independent H atom. The effect of the H-H interaction has been studied [59], finding that at sufficient interaction strength a hydride phase will form below an extended edge dislocation. These calculations are done by MS resulting in a zero temperature structure which may not be stable. To quantify the feasibility of this approximation we compare this method to the (self consistent) LC distributions. Following this procedure, the segregation energy is calculated and a discrete field of interstitial site occupancies is obtained. Each iteration of this calculation outputs both a binding energy and the location of its corresponding interstitial site. Unfortunately, this is the limiting step of the method and substantially reduces its tractability for large systems (larger than a few hundred thousand atoms). However, once the binding energy distribution is computed, generating discrete samples is trivial in terms of computation time.

To sample equation Equation 2.9, we generate a histogram of the energy (i.e., counts of the number of interstitial sites with a specific binding energy) to generate bins. Then, the quantity χ_{BE} is computed for each energy bin. Since the number of sites with a given binding energy is known (from the number of counts in our histogram) we can then calculate how many of those sites will be occupied by using $\chi_{BE}(\epsilon_i) = \frac{n_i}{n_s} \rightarrow n_s\chi_{BE}(\epsilon_i) = n_i$. Finally, the set of site locations in a single energy bin is randomly sampled n_i times and a H atom placed on each sampled site; for any given energy bin, all of the n_s locations are equally probable but only n_i will be occupied.

Systematically, the procedure is carried out as follows:

1. Generate a histogram from the field of interstitial binding energies, associating site positions with their corresponding energy. This step gives bins of the binding energy with counts of the number of degenerate sites.

2. Compute $\chi_{BE}(\epsilon_i)$ for each energy bin.

3. Compute $n_s\chi_{BE}(\epsilon_i) = n_i$ for each energy bin. We now know the number of H atoms, n_i, to be distributed in each energy bin.

4. For each bin, randomly sample n_i positions from a uniform distribution without replacement and assign a hydrogen atom to each position.

5. Compile and output the positions of all of the hydrogen atoms in a format appropriate for our application.

The appearance of the histogram of energies in this procedure is analogous to that of a density of states, i.e., a "density of interstitial states". If we consider the sampling in this way, the total number of particles in the system is given by

$$N = \sum_{i}^{N_{bins}} n_i = \sum_{i}^{N_{bins}} n_s\chi_{BE}(\epsilon) \tag{2.11}$$

where the summation is over all N_{bins} bins. Further, if we consider $n_s(\epsilon)$ and $\chi_{BE}(\epsilon)$ to be continuous functions of the binding energy,

$$N = \int_{-\infty}^{\infty} n_s(\epsilon)\chi_{BE}(\epsilon)d\epsilon \tag{2.12}$$

It is apparent in this interpretation that n_s is a density of interstitial states and χ_{BE} is a probability density function, specifically in this case a Fermi-Dirac distribution. With this in mind, we can calculate the variance in the site occupancy from the relation

$$\left\langle \chi_{BE}^2 \right\rangle = \frac{1}{k_B T}\left(\frac{\partial \chi_{BE}}{\partial \epsilon}\right) \tag{2.13}$$

giving the well known expression for the variance of a Fermi-Dirac distribution [60], i.e.,

$$\left\langle \chi_{BE}^2 \right\rangle \approx \chi_{BE}(\epsilon)\left(1 - \chi_{BE}(\epsilon)\right) \tag{2.14}$$

In the sampling procedure, the ensemble average site occupancy is calculated for each energy bin. By use of Eqn. 2.14, variance can be incorporated into the sampling, thus accounting for natural thermodynamic fluctuations of the system. Values needed for computing λ and V^* can be obtained by atomistic calculations. The α parameter is calculated by inserting H atoms into a perfect single crystal and calculating the corresponding volume change. The $\frac{\partial \mu}{\partial n_i}$ factor can be calculated analytically for interstitial hydrogen, assuming that the H atoms do not interact, since its chemical potential is well defined.

2.2 Comparing LC-based distributions with energy-based sampling

In the following section we make a comparison between the H distributions around an idealized perfect dislocation for the energy-based and the LC methods. The calculations in this section are carried out for an edge dislocation with a Burgers vector, b, in the $[100]$ direction ($b = a[100]$) for FCC Ni and FCC Pd with interstitial hydrogen. This particular idealized dislocation is chosen for simplicity; it does not disassociate as a $b = \frac{a}{2}[110]$

dislocation will, thus permitting the use of classical solutions for stress fields of perfect edge dislocations. This dislocation is the same used in [28] and thus facilitates direct comparison. For atomistic calculations, the simulation cell is periodic in the dislocation line direction, ξ, and in the direction of the Burgers vector. There are free surfaces in the $\xi \times b$ direction. The dislocation structure is shown in Figure 2.1. The Atomsk software package [61] is used to generate the initial structure, which is then energy minimized. The energetics of the Ni-H system are modeled using two EAM potentials [62, 48] and the Pd-H systems by another [63]. All atomistic calculations are performed using LAMMPS [64]. Images of atomistic structures are generated using Ovito [65].

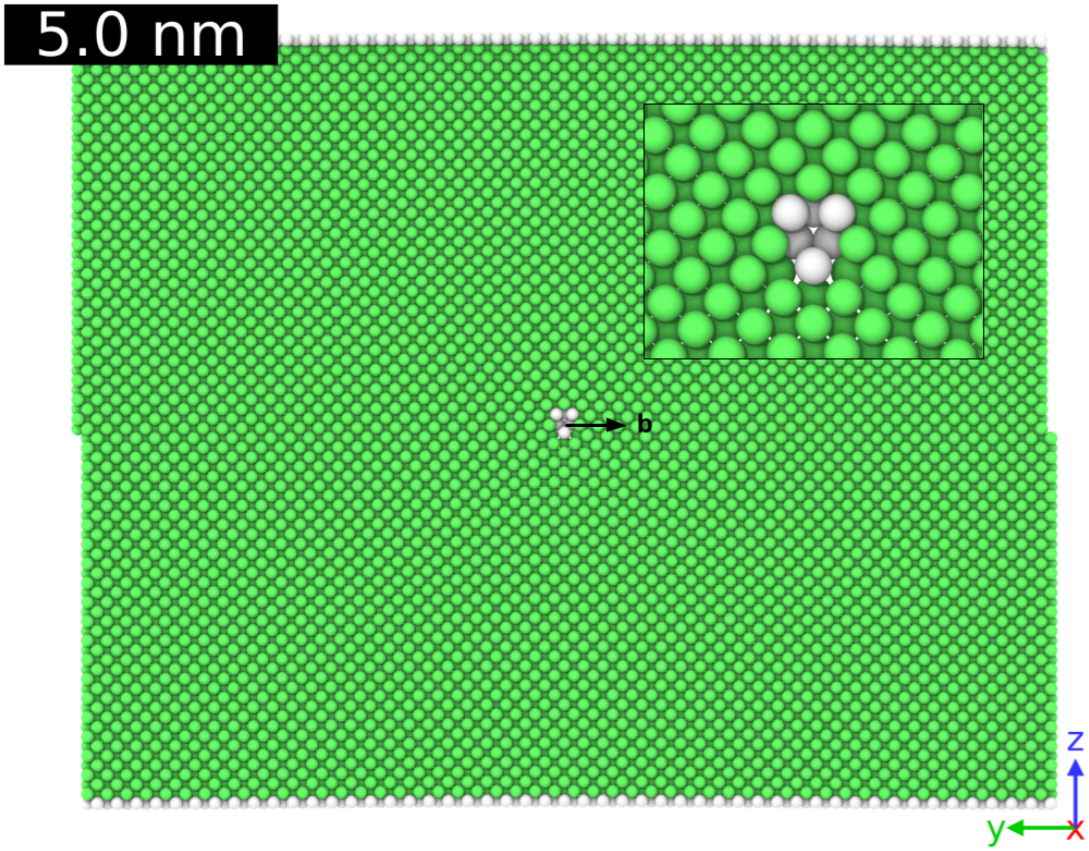

Figure 2.1: Edge dislocation structure with Burgers vector $b = a\,[100]$ colored by common neighbor analysis. The simulation cell is 178 Å in the y-direction and 128 Å in the z-direction and contains 29492 Ni atoms. The boundaries normal to the x and y-directions are periodic while the boundaries normal to the z-direction are free surfaces. The inset is a magnified view of the dislocation core.

Figure 2.2 compares the curve for χ_{LC} to computed values of χ_{BE} for two Ni-H potentials. The χ_{BE} values somewhat overestimate the site occupancy as compared to the LC curve, by a difference of about 1 per 100 occupied sites. As mentioned above, the choice of potential plays a significant role in the calculation of the binding energy of the H interstitials. The Angelo potential [62] has been widely used to study H interaction with defects. The newer Tehranchi potential [48] is a modification of the Angelo potential which aims to improve accuracy of binding energy values of H atoms to grain boundary sites. It may be expected that this might also improve accuracy of the binding energy values around dislocations. Indeed, the Tehranchi potential more closely matches the LC curve.

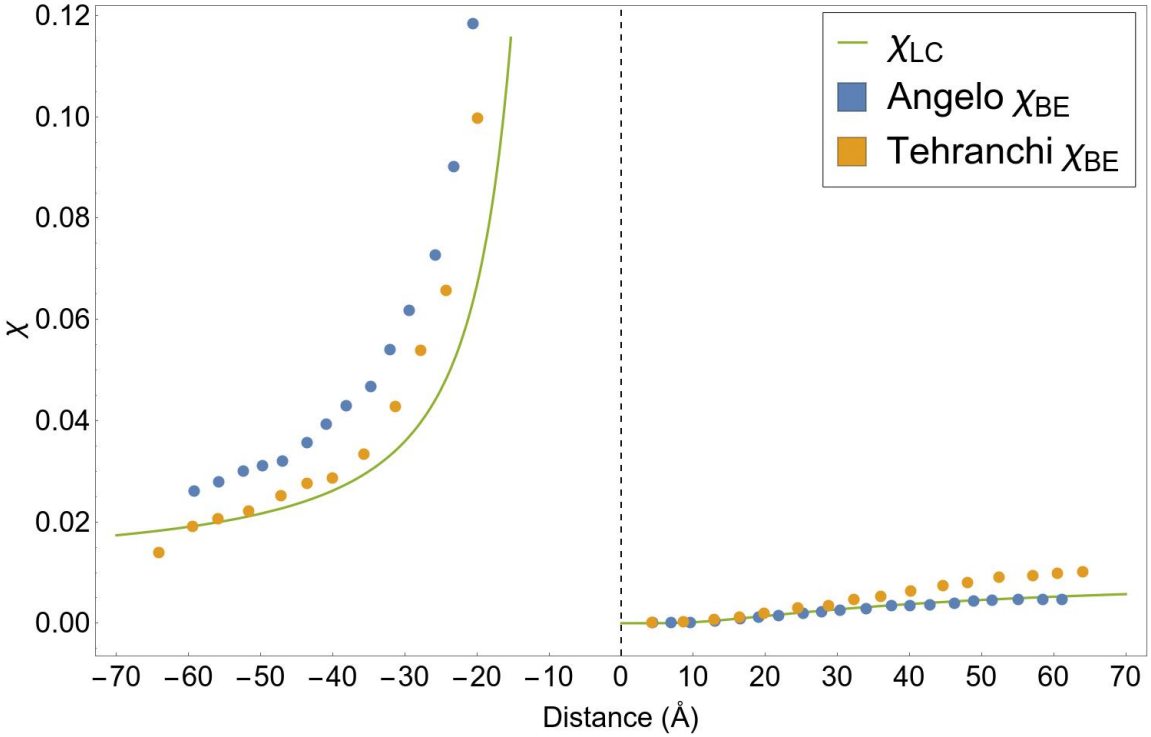

Figure 2.2: Site occupancy as a function of distance from the dislocation core in the direction mutually perpendicular to the Burgers vector and dislocation direction for the Ni-H system. Negative distances correspond to the tensile region below the core (where H is expected to concentrate) and positive distances to the compressive region above the core. The bulk site occupancy is $\chi_0 = 0.01$. The solid line is the LC site occupancy. The points are the computed values of χ_{BE} for both the Angelo (blue) and Tehranchi (yellow) potentials.

The comparison between the Tehranchi and Angelo potentials provides a somewhat biased result, as the Tehranchi potential is a modified version of the Angelo potential. To

provide an independent comparison, a Pd-H potential [63] is studied. The results for the Pd-H calculations are shown in Figure 2.3. The χ_{BE} values for this potential more closely match the LC result, again illustrating the strong dependence on the choice of potential. Ideally more potentials could be included, however few metal-H EAM potentials are available. It is also worth noting the deviation of the computed χ_{BE} values near the edge of the simulation box; this is likely due to the influence of free surfaces in that direction on the binding energy calculations. The stress field used in calculation of χ_{LC} is derived for a dislocation in an infinite medium, with no consideration of free boundaries.

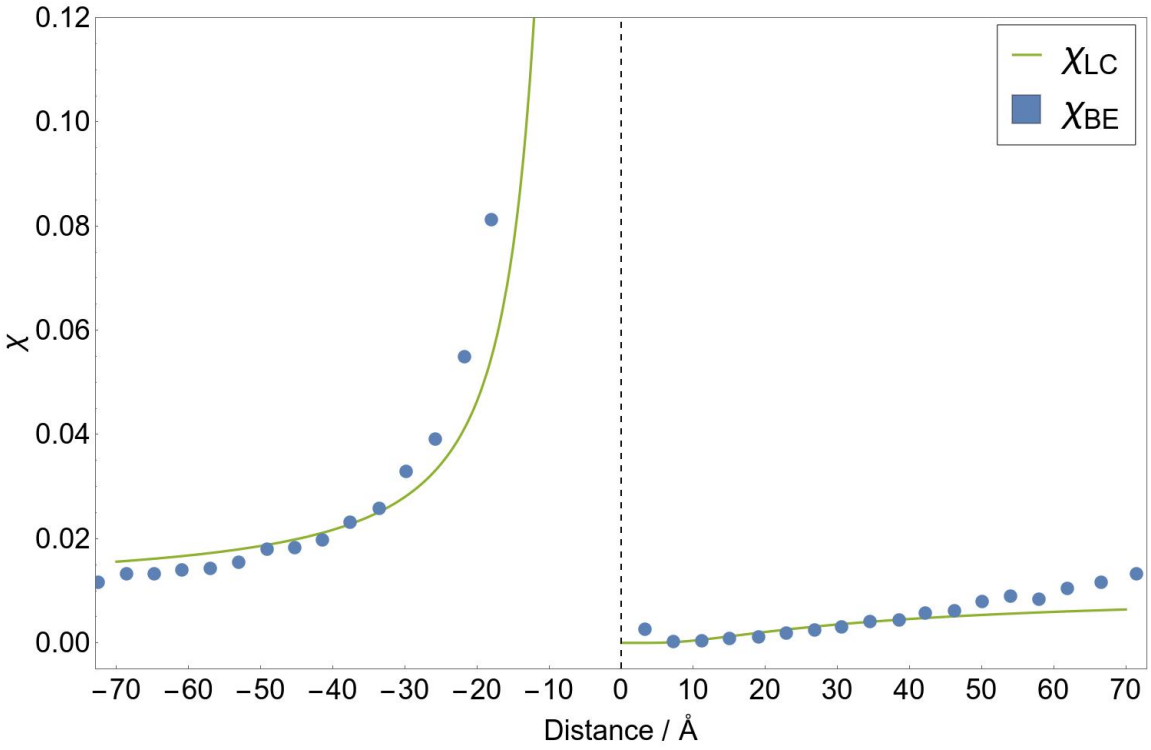

Figure 2.3: Site occupancy as a function of distance from the dislocation core in the direction mutually perpendicular to the Burgers vector and dislocation direction for the Pd-H system. Negative distances correspond to the tensile region below the core (where H is expected to concentrate) and positive distances to the compressive region above the core. The bulk site occupancy is $\chi_0 = 0.01$. The solid line is the LC site occupancy. The points are the computed values of χ_{BE} for the Pd potential [63].

In the analysis of the data to this point, we have implicitly assumed that the most accurate site occupancy is given by the LC curve. This is justified to some degree as the LC values have been shown to match MC data for substitutional solute atoms. However, this

has not been tested in the same way for interstitial solutes, let alone interstitial H. To the author's knowledge, the capability to conduct open system MC simulations for interstitial solutes is not currently available. This would require the calculation of the location of all interstitial sites at any step to avoid very high rejection rates. In other words, without a priori knowledge of the interstitial positions, during a MC step it is unlikely that a randomly inserted interstitial atom will place the system near an energy minimum position, and thus it is unlikely that any random insertion will lead to an accepted move.

Overall there is some correspondence between the two presented methods, as shown in Figures 2.2 and 2.3, although they do not produce identical results. This may be attributed to the choice of potential in the binding energy-based calculations; however, this is difficult to test as there are a limited number of potentials available for metal-H systems. With that in mind, each method has strengths and weaknesses in the context of discrete sampling of interstitial sites for use in atomistic simulations. Stress-based methods can provide fast and accurate calculations of the site occupancy, given a stress field. Because they are continuous, they are limited in their resolution when producing discrete samples. There is no information regarding the exact location of the interstitial positions and thus sampling may be inaccurate. In contrast, energy-based methods sample the interstitial sites directly, providing full resolution for generating discrete samples. Given a suitable potential, the energy-based methods can be used effectively to generate accurate discrete samples of non-homogeneous solute environments amenable for use in atomistic studies.

2.3 Stacking fault width of a partial edge dislocation in a hydrogen atmosphere

As an example problem which utilizes our energy-based sampling method, we study the screening of dislocation-dislocation interactions due to H atmospheres. One of the primary arguments of the HELP mechanism is that H atmospheres screen dislocation-dislocation interactions [66], thereby reducing pileup spacing of dislocations and, in the case of extended dislocations, widening stacking faults [7]. The effect of H atmospheres on pileup

spacing in bcc Fe has been previously studied using atomistic calculations [24], with the conclusion that H atmospheres have little effect. Here we address the effect of H on stacking fault width (SFW) in FCC Ni. The SFW is determined by a set of competing forces. The partial cores repel each other, while the force due to the stacking fault energy pulls the cores together. Here we investigate the effect of a H atmosphere on these interactions for a periodic array of dislocations. We note here that while this example draws parallels with dislocations pileups, this simulated system differs in that the spacing between dislocations is uniform whereas in a pileup, spacing between dislocations is nonuniform.

2.3.1 Stacking fault width of dislocations with H atmospheres

To test the effect of H atmospheres on dislocation-dislocation interactions, we introduce H atoms around an extended edge dislocation, shown in Figure 2.4. Structures used are $b = \frac{1}{2}[110]$ edge dislocations. The simulation cell is oriented with the dislocation line direction (x-axis) along the $[1\bar{1}2]$ direction, the Burgers vector is along the (y-axis) $[110]$ direction, and the orientation along the vector normal to the stacking fault (z-direction) is $[\bar{1}11]$. The simulation cell is quasi 2D and has dimensions $26 \times 250 \times 167$ Å. There is a free surface boundary normal to the z-direction and periodic boundaries normal to the x and y directions. The cell contains roughly 100,000 atoms. H atmospheres of background concentrations $\chi_0 = \{0, 0.0002, 0.0004, 0.0008, 0.001, 0.005, 0.01\}$ are introduced according to the method described in section 2.1.1. After H atmospheres are introduced, NVT dynamics are run at 300K using a Langevin thermostat until the SFW stabilizes. The relaxed system is then run, with measurements taken every 2 ps, and the output data processed to measure the SFW of the dislocations. The dislocation line positions are extracted using the dislocation extraction algorithm (DXA) [67] as implemented in Ovito [65] and run through its included Python interface. The time averaged SFW is then calculated. This is repeated 5 times for each background concentration. The calculated SFW values are averaged and their variance (due to the sampled structure) is computed. These data are shown in Figure

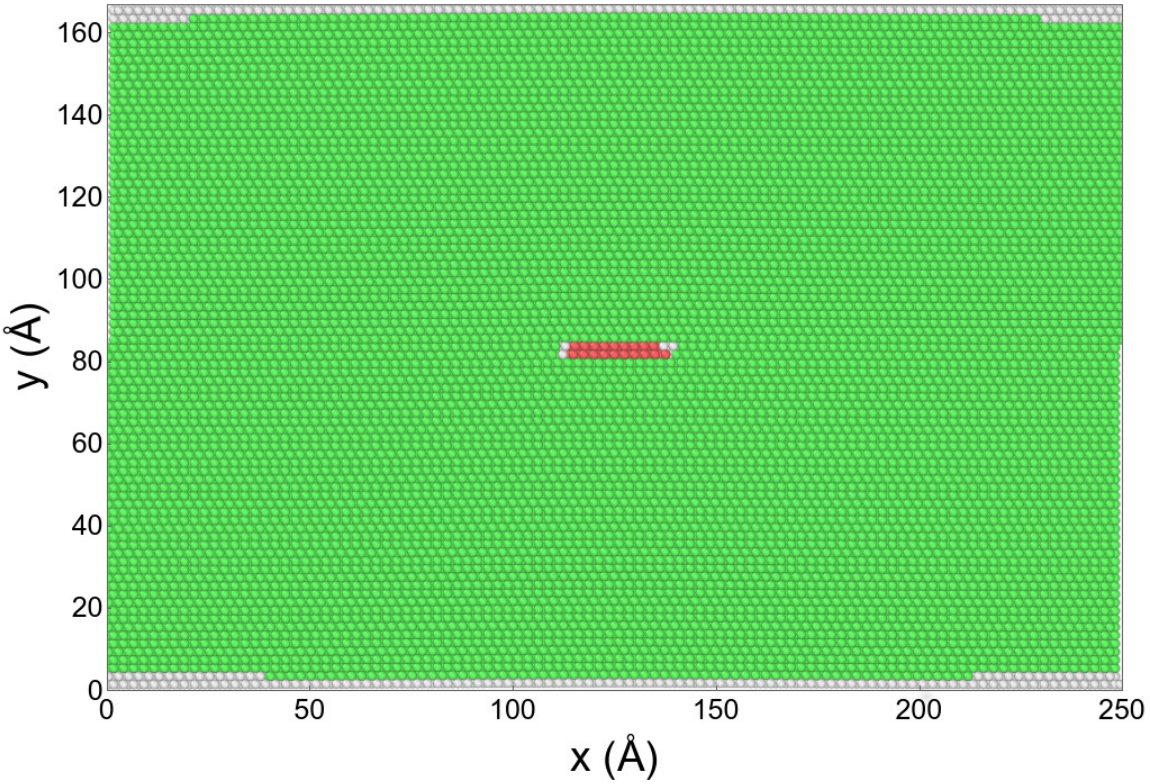

Figure 2.4: Edge dislocation structure with Burgers vector $b = \frac{1}{2}[110]$ colored by common neighbor analysis. The simulation cell is $26 \times 250 \times 167$ Å and contains roughly 100000 atoms. The boundaries normal to the x and y directions are periodic while the boundaries normal to the z-direction are free surfaces. The dislocation is created such that the extra half plane is in the upper region (above the dislocation).

2.5. We choose to focus on edge dislocations over screw dislocation as the effect of H on the screw dislocation is expected to be significantly smaller than that on an edge dislocation. This is because the hydrostatic stress field of a screw dislocations is very small compared to an edge dislocation and thus the amount of H segregating to screw dislocations is expected to be much lower than that around edge dislocations.

To isolate the effect of trapped H in the dislocation core from the surrounding atmosphere effect, two additional calculations are run on the structure with $\chi_0 = 0.005$. Here we define the "core" region as the region containing the partial dislocation cores and stacking fault. In terms of the interstitial spaces, the core comprises all the interstitial sites contained within the partial dislocation cores and stacking fault (the red and connected white atoms in Figure 2.4). The "atmosphere" refers to the entire region outside of the core region. In one

simulation, the H atoms are removed from the core region of the dislocation but H atoms are left in the atmosphere; in the other, H atoms are removed from the atmosphere but are left in the core.

Additionally, the effect of H on the generalized stacking fault energy (GSFE) is considered as a means of explaining the results. The GSFE can be calculated via molecular statics. In this case, a single crystal structure is prepared with the x, y, and z axes oriented along the $[112]$, $[\bar{1}10]$, and $[\bar{1}\bar{1}1]$ directions, respectively. The structure is divided in two along a $[111]$ plane and the the upper section displaced along the $[112]$ direction, minimizing energy at each step, keeping the x and y positions of all atoms fixed. H atoms are added to the plane between the upper and lower region in random positions and allowed to relax. This is performed for a set of concentrations $\chi = \{0.01, 0.02, 0.03, 0.04, 0.05\}$ with 10 realizations for each concentration. The average GSFEs for each concentration are displayed in Figure 2.6. This calculation is an elaboration on that done previously [68]. We include our calculation here to provide additional curves for systems with H atoms fixed in position throughout the process. Results will be discussed in the next section.

2.3.2 Results and discussion

Contrary to what has been observed experimentally [5], in our simulations the SFW decreases with increasing H concentration. This effect has been observed in previous studies [50, 69], indicating that the local interaction of H with the dislocation is dominant. As background H concentration increases, the measured SFW decreases (Figure 2.5). Further, the core effect dominates this phenomenon. The system with only H atoms in the stacking fault and core region yields a SFW about 4Å lower than that of the system with only H atoms in the atmosphere around the dislocation. To model our observations we start by reviewing the classical description of the extended dislocations. Without H, the total energy

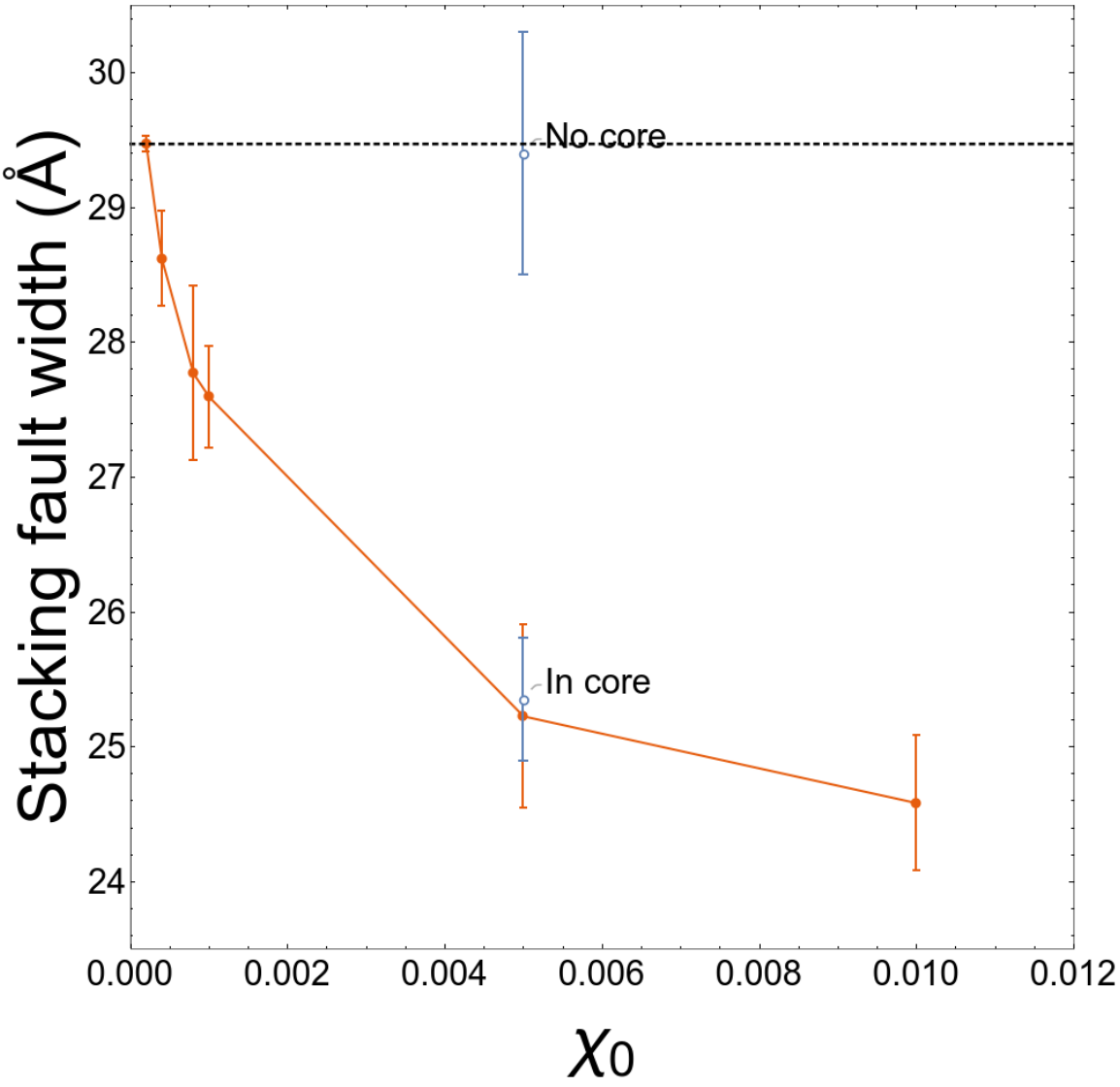

Figure 2.5: Average stacking fault width vs. background H concentration, χ_0. Error bars are the variance due to the sampled configurations from which the averages are measured. Also plotted (in blue) is the breakdown of the contribution due to H located in the atmosphere vs. the core of the dislocation for the structure with $\chi_0 = 0.005$. The point labeled "No core" is a system with no H in the core but with H in the surrounding atmosphere, the point labeled "In core" has only H in the dislocation core and none in the atmosphere. The dashed line is the SFW with no H.

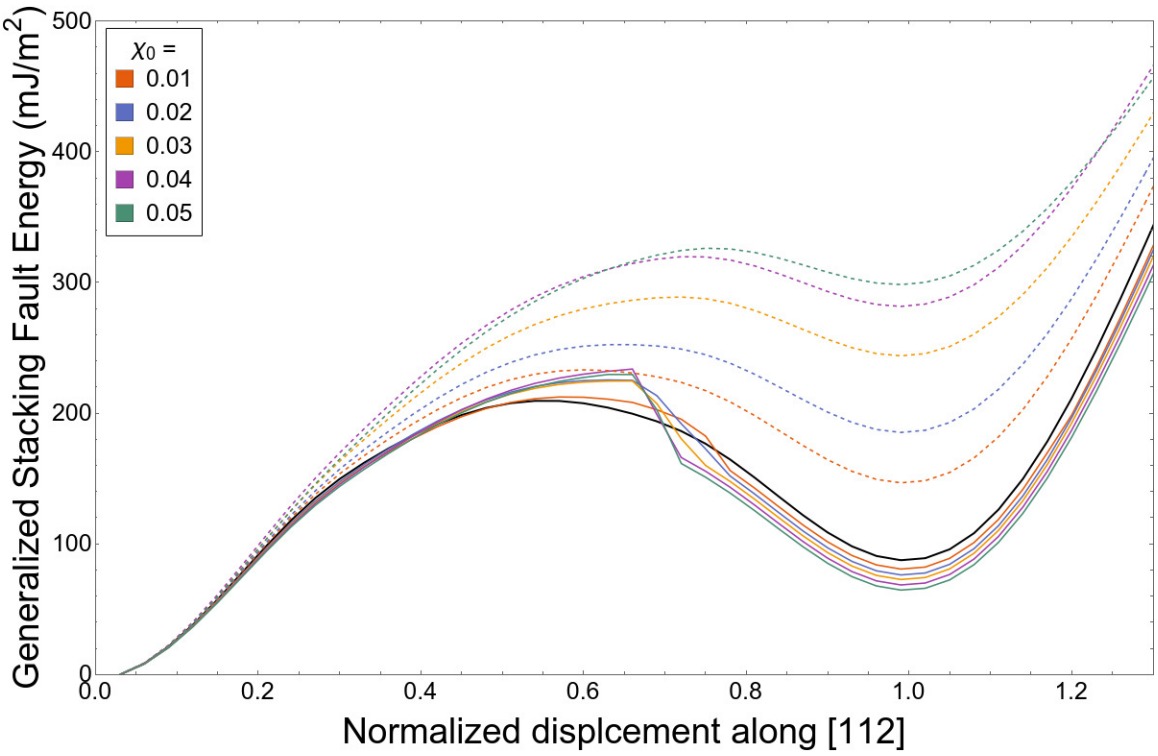

Figure 2.6: Generalized stacking fault energy for various H concentrations in the stacking fault plane. Dotted lines indicate that the H atoms are fixed in their positions during displacement while solid lines indicate that the H atoms are allowed to relax during the deformation (free H). The solid black line is the GSFE curve with no H. The discontinuities in the free H curves are due to the rearrangement of H atoms in a single step, leading to a large jump in the GSFE curve.

of an extended dislocation can be written

$$E_{tot} = E_{el} + E_{\gamma} \tag{2.15}$$

where E_{el} is the energy contribution due to the elastic field of the dislocation (repulsion of the partial cores) and E_{γ} is the energy due to the stacking fault between partial cores. In the case of an infinite lattice with a single dislocation E_{el} only accounts for the repulsion of the two partial cores but for a periodic array of dislocations we assume that the interaction with neighboring dislocations is accounted for in this term as well. The equilibrium SFW, d_0, is then determined by calculating the minimum of this energy, i.e.,

$$\frac{\partial E_{tot}}{\partial d} = \left\{ \frac{\partial E_{el}}{\partial d} + \frac{\partial E_{\gamma}}{\partial d} \right\} \Bigg|_{d=d_0} = 0 \tag{2.16}$$

and using classical dislocation models [49] we obtain the expression

$$d_0 \propto \frac{Gb}{\gamma_{SF}} \tag{2.17}$$

One approach to explaining the H effect on dislocation core structure is to consider the competing effects of the H affected stable stacking fault energy, γ_{SF}, and shear modulus. It is shown by Wen [70] that with increasing H concentration, G decreases linearly, which is consistent with decreasing SFW. The effect on stacking fault energy is not as clear. It has been suggested that for a Ni-H system, γ_{SF} may increase or decrease depending on the positions of the H atoms [68]. If the H atoms are only relaxed initially, prior to any SFE calculation involving subsequent changes of configuration, the SFE increases with increasing H concentration (shown in Figure 2.6). The increase in γ_{SF} for fixed H implies a decrease in SFW with increasing H concentration, consistent with our simulations. However, it is unclear that fixing the positions of H atoms in calculating the stacking fault energy is physically reasonable. If we consider the stacking fault energy calculated with H free to move, for a background H concentration (χ_0) of 0.01, γ_{SF} decreases from 87 mJ/m^2 to 80

mJ/m^2. This then implies that the SFW will increase by roughly 8%, inconsistent with our observation. Additionally, H may locally screen the elastic interaction of the neighboring partial cores, thereby reducing the repulsive interaction. In the following, we assume that the local screening effect of H on the interaction of the partial cores dominates over any long range screening and its effect on the stacking fault energy. We propose a method that models such local screening by explicitly accounting for the interaction energy of H with the partial cores.

H-affected SFW

We start by noting that H has a tendency to segregate in the tensile region under the dislocation core and in the stacking fault. This has the effect of screening the interaction of the partial cores, resulting in the decrease in the dislocation SFW. The decrease in SFW is illustrated in Figure 2.7. This effect is captured by decomposing the elastic energy into two terms, one which describes the elastic energy of the dislocation with no H, E^0_{el}, and another which describes the effect of the interaction of H with the dislocation field, E_H. The additional term, E_H is consistent with interaction energies described in previous studies [69]. We can then write the total energy, including H effects, i.e.,

$$E^H_{tot} = E^0_{el} + E_H + E_\gamma \tag{2.18}$$

We can then find the H affected SFW, d_H, by calculating the minimum of our new E^H_{tot}, i.e.,

$$\frac{\partial E^H_{tot}}{\partial d} = \left\{ \frac{\partial E^0_{el}}{\partial d} + \frac{\partial E_H}{\partial d} + \frac{\partial E_\gamma}{\partial d} \right\}\Bigg|_{d=d_H} = 0 \tag{2.19}$$

If we seek to understand the observation that H decreases the SFW of an edge dislocation, we place requirements on E_H that must be satisfied.

In the classical model of extended dislocations [49] the contribution due to the elastic

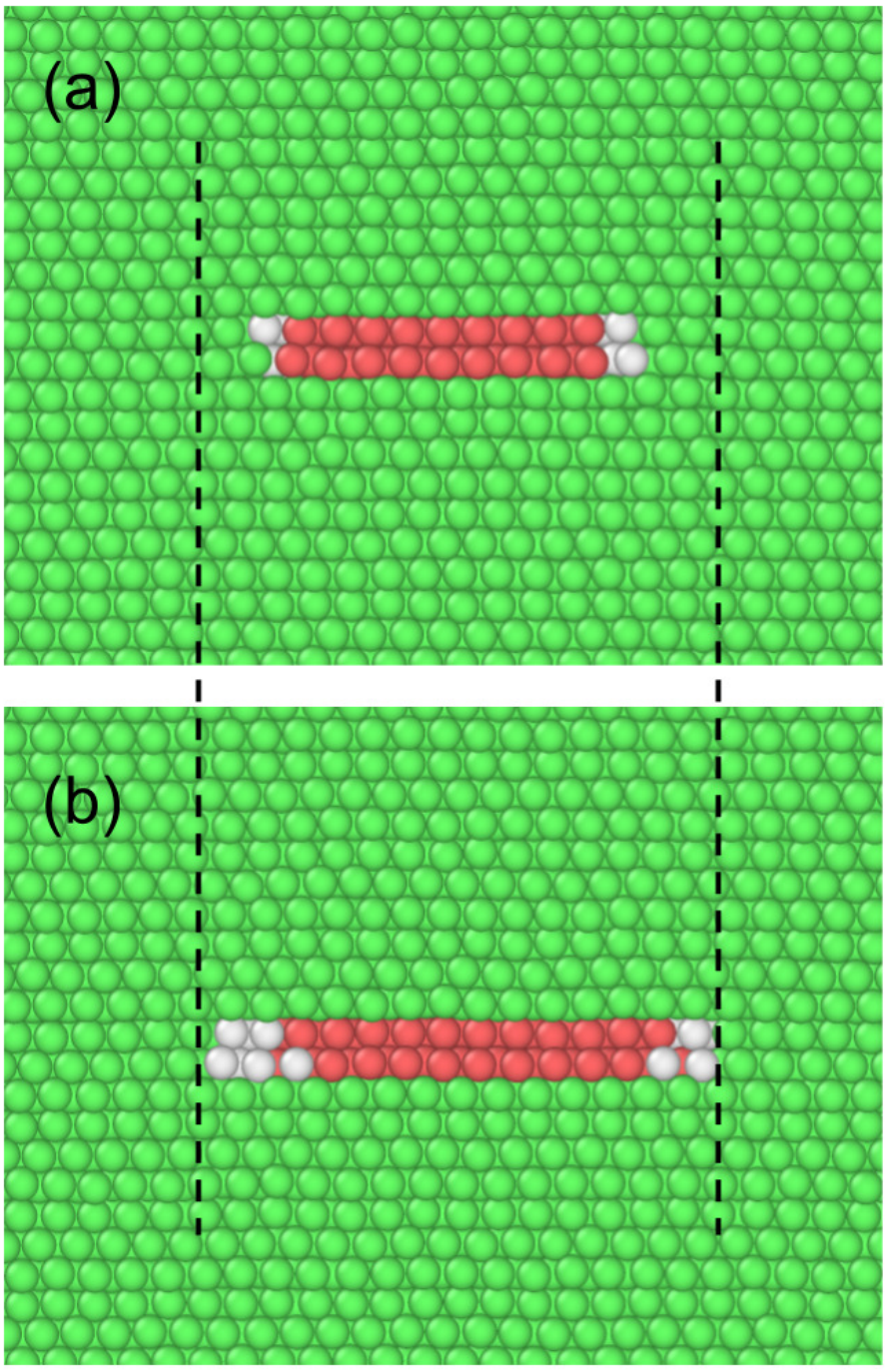

Figure 2.7: Resultant edge dislocation core structures for two different background H concentrations. In (a) $\chi_0 = 0.01$ and in (b) $\chi_0 = 0.0002$. It is clearly visible that in the higher H case, the SFW is decreased relative to the low H case.

field is

$$\frac{\partial E_{el}^{0}}{\partial d} \propto -\frac{Gb}{d} \tag{2.20}$$

and $\frac{\partial E_{\gamma}}{\partial d} \propto \gamma_{SF}$ so that if we consider the minimum of the total energy including H, as in Eqn. 2.19, we have

$$\frac{\partial E_H}{\partial d} + \gamma_{SF} - \frac{Gb}{d_H} = 0 \tag{2.21}$$

or

$$d_H \propto \frac{Gb}{\frac{\partial E_H}{\partial d} + \gamma_{SF}} \tag{2.22}$$

If we require that $d_H < d_0$ then any model for the interaction of H with the dislocation must satisfy the condition $\frac{\partial E_H}{\partial d} > 0$. Further, we have observed that increasing background H concentration, χ_0, decreases the SFW monotonically.

Energy of the dislocation-H interaction

To test the condition required by Eqn. 2.22, we define the interaction energy of a single interstitial site as the interaction energy between a single point defect and a dislocation, weighted by the probability of a site being occupied, i.e.,

$$E_H^1 = \chi(\sigma_{jj}) U_{int}(\sigma_{jj}) \tag{2.23}$$

Since the stress field is not defined at each site we instead calculate the interaction energy of a small region, or an element in a mesh. For the i^{th} element, if we take χ_i and U_{int} to be constant over the element, then

$$E_H^i = N\chi_i(\sigma_{jj}) U_{int}^i(\sigma_{jj}) \tag{2.24}$$

Here, N is the number of sites per element, which is $N = \rho_s V_{ele}$; ρ_s is the site density and V_{ele} is the volume of an individual mesh element. Element size is included here for clarity of the analysis, but in a calculation the element size should be taken so that $N > 1$. The total interaction energy, summed over all elements, is given by

$$E_H = \rho_s V_{ele} \sum_i \chi_i(\sigma_{jj}) U^i_{int}(\sigma_{jj}) \tag{2.25}$$

or

$$E_H = \int_V \chi(\sigma) U_{int}(\sigma) dV \tag{2.26}$$

where $\chi(\sigma_{ii}) = \chi_\sigma$ is the site occupancy field as a function of the hydrostatic stress field, σ_{ii} given in Equation 2.1 and the summation is over all elements. ΔV is the excess volume due to the insertion of H, however this is typically referenced to the stress free atomic volume of the solute atom, which is poorly defined for H. To address this, we use the LC effective volume of insertion in place of the Eshelby definition of ΔV. In order to calculate this value we require two components: the site volume, ω, and the compositional derivative of the strain, α. The site volume is calculated by computing the Voronoi volume of the octahedral interstitial sites. In order to calculate α, NPT dynamics are run at 300K and the simulation cell edge lengths measured for a range of H concentrations. The strain as a function of concentration is then calculated from the time-averaged edge lengths. Finally, the interaction energy is defined using a non-singular, gradient based stress field [71, 72], so that for a pure dilatation,

$$U_{int} = -Q\sigma_{ii} \tag{2.27}$$

Here, Q is the dilational strain due to defect insertion and the hydrostatic stress field is

given by Eqn. 2.28.

$$\sigma_{ii}(x,y) = \frac{Gb(1+\nu)}{\pi(1-\nu)}\frac{y}{r^2}\left\{1 - \frac{r}{l}K_1\left[\frac{r}{l}\right]\right\} \tag{2.28}$$

where $r = (x^2 + y^2)^{1/2}$, K_1 is the Bessel function of the second kind, and l is a length scale associated with the size of the dislocation core, which we take here to be $0.4a_0$. This is a modification of the classical stress field given by Equation 2.2 which is derived from a gradient theory and properly accounts for the nonsingular stress at the dislocation core [72]. To represent an extended dislocation (and to introduce the stacking fault width, d) we superimpose the contributions of the two cores, separated by the stacking fault, i.e.,

$$\sigma_{ii}^{part}(x,y,d) = \frac{1}{2}\left\{\sigma_{ii}(x - \frac{d}{2}, y) + \sigma_{ii}(x + \frac{d}{2}, y)\right\} \tag{2.29}$$

It is noteworthy that although the stacking fault is explicitly taken into account in the simulated binding energies, in the stress-based approaches (using a stress field as above) the stacking fault is not accounted for. Instead we assume that the effect is driven primarily by the hydrostatic component of the stress fields of the partial dislocation cores. We can then calculate the contribution of the H field by numerically integrating E_H. Figure 2.8 shows example plots of E_H and $\frac{\partial E_H}{\partial d}$ for values of d from 20 to 30 Å.

E_H is a monotonically increasing function of d, and thus $\frac{\partial E_H}{\partial d}$ is positive for all d, verifying our first condition. This supports the observation that H acts to decrease the SFW of a dislocation relative to its H free configuration, but does not confirm the trend that increasing χ_0 leads to decreasing SFW. This trend can be tested by calculating $\frac{\partial E_H}{\partial d}$ for a range of values of χ_0. Figures 2.8 and 2.9 are plots of $\frac{\partial E_H}{\partial d}$ for several values of χ_0 and the resultant SFW as a function of χ_0, respectively. The increasing trend of $\frac{\partial E_H}{\partial d}$ with increasing χ_0 indicates that the SFW should decrease, in agreement with our simulation.

In Figure 2.9, SFW determined from the outlined model is compared with the SFW data from MD simulations. It is shown that trends observed in the simulation data can

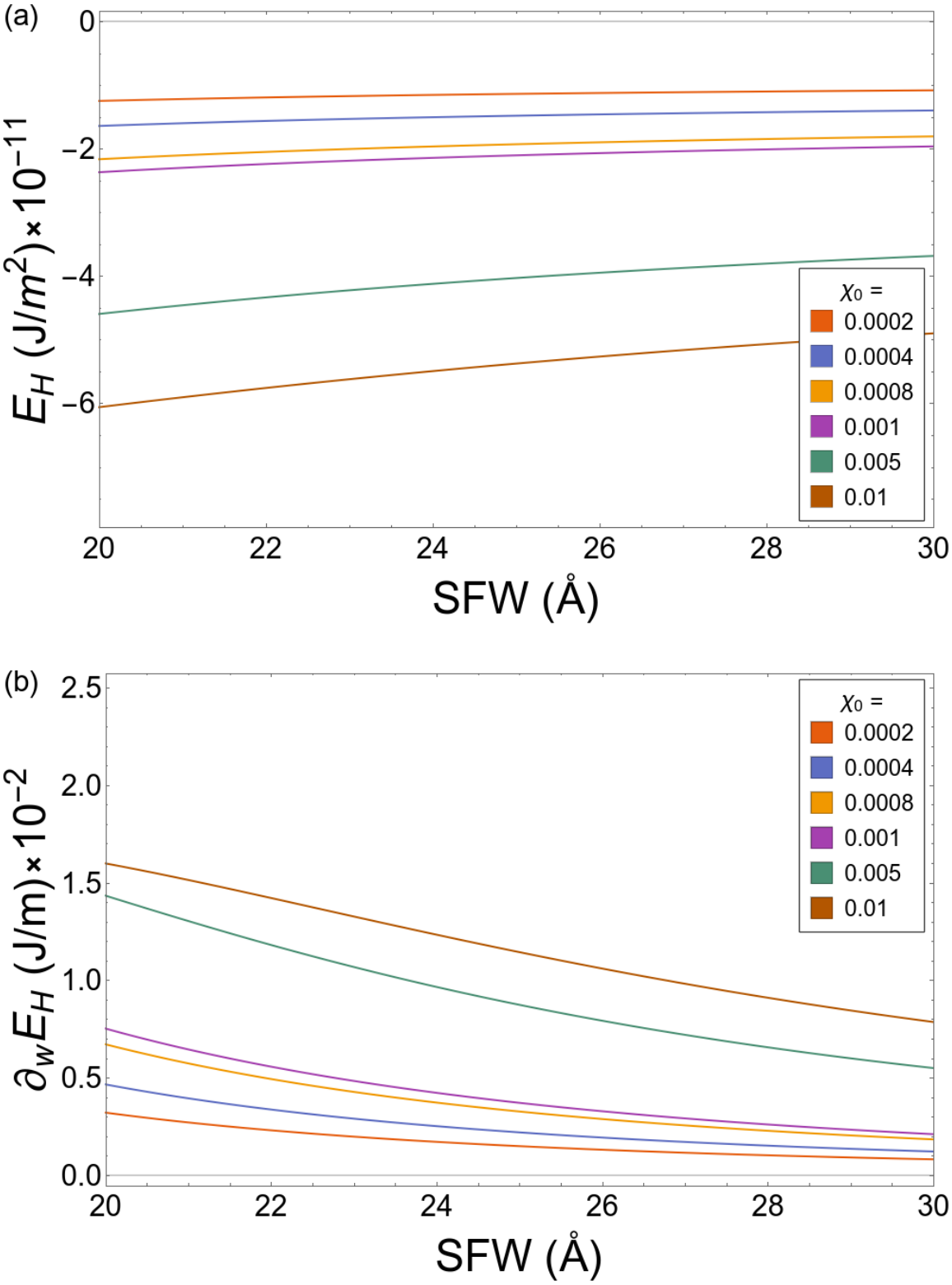

Figure 2.8: E_H (a) and $\frac{\partial E_H}{\partial d}$ (b) as a function of SFW for differnt values of the background H concentration $\chi_0 = \{0.01, 0.005, 0.001, 0.0005, 0.0001\}$

be reproduced by explicitly accounting for the interaction of H with the dislocation. It should be noted that in calculation of d_H the classical descriptions of E^0_{el} and E_γ may be incompatible with the the description of E_H. These terms are temperature independent and are derived from different distance scales than our description of E_H; as such, we allow flexibility in choosing the values of Q and ΔV. The model curve shown in Figure 2.9 is for $Q = 0.006$ and $\Delta V = 3.6 \times 10^{-30} m^3$. For reference, the value of Δv calculated for this system is $1.8 \times 10^{-30} m^3$.

2.3.3 Summary

We have utilized physically realistic equilibrium distributions of H around a periodic array of partial edge dislocations to study the effect of H on the interaction of neighboring dislocations. An algorithm for sampling such distributions was presented and subsequently used to generate structures for atomistic calculations. The SFW of the extended dislocation was computed, after the dislocation is allowed to dynamically relax, to study any potential effect that the H field may have on the dislocation core structure. The results of MD calculations indicate that the effect is primarily due to local screening of the repulsive interaction of the partial cores, rather than a long range interaction effect.

A decrease in SFW is observed with increasing H concentration. While consistent with some recent results [50, 69], this is inconsistent with conventional modeling approaches, which ascribe the effect of H to a change in the stable stacking fault energy or shear modulus and predict that increasing H concentration leads to increasing SFW for H. To interpret our atomistic simulations, we introduce an interaction energy term into the energy balance which accounts for the observed local screening by explicitly adding the interaction energy of H with the extended dislocation. Significantly, we observe that the local interaction of H with the extended edge dislocation drives a relaxation process leading to a net decrease of the SFW.

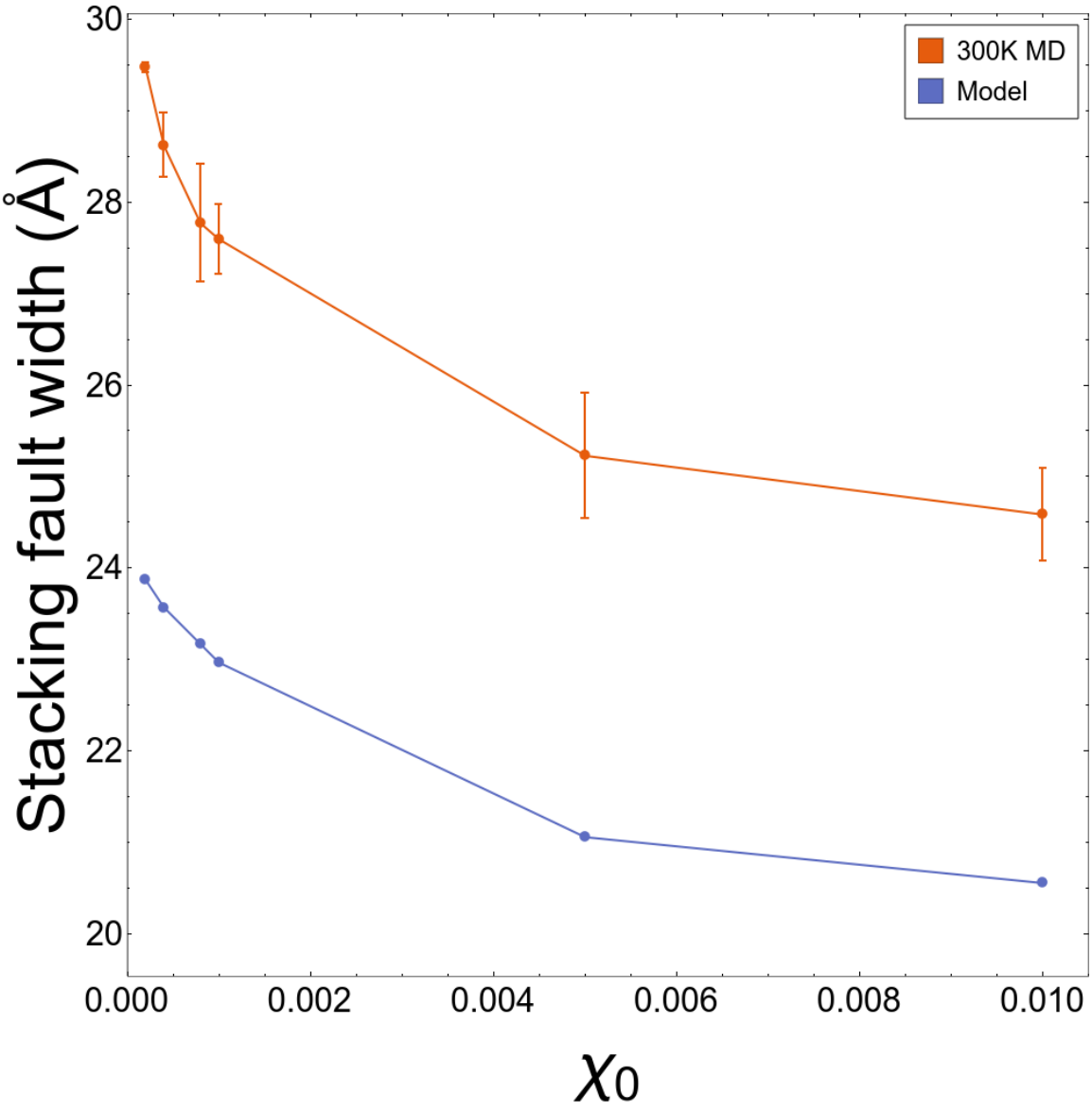

Figure 2.9: SFW as a function of the background H concentration, χ_0, for MD simulations as well as calculated values from described model (Equation 2.22).

2.4 Conclusion

In this section we have described a method for calculation of the H distribution in the elastic field of a dislocation. In our method, the H binding energy is used to determine the occupation probability of the collection of possible interstitial H sites, from which a discrete H distribution can be sampled. This method provides the advantage (in comparison to stress-based methods) of computing the exact interstitial positions, providing a more precise distribution in and directly around the dislocation cores. This model is exercised to study the effect of H on the core structure of an extended edge dislocation in Ni-H. Its is found that the SFW decreases with increasing H concentration and that this effect is primarily due to the interaction of the partial cores with the local H atoms near the cores. Little far field effect is observed. This indicates, consistent with other simulations [24], that H does strongly influence long range dislocation-dislocation interactions. This places stronger emphasis on HE mechanisms that consider H to act locally in conjunction with other defects (such as HESIV). Following this, for the remainder of this thesis, we focus on the role of H in the development of high vacancy concentrations due to plastic deformation.

CHAPTER 3

PRODUCTION OF EXCESS VACANCIES BY DISLOCATION INTERACTIONS

Recently there have been indications that H alone cannot account for the observed H-embrittlement phenomena and that the interactions of H with vacancies plays a significant role in the effect [73, 11]. Vacancy concentrations much greater than those expected at equilibrium are produced during plastic deformation [74]. Production of excess vacancy concentrations has been observed experimentally by X-ray line profile analysis [75], by electrical resistivity and differential scanning calorimetry [13]. When high levels of vacancies are present H can act to stabilize this excess by lowering the formation energies [18, 19, 20] promoting the formation of vacancy-H complexes. These observations are consistent with a proposed mechanism [16] which ascribes that the main action of H on embrittlement effects to its role in the formation of high concentrations of vacancies and vacancy clusters.

A model has been introduced which considers the production of vacancies during plastic deformation to be due to the interactions of dislocations in persistent slip bands (PSB) [29, 76] based on a previously developed bowing and passing model [77, 78, 79]. Within this context, vacancies are generated by the annihilation of dislocation loops [80] and the subsequent dragging of jogged segments [81]. In the following chapter we introduce this model as a starting point for development of an expanded model of vacancy production in PSBs. While this previous model is developed with PSBs in mind, the formulation remains valid for cellular substructures during cyclic slip as well. The goal here is to develop a physics based model inspired by this previous framework, for vacancy balance which is compatible with macroscopic crystal plasticity finite element (CP-FEM) simulations. The term describing vacancy production is defined explicitly, but currently the vacancy annihilation term is parameterized. Possible mechanisms of vacancy annihilation are discussed

along with some corresponding atomic scale simulations and analysis. This model is implemented in an existing CP-FEM framework and some preliminary results are shown and discussed.

3.1 Polák-Sauzay model

Polák and Sauzay [29] proposed a model for the steady state vacancy concentration in PSBs. A PSB generally consists of dislocation rich walls separated by sparse channels. While a PSB has a specific structure, this is analogous to cellular dislocation substructures that are formed by processes associated with interacting mobile dislocations under cyclic shear. When subject to an applied stress, sources embedded within the walls may emit dislocation loops which will bow out into the channels. These loops can then cross the channel, with the leading segment being annihilated into the wall. In this case two screw type segments are left behind, spanning the length of the channel. These segments glide in the channels until they are annihilated by other screw segments. In another case dislocation loops emitted from adjacent walls may meet in the channel resulting in annihilation of the leading edge type segments. The annihilated segments leave behind a row of point defects, of either vacancy or interstitial type depending on the relative signs of the dislocations. In addition, two jogged screw segments are left spanning the channel. As jogged segments glide they drag the jogs along with them, resulting in generation of additional point defects. These processes are illustrated in Figure 3.1. In their model, they take the vacancy production rate to be independent of the current vacancy concentration and the vacancy annihilation rate to be a linear function of the current vacancy concentration, i.e.,

$$\frac{\partial c_v}{\partial N} = p - A c_v \tag{3.1}$$

where p is the production rate parameter, A is the annihilation parameter, c_v is the vacancy concentration, and N is the cycle number. They then calculate the vacancy concentration,

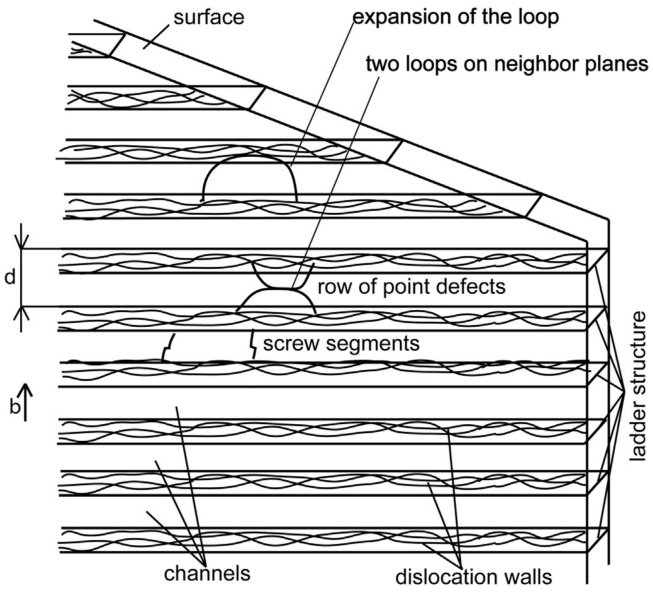

Figure 3.1: An illustration of a PSB from the work of Polák and Man [76]. The scenario of a loop bowing out and spanning a channel is illustrated as well as the possibility of two loops meeting in a channel forming a row of point defects.

i.e.,

$$c_v(N) = \frac{p}{A}\left(1 - \exp(-AN)\right) \tag{3.2}$$

While this approach is appealing in its simplicity, the production and annihilation parameters are unclear. In the following, we propose a model in the spirit of the work of Polák and Sauzay but that directly accounts for the statistics of dislocation bow out and annihilation processes.

3.2 Statistical model of vacancy production

To more clearly define the vacancy production term, we consider the statistics of bow out and annihilation processes. In the model we envision a substructure consisting of dislocation rich walls separated by channels, as in a PSB or a cellular substructure. The walls contain a collection of Frank-Read sources [82] which, when activated, can bow out dis-

location loops into the channels. A Frank-Read source is simply a dislocation segment pinned between two obstacles. As a force is applied to the pinned dislocation it will bow out from the pinning points until a critical stress is achieved, after which the dislocation loop breaks free of the source. The critical stress required to bow out a dislocation loop from a source takes the form [49]

$$\tau_{crit} \propto \frac{Gb}{L} \tag{3.3}$$

where G is the shear modulus, b is the Burgers vector, and L is the source length or the distance between pinning sites. While this equation provides a general result several modifications have been made over time [83] but are outside the scope of this analysis.

We start our analysis by calculating the density of activated sources in a wall following a recent approach [84] that considers a collection of sources with their activation strengths being normally distributed. If the probability density for the source strength, $\psi(\tau)$, is the normal distribution where τ is the resolved shear stress on a source then the cumulative distribution function is given by

$$\Psi(\tau) = \int_{-\infty}^{\tau} \psi(\tau) d\tau = \frac{1}{2}\left\{1 + erf\left[\frac{\tau - \bar{\tau}}{\sqrt{2}\sigma}\right]\right\} \tag{3.4}$$

Here $\bar{\tau}$ is the average critical activation stress of a normally distributed collection of Frank-Read sources and σ is the standard deviation in the distribution of activation stresses. The distribution of critical activation stresses can be thought of in the context of this model as a distribution of source lengths, L, related through equation 3.4. For single slip, the density of activated sources is

$$\rho_{act} \propto \rho^0 \Psi(\tau) \tag{3.5}$$

where ρ^0 is the total source density. The source activation rate is given by

$$\frac{\partial \rho^+}{\partial t} = \rho_{act} \frac{\bar{v}}{l_s} = \frac{\rho_{act}}{l_s \rho b} \dot{\gamma} \tag{3.6}$$

where ρ^+ is the density dislocations generated by activated sources, the average dislocation velocity, $\bar{v}$, is obtained from the Orowan relation [85], $\dot{\gamma} = \rho b \bar{v}$ (ρ here is the total dislocation density), where $\dot{\gamma}$ is the plastic shear rate, and l_s is the distance a loop must travel from a source before that source can emit another loop. Assuming the sources are spatially distributed according to a uniform random distribution, the probability of two loops annihilating in the channel is

$$p_{ann}(\tau) \propto C_n y_s^{edge} (\rho^+)^2 \tag{3.7}$$

where y_s^{edge} is the edge dislocation annihilation height and $C_n = 1/\rho_{mat}$ is a normalization factor related to the material density, ρ_{mat} (which for FCC is $4a_0^3$). The number of vacancies generated is then given by

$$\dot{c}_v^+ = \Phi_{ann} p_{ann}(\tau) \tag{3.8}$$

Here Φ_{ann} is the annihilation efficiency, or the number of point defects produced per dislocation annihilation event. The superscript '+', as in the case of the dislocation density due to source activation, denotes the additional quantities generated in this model formulation. In the above analysis, many of the values can be obtained by a finite element crystal plasticity (CP) calculation; however, some can not. With this formulation we have outlined a model for the generation of excess vacancies based on the physical mechanism of dislocation bow out from walls comprised of Frank-Read sources and their subsequent annihilation. This provides a formulation which, rather than being based on arbitrary parameters, relies on input of physical parameters. For some quantities this is straight forward and values for τ, ρ, $\dot{\gamma}$, and Δt can be obtained or are used in the CP calculation while Φ_{ann} , y_s^{edge}, and l_s

can be calculated directly. However, the values of the source parameters $\bar{\tau}$, σ, and ρ^0 are more difficult to obtain, as measurements do not exist. Further, discrete dislocation dynamics calculations which could potentially assess the source properties require prohibitively large dislocation densities. Due to these limitations, we consider choices for the source parameters as approximations and choose values consistent with other work [84].

For the vacancy concentration to reach a saturation point, as is observed in experiments [75, 13], vacancies must also be allowed to annihilate by some mechanism (or set of mechanisms). Thus, we must consider the balance of production and annihilation of vacancies, i.e.,

$$\dot{c}_v = \dot{c}_v^+ - \dot{c}_v^- \tag{3.9}$$

where c_v^+ is the concentration of vacancies being produced and c_v^- is the concentration of vacancies being annihilated. While this section focused on the calculation of c_v^+ in the following section we provide analysis of possible vacancy annihilation processes contributing to the required vacancy balance.

3.3 Vacancy annihilation

As a simple way of estimating the vacancy annihilation term we can take $c_v^- \propto Ac_v$, as was done in the work of Polák and Sauzay [29]. Approaching the problem in this way obscures the underlying mechanism by using a fitting parameter to characterize the vacancy annihilation process, but provides a simple estimate of the model form. With this in mind we can explore some possible mechanisms for vacancy annihilation with the goal of quantifying their impact on vacancy annihilation. For mobile vacancies an additional term will be incorporated into the vacancy annihilation, accounting for the diffusion of vacancies to sinks [29, 86]. As a starting point for investigating mechanisms we propose a simple form which accounts for the mechanisms of static Frenkel pair annihilation and diffusion of vacancies.

In this case,

$$\dot{c}_v^- = y_v c_i c_v + D_v \tau^{(\alpha)} \nabla^2 c_v \tag{3.10}$$

where y_v is the activation volume for Frenkel pair recombination, c_i is the self interstitial concentration, D_v is the vacancy diffusion coefficient, and $\tau^{(\alpha)}$ is the slip system level shear stress. The first term captures static recombination of vacancy-interstitial pairs [87]. Effectively it represents the probability of annihilation given two randomly distributed sets of points defects. Here we have vacancies, c_v, and self interstitial atoms, c_i, which will recombine if they are located within y_v of each other. The second term captures diffusion of vacancies to dislocation walls [29]. This term is directly proportional to the vacancy diffusivity.

Another possible mechanism is the sweeping of vacancies by mobile dislocations. This is feasible, provided that the vacancies are not stabilized in some way. However, it has been shown in MD simulations of α-Fe that H can stabilize vacancies and vacancy clusters with respect to sweeping by dislocations [48, 88]. When a single vacancy with no H is encountered by a dislocation the vacancy is absorbed by the dislocation, creating a jog. If, however, the vacancy contains a sufficient number of H atoms the dislocation will simply bypass the H-vacancy cluster. The same has been observed for di-vacancies [48]. Perhaps in situations with low H concentrations a significant number of vacancies are swept by dislocations, or perhaps the stabilization effect is less pronounced in FCC Ni; however, these results suggest that this mechanism is not dominant.

In addition to the other proposed mechanisms, pipe diffusion (diffusion of point defects along dislocation cores) provides another possibility. Pipe diffusion can be incorporated into theoretical formulations via an 'effective diffusivity' which can be written as a combination of the lattice diffusivity, D_v, and the diffusivity along a dislocation, D_{pipe}, weighted

by their fractional occupancy [89] i.e.,

$$D_{eff} = (1 - f_d)D_v + f_d D_{pipe} \tag{3.11}$$

where f_d is the dislocation volume fraction. There are two possibilities regarding pipe diffusion. The first is that vacancies may diffuse a relatively short distance to a dislocation line which is spanning the channel, and can then be 'piped' to the wall. Another possibility is that vacancies coalesce into nanovoids. Screw dislocation segments are then pinned by these voids, creating channels for diffusion of vacancies from the voids into the PSB walls.

In the following section we provide some analysis of the possible mechanisms, starting with atomistic simulations of Frenkel pair recombination. Next, we consider the role of vacancy diffusion by studying the lattice vacancy diffusivity, D_v. Following this, a discussion of the effect of pipe diffusion on vacancy diffusivity is presented. The applicability of each mechanism is evaluated based on the results in each section.

3.3.1 Frenkel pair recombination

Calculation of the contribution of static recombination to vacancy annihilation requires the activation volume, y_v, as input. This can be calculated from the Frenkel pair recombination radius, which has been calculated for bcc Fe by object kinetic Monte Carlo (OKMC), giving $r \approx 2.26a_0$ [90] where a_0 is the lattice parameter. Here we perform a similar calculation for a self interstitial atom as it diffuses to and recombines with a vacancy in FCC Ni. The EON code [91] is used to conduct adaptive kinetic Monte Carlo (AKMC) calculations of the hopping of a self interstitial atom in Ni using an appropriate EAM potential [58, 62]. We choose to use this method as opposed to direct MD simulation in order to accommodate the long timescale associated with diffusion. In conventional MD, the time step must be chosen to accommodate the highest frequency modes relevant to the system. In the case of atomic crystals this mode is the vibration of individual atoms, which is on the order of fs; integration time steps are typically chosen to be on the order of fs. With time steps this

small (2 fs), it quickly becomes computationally intractable to study processes driven by rare events, such as diffusion.

Kinetic Monte Carlo (KMC) methods get around this limitation by employing harmonic transition state theory to estimate the rates of rare events. The transition rates are calculated by using the standard Arrhenius form

$$R = \nu \exp^{(-\Delta E/k_B T)} \tag{3.12}$$

where ν is an attempt frequency, ΔE is the activation barrier of the process, k_B is Boltzmann's constant, and T is the temperature. In AKMC [92, 93] transition pathways are found by adaptive search. Starting from an initial state, a dimer search [94, 95, 96] is carried out to find an accessible transition pathway. A library of all pathways is generated for the particular state and the fastest transition rates are sampled. The system is then progressed to a new connected state. The time is updated by randomly sampling the distribution of escape times from the starting state.

This method is employed here to calculate the recombination radius of a self interstitial with a single vacancy. A small simulation cell is created with a single self interstitial and a single vacancy. It is ensured that the self interstitial atom is initially located a distance of at least $5a_0$ from the vacancy. The self interstitial atom relaxes into a $[100]$ split configuration, which is common for FCC metals. Following the initial relaxation, an adaptive search is run from the initial state to find possible escape pathways. The interstitial atom hops through the pathway illustrated in Figure 3.2. Starting from the $[100]$ split configuration, one of the split interstitial atoms shifts through the transition state resulting again in a $[100]$ split configuration along a different $[100]$ direction. The activation energy for this process is found to be 0.106 eV. Interstitial hopping proceeds in this manner until recombination occurs.

The value of the recombination distance is measured as the last recorded position of the self interstitial prior to annihilation with the vacancy. This point is determined by

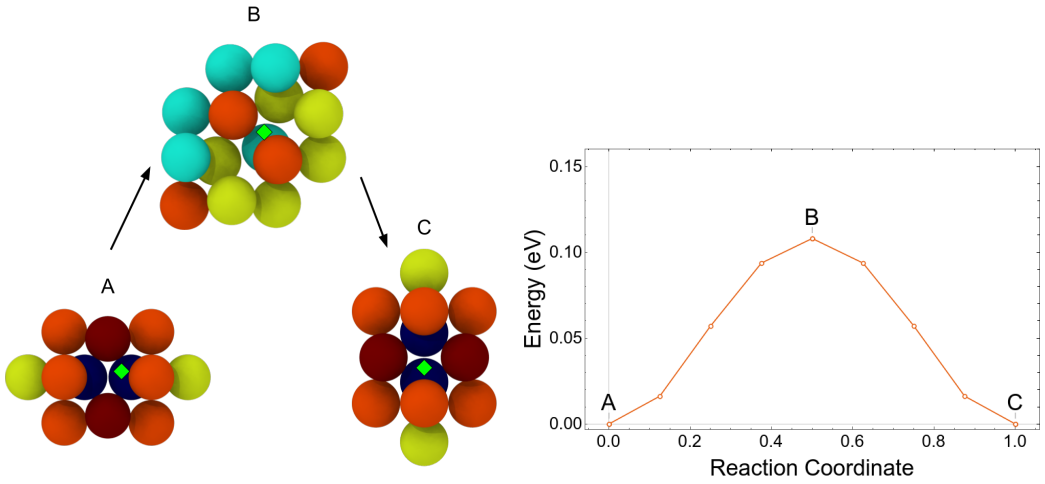

Figure 3.2: Nudged elastic band (NEB) calculation of the energy barrier for self diffusion in Ni. The left image shows configurations at the initial, saddle, and final states moving from a $[100]$ split interstitial (A) through the transition state (B) to another $[100]$ split interstitial along a different line direction (C). The green diamond labels the moving interstitial atom. Atoms are colored according to their potential energy. On the right is the corresponding plot of the energy of each state as a function of the reaction coordinate.

a discontinuity in the total system energy as a function of time (due to the defect pair recombination). This is run 10 times, allowing for annihilation from different positions. Each sampled transition pathway is added to a library (that is shared among runs), which is used to accelerate simulations. Measured distances are averaged giving a value of $r \approx 1.8a_0$. Taking $r = 2a_0$ and $c_v = c_i = 10^{-5}$ we arrive at $y_v c_i c_v \approx 1.5 \times 10^{-37}\text{m}^{-3}$. This value is much smaller than the production term and thus this mechanism likely does not contribute significantly to the vacancy balance.

3.3.2 Vacancy diffusion to walls

In the Polák and Sauzay work, their goal was to connect vacancy generation in PSBs to extrusion and intrusion growth on metal surfaces. They posited that the vacancies generated in PSB channels migrate to walls where they are rapidly transported to surfaces leading to formation of intrusions and extrusions. This assumes that vacancy diffusion to walls is a significant mechanism for vacancy annihilation; however, vacancy diffusion can be

Table 3.1: Diffusion coefficients in Ni as a function of T

$D_v(m^2s^{-1})$	T (K)	source
8×10^{-27}	300	This work
4.44×10^{-23}	773	Wazzan [99]
7.76×10^{-17}	1195	Maier et al. [100]

very slow, and thus this mechanism may only contribute significantly to vacancy annihilation at high homologous temperatures. In this section, we investigate this postulate by calculating the room temperature diffusivity of vacancies by use of the nudged elastic band (NEB) method. In addition, we make comparisons to available experimental data at higher temperatures.

To calculate the prefactor for the vacancy diffusivity, the Eyring equation [97] is employed, as has been studied in first principles calculations of vacancy diffusivities [98]. In this calculation we require the activation energy, ΔE, to calculate the jump frequency

$$\omega = \frac{k_B T}{h} \exp^{-(\Delta E/k_B T)} \tag{3.13}$$

where h is Planck's constant. The activation energy for vacancy migration, calculated by NEB, is 0.868 eV.

Using this value we obtain $D_v = 8 \times 10^{-27} m^2 s^{-1}$ at 300K. This compares favorably to experimental data on higher temperature samples. The lowest temperature value presented by Wazzan was $D_v = 4.44 \times 10^{-23} m^2 s^{-1}$ at 773K [99] and a study from Maier et al. found $D_v = 7.76 \times 10^{-17} m^2 s^{-1}$ at the higher temperature of 1195K [100]. These values are collected in Table 3.1. The calculated diffusivity is very low, suggesting that vacancy diffusion occurs primarily through a process other than lattice diffusion at low temperatures. This is not to say that vacancies in PSBs do not diffuse. For $D_v = 10^{-27}(m^2 s^{-1})$ it would take a vacancy roughly 1 hour to diffuse a distance of 1 micron. Rather than direct diffusion there may be another process governing the effective diffusivity, as discussed in the next section.

3.3.3 Pipe diffusion

While diffusion at low temperatures is very slow, there may be alternative ways in which vacancies can be transported. Pipe diffusion [101, 102], or accelerated diffusion along dislocation cores, provides one possible mechanism. Self diffusion coefficients along dislocations have been measured in Al by measuring the volume change of large voids which are connected to a surface by a dislocation line [102]. In addition, diffusion coefficients of impurity atoms along dislocations in Al have been measured to increase relative to the bulk by about 4 orders of magnitude [103]. In Ni, self diffusion coefficients have been measured along edge dislocations lines by measuring surface accumulation of vacancies. At 800K diffusion coefficients of $10^{-12}\frac{\mathrm{m}^2}{\mathrm{s}}$ have been observed [104]. In addition, diffusion coefficients of $10^{-11}\frac{\mathrm{m}^2}{\mathrm{s}}$, also at 800K, have been measured along screw dislocations in dislocation dynamics simulations [105]. This is a difference of 11 or 12 orders of magnitude compared to self diffusion coefficients measured in pure Ni [99]. Of the presented mechanisms this provides the most feasible mechanism that can account for significant vacancy annihilation. It is possible that dislocations are pinned at voids in the channels, providing a connection to the dislocation walls. Vacancies can then diffuse along this network from the channels, into the dislocation walls, and eventually to surfaces.

3.3.4 Conclusion

Analysis of the proposed vacancy annihilation mechanisms reveals that direct diffusion and annihilation mechanisms are likely very slow and thus are unlikely to contribute significantly to vacancy annihilation. Static Frenkel pair recombination is likely to only play a significant role in point defect annihilation at very high concentrations. Direct vacancy diffusion near room temperature is quite slow as well indicating that direct diffusion of vacancies to dislocation walls from inside channels occurs very slowly (on the time scale of hours). Pipe diffusion provides a possible mechanism for enhanced vacancy diffusivity. It has been observed that pipe diffusion may increase diffusivity 4 orders of magnitude in Al.

It is possible that screw segments spanning the channels are pinned to voids in the channels and subsequently act to pipe vacancies to the dislocation rich walls, which are ultimately transported to surfaces. With this possible mechanism in mind, in the current implementation we choose the simple linear model for vacancy annihilation ($c_v^- \propto Ac_v$), leaving open the possibility of incorporating pipe diffusion based more directly in the future.

3.4 Model implementation and simulations

The vacancy balance model described in the previous section has been implemented along with a H transport model into a microstructure-sensitive crystal plasticity (MS-CP) model [34]. A goal of this MS-CP approach is to incorporate micro-scale and meso-scale mechanisms so that the model may be informed from the bottom up by lower scale simulations. In addition, this allows explicit tracking of dislocation substructure and of defect densities. The MS-CP model is fit to experimental data for single crystal Ni [106]. The governing vacancy balance equations, restated here for continuity, are solved using inputs from the MS-CP calculation. The concentration of vacancies generated by dislocation loop annihilation is determined by

$$\begin{aligned} \dot{c}_v^+ &= \Phi_{ann} y_s^{edge} (\rho^+)^2 \\ \frac{\partial \rho^+}{\partial t} &= \frac{\rho_{act}}{l_s \rho b} \dot{\gamma} \\ \rho_{act} &= \frac{\rho^0}{2} \left\{ 1 + \left[\frac{\tau - \bar{\tau}}{\sqrt{2}\sigma} \right] \right\} \end{aligned} \tag{3.14}$$

Equations 3.14 are solved in ascending order starting with the density of activated sources. The time integration is carried out via forward Euler integration [107]. Along with the vacancy production equations we calculate the number of vacancies annihilated by

$$\dot{c}_v^- = Ac_v \tag{3.15}$$

and the total vacancy concentration is given by a sum of the annihilation and production

components, i.e.,

$$\dot{c}_v = \dot{c}_v^+ - \dot{c}_v^- \tag{3.16}$$

Values for τ, ρ, and $\dot{\gamma}$ can be directly obtained from the MS-CP calculation. All of the additional variables are estimated or calculated directly. Outputs from the MS-CP calculation are used in the vacancy balance model to generate the change in vacancy concentration. This can then be fed back into the MS-CP module for use in the next step.

3.4.1 Estimation of model parameters

The Φ_{Ann} parameter describes the number of vacancies produced by the annihilation of two bowed out edge dislocation segments and the subsequent non-conservative jog dragging of the remaining screw dislocation segments. This can then be estimated by adding the length of the annihilated edge segment, D, and the average irreversible slip distance for a screw segment spanning a channel, L_{irr} , which can be estimated [108] as

$$L_{irr} = \frac{1}{2y_s\rho_s} \tag{3.17}$$

If we take $D \approx 1\mu m$, $\rho_s = 10^{13}m^{-2}$, and $y_s = 50nm$, then $\rho_{line}(L_{irr} + D) \approx 1900$ vacancies with ρ_{line} being the atomic density along the edge dislocation line direction for an FCC lattice. This states that if a jog is drug along the edge dislocation line direction for a distance $L_{irr} + D$ then with an atomic density of ρ_{line}, roughly 2000 vacancies are generated.

The additional required parameters include information regarding the source densities and strengths which we estimate based on other work [84, 109]. We require that the source density is smaller than the total dislocation density in the walls, and the critical bow out length is estimated from experimental results and coarse grained atomistic simulations [109]. The remaining model parameters are consistent to first order with values in

Table 3.2: Parameter values used in the vacancy balance model

$\bar{\tau}$ (Pa)	10^8	Φ_{ann}	1000
σ (Pa)	$2 * 10^7$	dt (s)	0.003
ρ^0 (m^{-2})	10^{10}	l_s (m)	$5 * 10^{-9}$
y_s^{edge} (m)	$6 * 10^{-10}$	A	0.1
b (m)	$2.5 * 10^{-10}$	C_n	$4 * a_0^{-3}$
a_0 (m)	$3.52 * 10^{-10}$		

similar work [29]. These parameters are relevant for simulations at 300K. The full set of parameters is listed in Table 3.2.

3.4.2 Model implementation in crystal plasticity

The vacancy production model has been implemented into a modular MS-CP code, based on a previously developed constitutive framework [34], along with a H transport model, which is based on a heat equation [110], and a trapping (including dislocations and vacancies) model [35]. Vacancy production enters this framework, illustrated in Figure 3.3, in the Crystal Plasticity User MATerial subroutine (CP-UMAT). A significant goal of the EICEM program is the development of the modular CP-UMAT along with modules to incorporate vacancy production and H transport. This work is done as a part of the broader EICEM program in collaboration with Theodore Zirkle, who developed the CP-UMAT code and implemented the additional modules. Together these modules facilitate FEM calculations that integrate microstructural information via the MS-CP model [34], vacancy production by implementation of the method described here into the UMAT, and hydrogen transport in the UMATHT (UMAT Heat Transfer) module.

The UMATHT module is used to cast the H diffusion problem as a heat equation so that

$$\frac{\partial c_H}{\partial t} + \nabla \cdot \mathbf{J} + r = 0 \tag{3.18}$$

where c_H is the H concentration, **J** is the H flux, and r is the source/sink rate for H [111].

This module is solved along side the MS-CP UMAT, allowing for the coupling of the H transport with the vacancy evolution. Later in this section, effects of this coupling are studied in the regions around a blunted crack tip and results are shown in Figure 3.8.

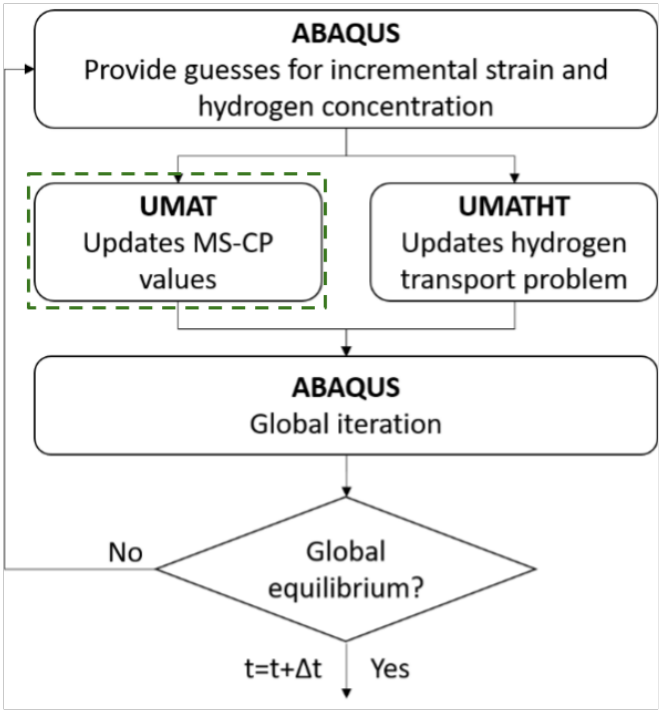

Figure 3.3: Flowchart outlining the full FEM calculation, including integrated modules. The green box indicates the location of the vacancy production module in this framework.

A goal of this implementation is to exercise the physically-informed CP-FEM model to understand the role of vacancies and H on crack tip plasticity and their role in fatigue crack growth. To this end we focus on studying the vacancy fields around a crack tip in Ni. In the following, the crack is oriented so that the crack plane is on the (001) surface and the crack front lies along the $[0\bar{1}0]$ direction. Initial cyclic loading simulations have been run to measure the effect of the vacancy production model as a function of distance from a crack tip. The simulations are run for 2 cycles at $K_{max} = 30$ ksi $in^{1/2}$, $K_{min} = 21$ ksi $in^{1/2}$, and $R = 0.7$. Values for the vacancy concentration per slip system as a function of the simulation time step are measured at 3 positions, illustrated in Figure 3.4 in the simulation cell. One computed result is recorded very near the crack tip, another in the damage region

ahead of the crack, and another in the far field. In the CP calculation the vacancy production model is calculated for each slip system. The output values for $\dot{\gamma}$ and ρ from the CP-UMAT that are used in vacancy production model (Equations 3.14) are per slip system values. As such the calculated dislocation density due to activated sources is also calculated per slip system. Results for all 12 slip systems are shown in Figure 3.5.

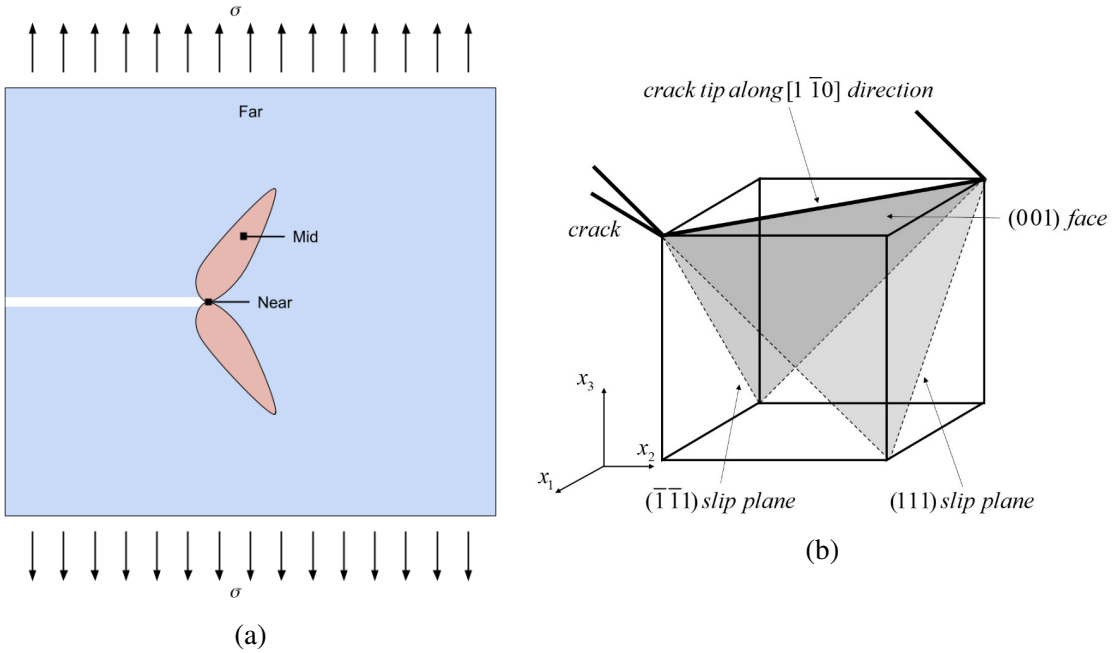

Figure 3.4: A schematic of a crack tip, illustrating positions around the crack where vacancy concentrations are sampled (a). The red plumes indicate high stress regions along the primary slip system ahead of the crack tip. The 'Near' point is located very close to the crack tip, in a high stress region, the point labeled 'Mid' is in the damage region ahead of the crack tip, and the 'Far' point is measured away from the crack tip in a region of low plastic strain. These regions correspond to the data shown in Figure 3.5. The crack tip orientation used in the simulations is shown in (b).

Only two slip systems tend to contribute significantly to the vacancy concentration in each case. As may be expected from the model formulation, these are the slip systems with the highest dislocation densities. Vacancy concentration is presented here as the dimensionless quantity N_v/N_s (the number of vacancies per lattice site). Vacancy concentrations near the crack tip reach very high levels of around 10^{-3}, with concentrations of roughly 10^{-6} in the damage region and 10^{-12} in the far field. Bulk experiments have measured vacancy

concentrations due to plastic deformation to reach orders of magnitude in the range of 10^{-4} down to 10^{-6} in Cu [75, 13, 12]. In Ni, specimens deformed under high pressure torsion (HPT) reach concentrations on the order of 10^{-4} [112, 113]. The value measured near the crack tip in this simulation exceeds these experimentally measured values; however, it should be understood that the experimental measurements capture the bulk concentration. It is expected that local concentrations higher than those observed in the bulk occur in regions under very high stress, such as near a crack tip. Within this simple simulation, observed values appear reasonable in the context of available experimental data.

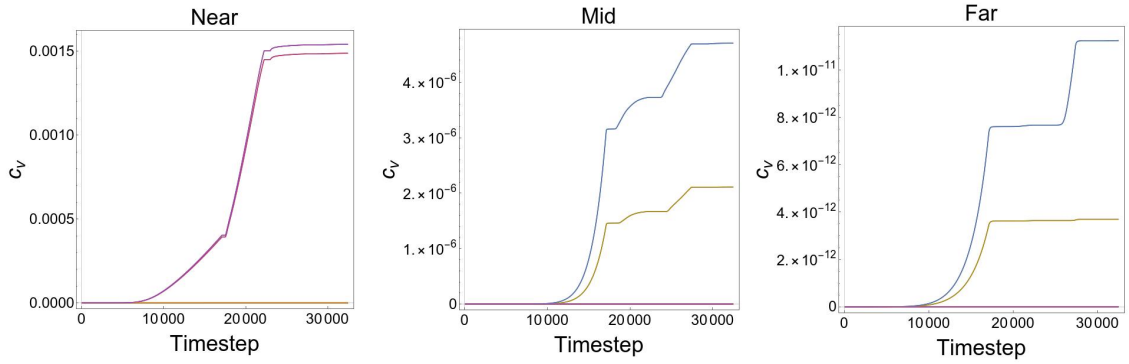

Figure 3.5: Vacancy concentration vs time step for data obtained from an MS-CP calculation in the near field close to the crack tip ('Near'), the damage region ahead of the crack('Mid'), and the far field ('Far'). All slip systems are shown. Only two contribute significantly to the vacancy concentration.

In addition, this CP-FEM framework has been exercised in monotonic loading with the same crack tip geometry to study the characteristics of each component of the model. The MS-CP model [34] is calibrated with data from single crystal Ni [106]. The simulation mesh is split into two domains, one in the near field around the crack tip which utilized the MS-CP model, and another in the far field which employs a J_2 plasticity model [114]. The crack tip radius is 8 μm and the simulations are run at 300K. The vacancy concentration is measured as a function of radial position around the crack tip. The mesh geometry as well as the positions at which measurements are taken are shown in Figure 3.6. The line in the figure shows the arc along which the vacancy concentration is measured.

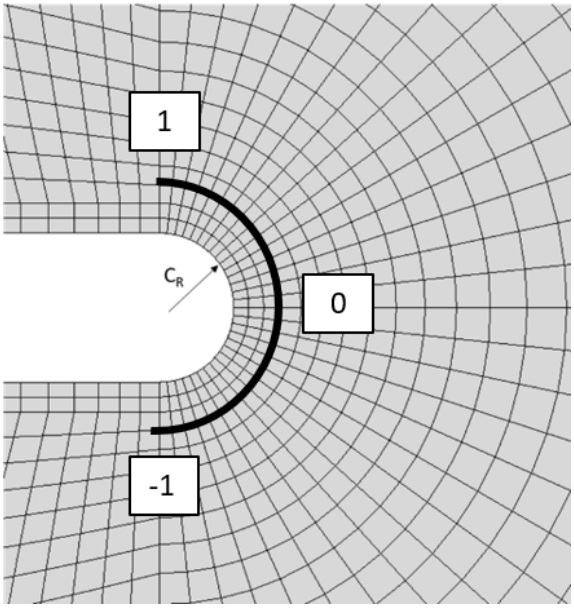

Figure 3.6: Crack tip mesh showing the location of the radial measurements (curved line labeled with -1, 0, 1).

The vacancy generation ahead of the crack tip was computed by loading to a stress intensity factor of 20 MPa-m$^{1/2}$ over 200 s. Vacancy concentration is computed on four slip planes: (111), $(1\bar{1}\bar{1})$, $(\bar{1}\bar{1}1)$, and $(\bar{1}1\bar{1})$. Data for both the vacancy concentration (a) and the dislocation density (b) is shown in Figure 3.7. The two dominant planes, the (111) and $(\bar{1}\bar{1}1)$ planes, are on the primary slip planes associated with the prescribed crack orientation [115]. Additionally, the peaks in the vacancy concentration are oriented at about 55 degree angles relative to the crack plane, closely matching the orientations of the (111) and $(\bar{1}\bar{1}1)$ planes (54.7 degrees) [115].

One role vacancies play in metals is as strong H traps [116, 117]. To investigate the interplay between vacancies and H, a trapping model [116] has also been implemented into the CP-FEM framework. The trapped H concentration is given by

$$C_T = \frac{\alpha_T N_T C_M K_T}{C_M(K_T - 1) + \beta N_L} \tag{3.19}$$

where α_T is the number of H atoms per trap site, β is the number of atoms on a normal lattice site, N_T is the molar trap density, K_T is the equilibrium rate constant, and C_M is the

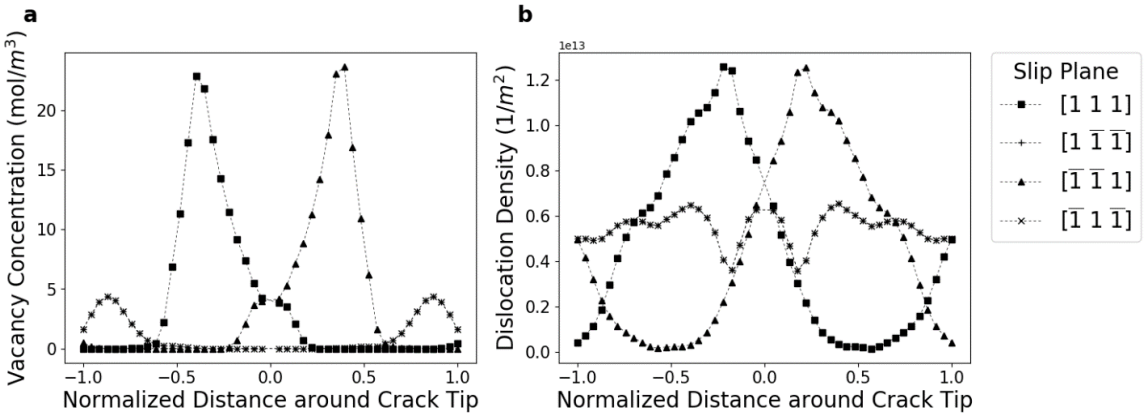

Figure 3.7: Vacancy concentration (a) and dislocation density (b) measured as a function of radial position (shown in Figure 3.6) around the blunted crack tip. Different markers correspond to different slip planes.

mobile H concentration. The mobile H concentration as a function of radial position around the crack tip has been calculated for three different scenarios: in the first it is assumed that there are no vacancies (0 C_{Va}), in the second the vacancy production model is used to generate the vacancy concentration, C_{Va}, and in the third the vacancy concentration generated by the model is elevated by a factor of 10 (10 C_{Va}). Data are shown in Figure 3.8. In addition to the mobile H concentration, the points corresponding to the maximum dislocation density (Max ρ) and the minimum and maximum trapped H concentrations (C_{HVa}) are shown.

As expected, with vacancy production turned off, the amount of mobile H is high; with vacancy production elevated, the mobile H density decreases. Interestingly, in the case with no vacancies, H transport appears to be dominated by pipe diffusion and convective transport, as the maximum in the mobile H concentration coincides with the maximum dislocation density. At the other extreme (elevated vacancy concentrations), the maximum in the mobile vacancy concentration corresponds to the minimum trapped H concentration, indicating that localization of vacancies tends to allow for higher mobile H concentrations in regions with low vacancy concentrations. Results at these two extremes provide insight into the role played by the localization of vacancy production around cracks. The data

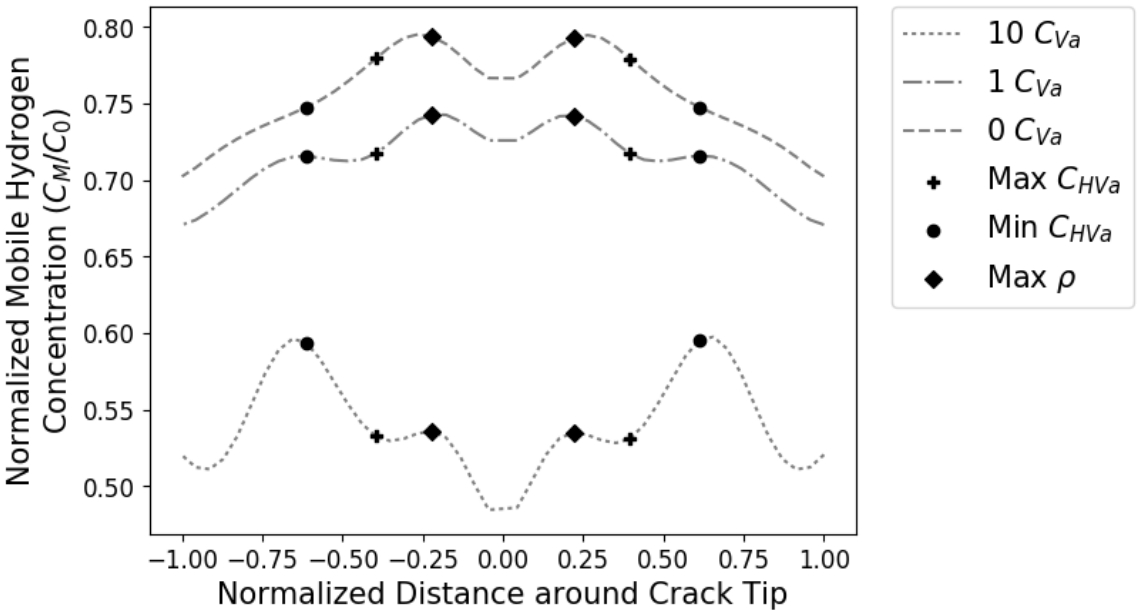

Figure 3.8: Normalized mobile H concentration around a crack tip. The points labeled Max ρ, Max C_{HVa}, and Min C_{HVa} correspond to direction of maximum dislocation density, maximum trapped H concentration and minimum trapped H concentration respectively.

corresponding to the vacancy production model represents a competition between the two effects observed at the extremes. A small local maximum is still observed in the direction associated with the minimum trapped H (consistent with the high vacancy case) and another maximum is observed corresponding to the maximum dislocation density (consistent with the no vacancy case). These two effects indicate that, at moderate vacancy concentrations, there is competition between localization of H transport in regions of high dislocation densities (when vacancy concentrations are low) and to regions of low vacancy concentration (when vacancy concentrations are high). In scenarios with a high number of vacancies being generated (high plastic strain), such as near a crack tip, vacancies act as the most significant traps for H and thus H-vacancy clustering effects dominate the HE response. Mechanisms like HESIV dominate in this regime. Under conditions with lower vacancy concentrations, dislocations act as the most significant trap in the system and H transport is enhanced. H is then transported more broadly into the bulk material and mechanisms like HEDE (with H segregated into boundaries) may play a more significant role.

3.4.3 Conclusion

In this Chapter, a new model is presented to incorporate the production of vacancies by annihilation of dislocation loops, inspired by previous models in PSBs, into a modular CP-FEM framework. The production term is based on the bow out of dislocation loops from PSB walls and their subsequent colinear annihilation in the channels. Several mechanisms for the annihilation of vacancies are discussed with the conclusion that the most likely mechanism is pipe diffusion of vacancies along dislocations. Together, the production and annihilation terms yield the total rate of change of the vacancy concentration. This model has been implemented in a modular CP-FEM framework which uses a MS-CP model along side modules for the transport and trapping of H. Under cyclic loading, the vacancy production module results in distributions with high vacancy concentrations very near the crack tip, shown in Figures 3.4 and 3.5. Exercising this framework to study trapping and transport of H around a blunted crack tip under monotonic loading reveals significant competition between promotion of H transport in regions of high dislocation density and suppression of H transport by high localized vacancy concentrations, shown in Figures 3.6, 3.7, and 3.8. This model, integrated into the CP-FEM framework, will be used in other parts of the EICEM program to study cyclic loading, building on the monotonic calculations presented here.

CHAPTER 4
HYDROGEN-VACANCY COMPLEX FORMATION AND NANOVOID NUCLEATION

In Chapter 2, the segregation of H to energetically favorable sites was studied, particularly its interaction with dislocations. The previous chapter focused on the generation of vacancies during plastic deformation. In this final chapter, we link these concepts together to study the role of H on vacancy clustering and nanovoid formation. As previously noted, it has been observed in experiments that the accumulation of plastic deformation in metals is accompanied by vacancy concentrations that are significantly higher than equilibrium concentrations [75, 13, 118, 14]. Elevation of the vacancy concentration can be particularly pronounced when H is present [118, 20], as H is believed to stabilize vacancies by reducing their formation energy. With high concentrations of vacancies being produced by plastic deformation, as discussed in the previous chapter, and considering the stabilization effect of H, it is expected that H-vacancy clusters are numerous in highly strained regions and play a significant role in HE [15] by reducing shear ductility.

Complementing the role of H in stabilizing vacancies, vacancies act as significant traps for H [116]. Using the Angelo Ni system as an example, the binding energy of an H atom to the most energetically favorable site around an extended edge dislocation is about -2.32 eV. Noting that the bulk binding energy of atomic H to an octahedral interstitial site is -2.19 eV, the maximum (on the most favorable site) segregation energy to this dislocation is -0.13 eV. For a broken octahedral site inside a vacancy in the same Ni-H system, the binding energy is -2.38 eV, or a segregation energy of -0.19 eV. Dislocations are typically believed to be strong trapping sites for H, but (at least in the case of this system) vacancies are even more significant traps. Density Function Theory (DFT) calculations have revealed that vacancy-H complexes may contain up to 6 H atoms [30, 31], with some material dependence [32,

118, 20]. More recently it has been suggested that in some cases VaH_2 clusters are most favorable [33], particularly in α-Fe, while other studies suggest that up to 6 H atoms can be accommodated within a single vacancy in a variety of FCC metals [32]. These simulations provide valuable insights into the nature of trapping of H by vacancies, but are generally limited to single or di-vacancies. Additionally, they focus on the role that these vacancies play in influencing the availability (or trapping) of lattice H.

Here we consider a different aspect, studying the role of H on vacancy cluster formation. In addition, we extend from single and di-vacancies up to large vacancy clusters. We draw inspiration from the radiation damage literature in which large void clusters are often observed. For example, in 304 stainless steel under deuterium bombardment, void clusters with sizes of up to 127 Å have been observed at 450 °C [119]. At similar temperatures but under neutron irradiation, clusters of up to 250 Å have been observed [120]. In Ni at 480 °C, 250 Å diameter voids have been observed, also under neutron irradiation conditions [121]. Under irradiation conditions it is expected that very high point defect concentrations are present. As such, these void cluster sizes provide an upper bound on what may be expected for void growth due to plastic deformation. As a point of comparison, the largest void clusters analyzed in this study have a diameter of roughly 35 Å.

We begin with the studies on the effect of H on the formation energy of small (containing up to 15 vacancies) H-vacancy clusters by two different methods. These methods then form the basis for a hybrid calculation method with the goal of simulating larger cluster sizes. Formation energies are then calculated for nanosized clusters (up to 500 vacancies) generated by this hybrid MC/MS simulation. The role of H on the formation energy is studied in the context of its effect on the surface energy of a void. Through this analysis, we calculate a H-affected surface energy. At the end of this chapter, application of this data to consider the aggregation of vacancies into nanovoid at the mesoscale is discussed.

4.1 Formation energy of small vacancy clusters

For single or di-vacancies, it is has been shown that H plays a role of lowering the formation energy, thereby stabilizing void formation and growth [118]. While the stabilization effect of H has been quantified in calculations for single vacancies and very small clusters [33, 122], this has not been extended to larger cluster sizes. The formation energy of a vacancy cluster [123] for a Ni-H system can be calculated as

$$E_f = E[(N-n)\text{Ni} + m\text{H}] - (N-n)E_{coh} - mE_{\text{H}}^{bulk} \tag{4.1}$$

where $E[(N-n)\text{Ni} + m\text{H}]$ is the energy of the system containing N lattice sites with a vacancy cluster of size n and with m H atoms, E_{coh} is the cohesive energy of Ni, and E_H^{bulk} is the binding energy of a H atom to a bulk interstitial site in the Ni lattice. This expression compares the total system energy containing a vacancy-H cluster with the energy of a crystal with n (unclustered) vacancies, and compares the binding energy of H in vacancy sites to that in bulk interstitial sites. Thus, this accounts for the energy differences between a random distribution of vacancies and a cluster of vacancies, as well as the segregation energy of H to vacancy sites from bulk sites. The cohesive energy is a property of the interatomic potential, while the H binding energy must be calculated. This can be done, as described in Chapter 2, by comparing the total energy of a simulated crystal with and without a single H atom. The difference in energy of these systems is the H binding energy. In this system, H preferentially occupies octahedral sites in the bulk, thus, E_H^{bulk} is taken to be the binding energy to an octahedral site in an otherwise perfect crystal. All that remains to be calculated with regard to the formation energy is the first term that accounts for the total energy of the vacancy-H cluster.

In the following, we work through several methods for computing $E[(N-n)\text{Ni} + m\text{H}]$ and the resultant cluster formation energy. We start with a MS-based method and a more flexible MC method for small (fewer than 15 vacancies) clusters. These methods are

thorough and require few approximations, but have high computational cost, especially if they were to be applied to larger clusters. We then outline a method for constructing larger clusters by driving the cluster growth toward an energy minimum and only applying MC sampling to the H distribution. The results of these calculations are then discussed in the context of power law relations for modeling the formation energy. An H-affected formation energy is calculated by fitting the obtained data to these models. In the last section, we outline the use of these models to inform mesoscale dislocation dynamics simulations by incorporating H effects in a nanovoid nucleation criterion. The H-affected formation energy is then implemented in a MC sampling scheme and can be used to study the effect of H on the clustering of vacancies. Implications of the H effects on the critical void size for nanovoid nucleation are discussed.

4.1.1 MS for small clusters

Initially we perform a MS-based calculation aimed at generating small vacancy clusters containing up to 12 vacancies. H is introduced into the small clusters at various concentrations and the formation energies are calculated. In this method, we start with a perfect, defect free lattice. One atom is removed to create a single vacancy. The first nearest neighbor atoms to the vacancy are then all added to a group. From this group, n atoms are selected randomly and deleted, generating a Vac_n cluster. H atoms are then added into the region around this cluster and the structure is energy minimized resulting in a $\mathrm{Vac}_n\mathrm{H}_{m*n}$ cluster. Here, m is the number of H atoms per vacancy and n is the number of vacancies comprising the cluster. For each value of m and n the simulation is run 100 times and the formation energy is calculated from an average energy over the 100 runs. A schematic of this process is shown in Figure 4.1.

This MS calculation is run in LAMMPS [64] for systems ranging from 1 to 12 vacancies per cluster with 0 to 6 H per vacancy, distributed randomly in the vacancy cluster. Minimization is carried out using conjugate gradients employing the Angelo EAM poten-

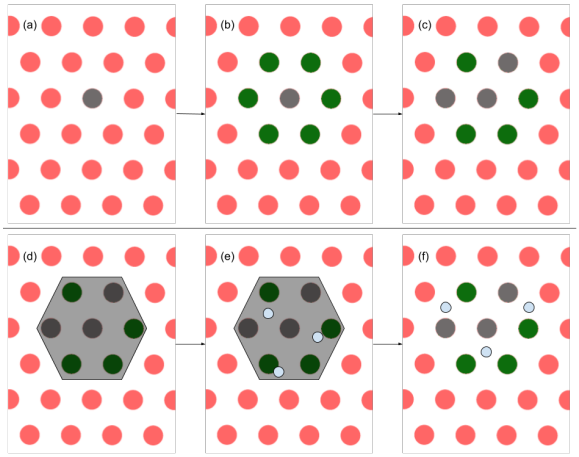

Figure 4.1: A schematic of the MS method for vacancy generation and H addition. Starting from top left (a), a single vacancy, the grey circle, is added to an otherwise perfect lattice. The neighboring atoms, green circles, around that vacancy are selected (b) and a random set is deleted to generate the vacancy cluster (c). H atoms, the light blue circles, are then added into the region contained by the vacancy cluster, shown in (d) and the structure is energy minimized allowing the H atoms to relax into interstitial positions (f).

tial [62] for Ni-H, which is used in previous sections as well. Data are shown in Figure 4.2. The formation energy decreases sharply with 1 H per vacancy relative to the case with no H. With 1 H per vacancy, the formation energy decreases relative to the bare vacancy. Increasing the number of H per vacancy then increases the formation energy. For values of 5 and 6 H per vacancy, the formation energy exceeds the 0 H case.

Lower formation energies for 4 and fewer H per vacancy indicates that up to 4 H per vacancy are favorable relative to the 0 H case, with 1 H per vacancy being the most favorable, as it has the lowest formation energy. With 5 and 6 H, per vacancy the formation energy is higher. This indicates a lower relative stability when compared to the bare vacancy. This is not fully consistent quantitatively with the DFT results for single vacancies but retains some of the qualitative features. H lowers formation energy relative to the 0 H case up to 4 H per vacancy, but beyond this threshold the formation energy becomes unfavorable. The formation energy tends to increase linearly with increasing vacancy number; however, in these simulations the 5 and 6 H cases appear to increase in slope at between 8 and 10 vacancies. This is because the number of possible H sites does not scale linearly

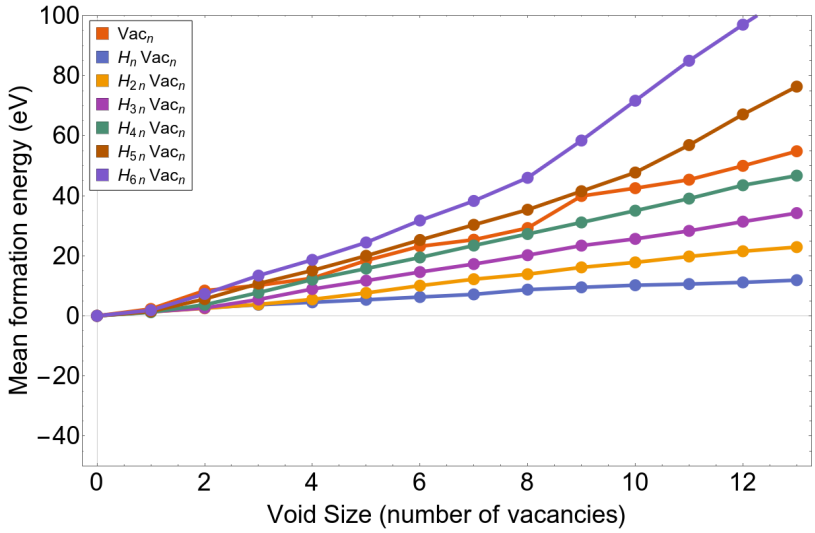

Figure 4.2: The formation energy of various H vacancy clusters calculated from equation 4.1 using data from the MS method.

with increasing void size (number of H sites $\neq 6 * n$) but instead the number of H sites per vacancy decreases with increasing void size (number of H sites $\leq 6 * n$). As a void grows, the H sites are dominated by the available surface sites and the interior vacancies do not contribute any sites at all. Thus, in larger voids the number of H sites is greatly reduced compared to the number of available sites for individual vacancies (6 sites per vacancy or $6 * n$). This will be discussed in more detail in Section 4.2.3.

While these simulations provide good estimates for the formation energy, there are some limitations to this method. Most notably, the vacancy clusters generated in this way are restricted in their configuration. Since atoms can only be removed from the region neighboring the initial vacancy the cluster is always compact. The possibility of no clustering (randomly distributed vacancies) is thus not admitted in this situation, which may not always be correct. Creating the clusters in this way allows the simulation to skip explicit MC calculations regarding the vacancy structure in order to save time. This is what allows for the large number of runs and generates smooth data, but this approximation is somewhat artificial. In addition, H is only added to the interior region of the vacancy, not allowing for the possibility of H populating of the exterior octahedral sites around the vacancy. The

binding energy to these nearest extremal sites in the Ni-H system is -2.26 eV, or a segregation energy of -0.07 eV. This is less favorable than that of the most favorable sites around the extended edge dislocation, but is still a favorable site relative to the bulk, indicating that some H will likely occupy these nearest external sites. In the following section, we address these issues by pursuing explicit MC calculations.

4.1.2 MC for small clusters

To allow for more flexibility in the simulations, we use a hybrid MC-MD approach to calculate the structure of the vacancy-H cluster. This is done by initially preparing a perfect Ni crystal with a sublattice of unoccupied octahedral H sites. To incorporate these unoccupied sites into the simulations, a vacant site type element was added into the Angelo potential. This is done by adding an element type which does not contribute to the energy and has no interaction with other element types. The sites of this vacancy type are fixed in position during the simulations. Next, n Ni vacancies are introduced into the system by swapping occupied Ni atoms with vacant type elements. Similarly, m H atoms per Ni atom are added on the sublattice by swapping unoccupied sublattice points from vacant elements to H type. This results in a structure containing n vacant Ni sites and $m*n$ H atoms located on octahedral interstitial sites.

After the initial structure is prepared, MC swaps are attempted. Ni and vacant elements are swapped on Ni lattice sites and H and vacant types are swapped on the sublatice. A trial swap is accepted or rejected according to the Metropolis criterion [124, 125], which accepts a trial step with probability

$$p = \begin{cases} 1 & \text{if } \Delta\Phi \leq 0 \\ exp(-\Delta\Phi/k_B T) & \text{if } \Delta\Phi > 0 \end{cases}$$

where $\Delta\Phi = \Delta E$ is the change in energy due to the swap. After a full MC step, MD steps are run to allow for the system to relax. MD simulations are run at 10K, which allows

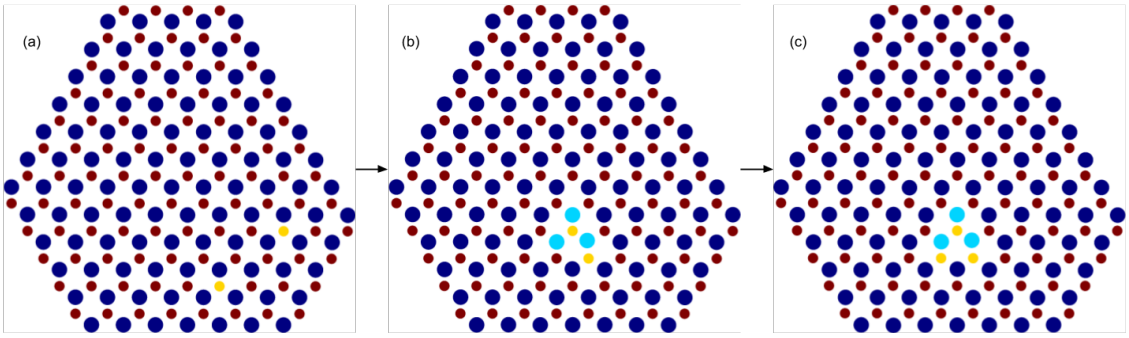

Figure 4.3: A schematic of the formation energy calculated by the full MC method. A perfect lattice (blue points) is produced with a sublattice of vacancy H sites in octahedral interstitial sites (red points) shown in (a). H atoms (yellow points) are added to the sublattice and vacancy type elements to the main lattice (light blue points) shown in (b). The entire structure is allowed to relax by attempting MC swaps of H atoms with vacant H sites (red and yellow points) and the Ni atoms with vacant lattice sites (blue and light blue points), illustrated in (c).

for some relaxation but is purposefully chosen to inhibit too much rearrangement. If the atomic sites were to undergo significant rearrangement, it is possible that the underlying H site sublattice and the Ni lattice could become misaligned, resulting in a dramatically decreased acceptance probability for H-vacant site swaps. Figure 4.3 illustrates the full calculation procedure.

Simulations of this type are run for cases of 0 to 15 vacancies ($n \in [0, 15]$) and for 0 to 6 H per vacancy ($m \in [0, 6]$). Due to increased computational cost of this full MC approach, only 1 simulation is run for each stoichiometry. This leads to significant noise in the results but general trends are still indicated. The results are shown in Figure 4.4. Relative to the 0 H case, all of the cases with H have lower formation energy. The formation energy decreases sequentially from 0 to 4 H per vacancy and appears to saturate at about 4 H per vacancy. The data for 4 to 6 H per vacancy appear clustered.

Here, the formation energy always decreases relative to the H free case, indicating that there is always some stabilization effect of H on voids. For high H, this saturates but does not increase and never exceeds the case with 0 H. This is inconsistent with the DFT results, which indicate that for high H per vacancy, the formation energy should increase beyond

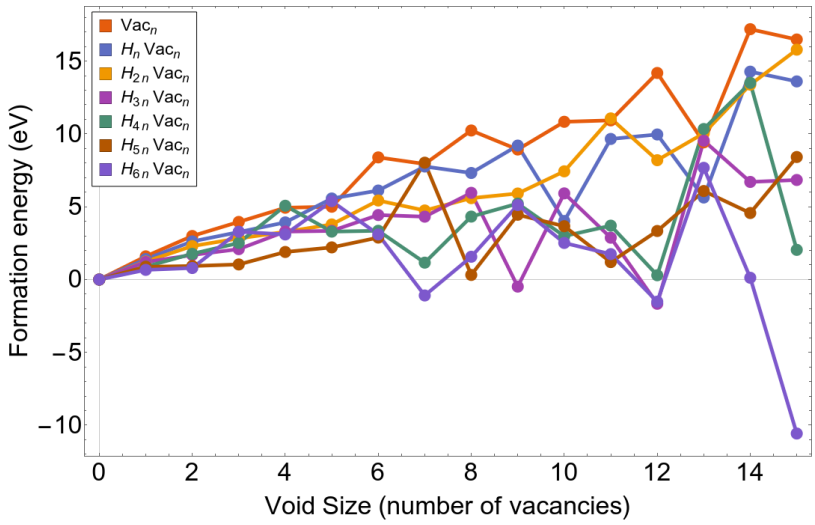

Figure 4.4: Formation energy calculated form Equation 4.1 using data from the full MC simulations.

a threshold value; after the vacancy is overfilled, inserting additional vacancies should be energetically unfavorable. However H is only placed on broken sites on the interior of a vacancy in the DFT calculation. In these simulations, H is allowed to distribute not only inside the void but also in any of the neighboring interstitial sites. Qualitatively, it is observed that for high H values (values of greater than 4 H per vacancy), H has a strong tendency to not only occupy interior vacancy sites but also the nearest external sites. These simulations indicate that although a single vacancy allows for up to 6 H on interior sites, it may allow for greater number of H if the first nearest neighbor external sites are also considered.

The full MC simulations provide a more flexible means of calculating the formation energy, but this method is not without limitation. Avoiding the approximations in the previous molecular statics calculations results in simulations which have a much higher computational cost. Accordingly, fewer runs are made and thus the results are much more noisy. This also restricts simulations to small cluster sizes. Despite these limitations, this method provides interesting qualitative results; while not fully consistent with DFT simulations they provide insight into the role of H on the formation energetics in small vacancy clusters. In the following sections, we introduce additional approximations intended to ease

the computational burden of computing the cluster structure while retaining the full MC approach to distributing the H field in and around the vacancy cluster. This can ultimately allow for study of a wider range of larger clusters.

4.2 A hybrid MS/MC approach for nanosized clusters

In this section we extend the previous small vacancy cluster calculations to larger sizes by invoking an approximate method for the growth of the vacancy cluster in the spirit of the previous MS calculation, but with the H field being estimated periodically by a full MC relaxation. This calculation is performed sequentially, so that as the vacancy cluster grows in size, H is added periodically and allowed to relax via MC sampling in this process. To begin, a perfect FCC Ni lattice is generated and one vacancy is created by removal of a single Ni atom. The resultant vacancy structure is then energy minimized. After minimization, the energies of each individual Ni atom in the system are output and the atom with the highest energy is removed from the system, adding a second vacancy to the cluster. Choosing to grow the void in this way is very fast and drives the system toward an energy minimum without need for explicitly searching for the minimum energy configuration [126]. It should be noted that although this process drives the vacancy toward an energy minimum, it is not necessarily the global energy minimum after relaxation. After a vacancy is added to the void, a sub-lattice of vacancy type atoms is added in all of the octahedral interstitial sites m H atoms are added onto this sublattice by swapping from vacant type elements to H type elements. From here, a full MC calculation is run, allowing the H and vacant type elements on the sublattice to swap. The Ni lattice (and thus the vacancy cluster structure) remain fixed in this calculation. Following the MC step, the H atoms are relaxed and the vacancy addition process is repeated, retaining the distribution of H atoms and vacant sublattice sites, by finding and removing the highest energy Ni atom. The calculation proceeds sequentially in this way until the desired $\mathrm{Vac}_n\mathrm{H}_{m*n}$ cluster is formed. A schematic of this method is shown in Figure 4.5.

This method borrows some strategies from the previous calculations in that it employs a MS method for the vacancy growth but retains a full MC run to determine the H distribution; there are some significant differences as well. Because MS is used in determining the void structure, this calculation is fast relative to full MC. This allows for calculation of very large void sizes, comprising up to 500 vacancies. In addition, because the H and vacancies are added in a sequential manner (every time a vacancy is added, H atoms are added as well), the concept of stabilization rate enters our considerations. By varying the rate at which H is added compared to the rate at which vacancies are added to the growing cluster, we can explore scenarios where growing clusters are experiencing different rates of H stabilization at identical stoichiometries. This will be discussed in more detail in Section 4.2.3.

4.2.1 Structure and formation energy of nanosized clusters

Simulations are run for clusters containing up to 400 vacancies. Initially, simulations are run for 0, 1, and 2 H per vacancy. In the initial runs, the H atoms are added into the simulation after each vacancy addition. For example, in the case of 1 H per vacancy, after the vacancy cluster is grown from 5 to 6 vacancies, 1 H atom is added, to increase the number of H atoms present from 5 to 6. MC swaps are then run on the H sublattice, allowing the 6 H atoms to relax into favorable sites. The formation energy is calculated using Equation 4.1, as before, and the results are shown in Figure 4.6. In addition to the formation energy data, we also consider the structure of the vacancy clusters. Images of the vacancy clusters are generated using Ovito [65].

Unlike in the previous simulations, the formation energy curves with H are quite wavy, indicating that there is something unusual or unexpected happening in the simulation. The formation energy for the case with 0 H follows a smooth curve and appears consistent with other similar simulations [126]. Visually, the cluster formed with 0 H is an octahedron (shown in Figure 4.7) with facets along the [111] surfaces. The blue elements in Figure

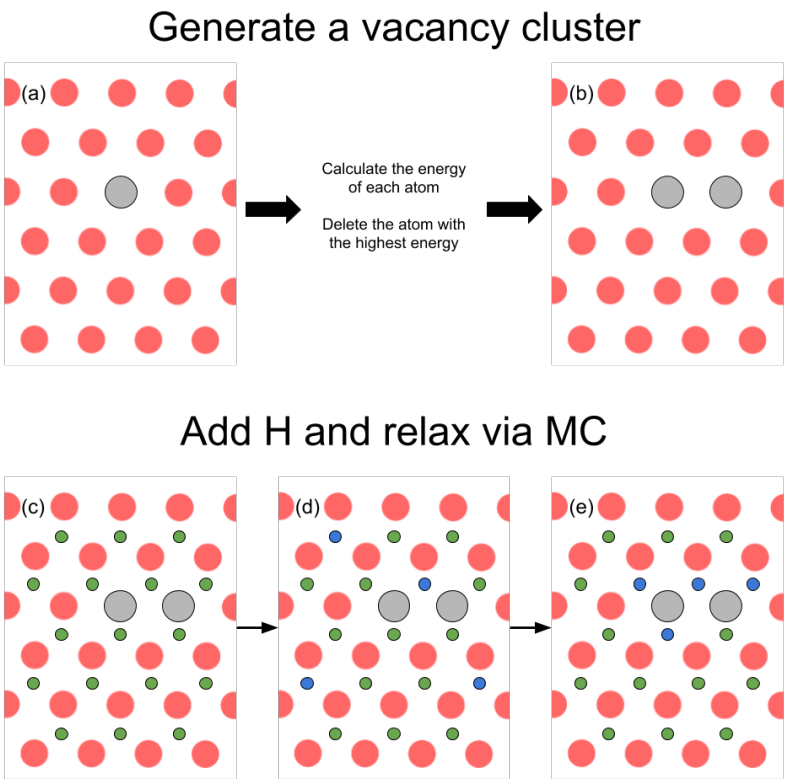

Figure 4.5: A schematic of the hybrid MS/MC method. The top illustrates the vacancy cluster growth. A single vacancy is generated (grey circle) in (a). The structure is energy minimized and the highest energy atom is removed (b), growing the vacancy cluster. In the bottom section the MC steps are illustrated. A sublattice of possible interstitial H sites is determined (c) and H atoms are added to random positions on the sublattice (d). The green circles represent the unoccupied H site sublattice and the blue circles represent sites which are occupied by H. The H field is relaxed around the existing vacancy cluster via MC swaps on the sublattice (e).

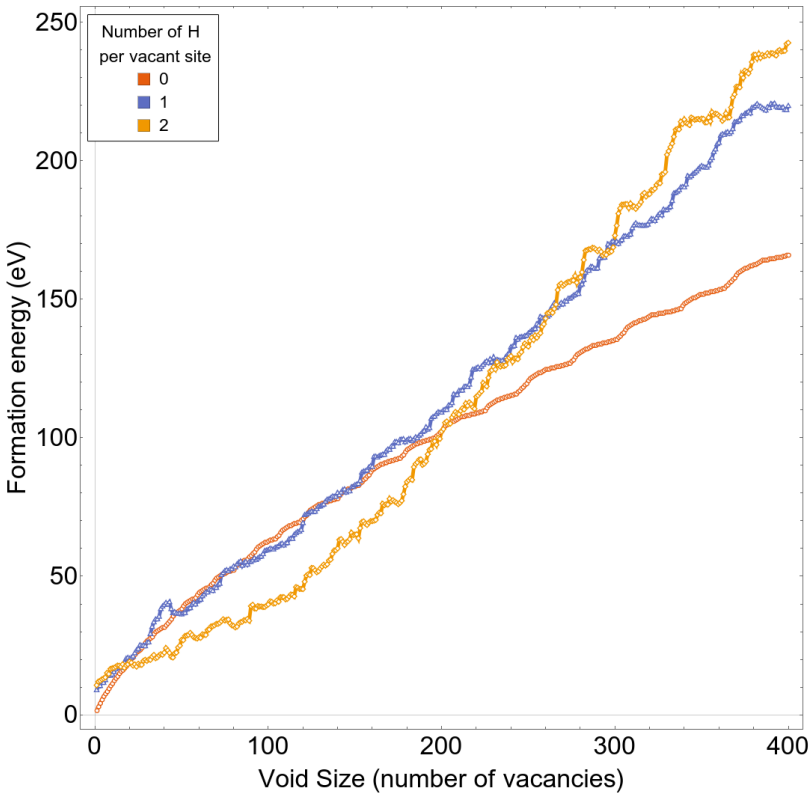

Figure 4.6: Formation energies of H vacancy clusters calculated from the MS/MC method. H is added in to the simulation the cluster is grown by one vacancy.

4.7 are vacant type elements, displaying the structure of the vacancies comprising the full vacancy cluster. Again this is qualitatively similar to observations in Nb [126] but geometries of this type have been observed in Cu near the cavitation point using a coarse-grained atomistic method [127]. Experimental TEM observations often reveal faceted voids in FCC metals under irradiation conditions [128] in a variety of materials.

In the cases with H, the situation is more complicated, as shown in Figure 4.8. As in the 0 H figure, the blue elements are vacancies but in Figure 4.8 the light yellow elements are H atoms distributed around the vacancy cluster. In the one H per vacancy case, the clusters are visually more linear, with H atoms settling on opposite sides of the vacancies, resulting in a sheet. In Figure 4.8(a) the sheet changes direction on the left and right ends. The cluster has grown to the edge of the box and thus has no more room to expand in the same direction. This is an artifact of the simulation and likely influences the form of the

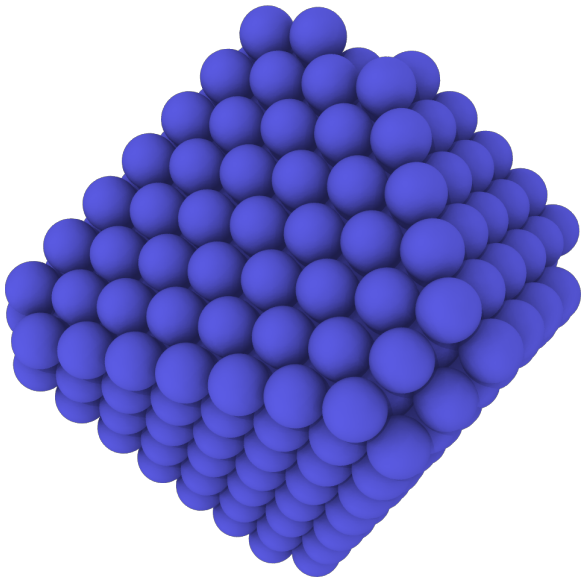

Figure 4.7: Geometry of a nanovoid with no H generated by the MS/MC method. The blue points are vacant lattice sites. The surfaces of the octahedron are along the $\{111\}$ planes.

formation energy curve. In the case with two H per vacancy, the clustering is more random in appearance; notably, the H atoms appear to cluster into a small hydride phase around the vacancy. This is sometimes observed in MC calculations but may only be physically reasonable at extremely low temperatures [69]. In this case it is likely that this H clustering has a substantial effect on the formation energy curve. These two clusters are qualitatively very different and it is difficult to draw any general conclusions. It appears that there are some difficulties with these simulation setups that warrant further investigation and refinement.

These simulations have some dependence on the rate at which H addition is performed. This set represents an extreme case of very rapid H addition. In this setup, the cluster grows by one vacancy upon which it is immediately stabilized by the addition of the corresponding amount of H. Perhaps this is possible in scenarios where void growth is slow or where H concentration is very high; in the model presented in Chapter 3, vacancy concentrations locally are likely very high relative to H concentrations. This suggests that cluster growth at lower H stabilization rates is more relevant in that model system. In the following section, we investigate the role of stabilization rate on vacancy cluster growth within this simulation

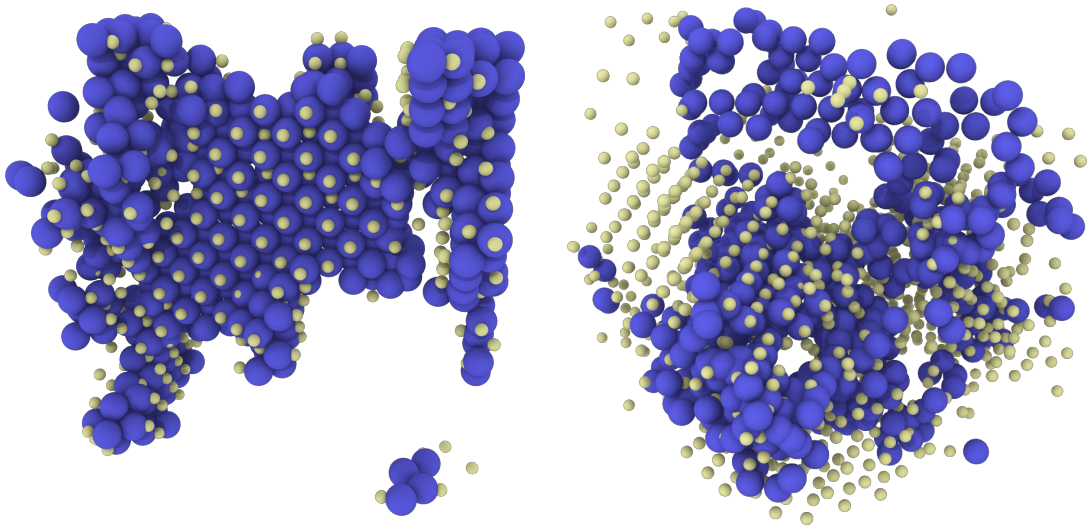

(a) 1 H per vacancy

(b) 2 H per vacancy

Figure 4.8: Geometries of nanovoids with H generated from the MS/MC method. Blue atoms are vacant lattice sites with light yellow point representing H atoms

framework.

4.2.2 Rate dependence of void structure and formation energy

To study the dependence of the void structure and formation energy on the rate of H addition, we consider two cases with H added at different stages during the vacancy cluster growth and compared to the case with 0 H. In one case, H atoms are introduced only after every 10th vacancy, and in the other only after every 20th vacancy is added to the cluster. For both cases, the number of H per vacancy is fixed at 1 for consistency. The new simulation procedure begins with a cluster of 10 vacancies, produced by sequentially removing the highest energy atom in the system. After each single vacancy is added to the cluster, the structure is energy minimized before another atom is selected and removed. At 10 vacancies, 10 H atoms are added to the sublattice of H sites and MC swaps between those sites are attempted, allowing for the H field to relax around the vacancy. The simulation then continues by adding 10 more vacancies as before and then 10 more H after until the cluster has reached 400 vacancies. From these data, the formation energy is calculated and are shown in Figure 4.9 as a function of void size.

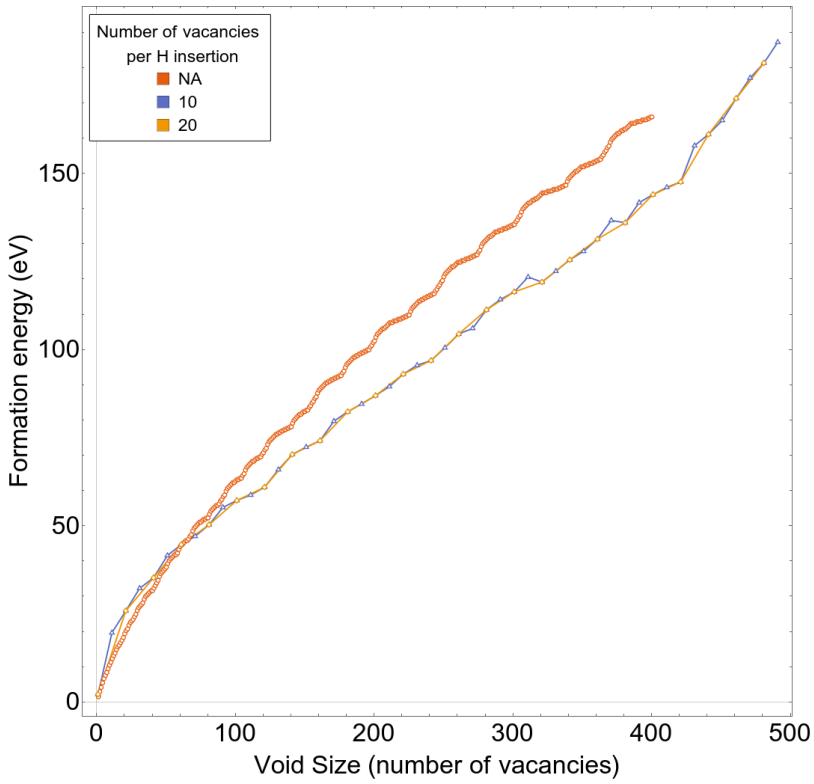

Figure 4.9: Rate dependence of the formation energy. The red curve is calculated from a system containing no H. The blue and orange curves are for a system with 1 H per vacancy added a different rates. In the blue curve 10 H atoms are added after every 10 vacancies are added to the vacancy cluster and in the orange 20 H atoms are added after every 20 vacancies. Both curves represent a H per vacancy ratio of 1.

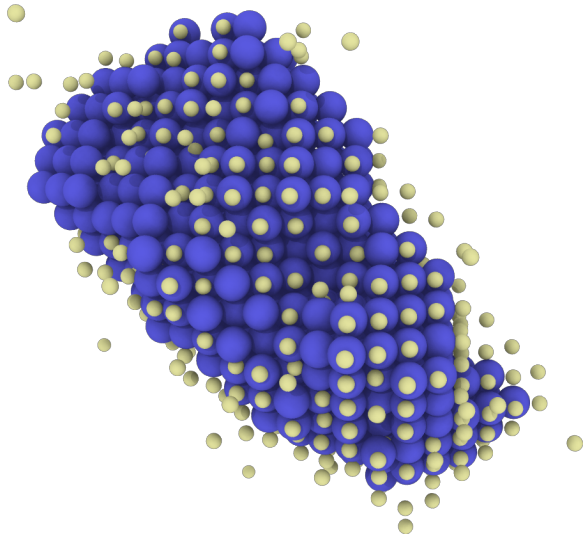

Figure 4.10: Vacancy cluster generated at a slower H addition rate. In this image the blue points are vacant lattice sites and the light yellow are H atoms. This structure is from the case with 20 H added after every 20 vacancies.

The formation energy at this lower H stabilization rate is decreased relative to the case of 0 H. Moreover, the curves are smoother than in the previous set (with H added with every vacancy). In addition, the curves for the two different rates are practically identical. This indicates that while rate has some effect, it appears to saturate. To address this in the continuing simulations, we choose to use the intermediate rate (H additions every 10 vacancies) for the following simulations.

Perhaps more interesting is the structure of the resultant cluster, shown in Figure 4.10; it is dramatically different from those observed in the previous section. Here, the cluster grows into an oblate structure. The surfaces are not as well defined as in the perfect octahedral case with 0 H, but this structure does not deviate as significantly as those in Figure 4.8 (from the 1H 1 vacancy simulations). Although it is not fully faceted, it bears some resemblance to a faceted void. The H field also appears to occupy many of the surface sites, with some of the H occupying the first neighboring octahedral sites, as was predicted in the simulations of smaller clusters. Overall, simulations at a lower rate of H addition generate more qualitatively reasonable clusters and smoother, less wavy formation energy curves. For these reasons, we choose to use a slower rate, adding H for every 10 vacancies.

4.2.3 Formation energy and structure as a function of H

Having explored several scenarios, we next proceed with calculating the formation energy of H-vacancy clusters as a function of number of H per vacancy. We choose to add H after every 10th vacancy and allow the H field to relax around the cluster by MC swapping after each addition. In this set of runs, we vary the number of H per vacancy ranging from 0.1 to 2. Included in this set are values less than 1. It was not previously mentioned, but using a slower rate (not adding H with every vacancy) allows for lower H concentrations at constant rate. This also allows for accommodation of the decrease in number of sites with increasing cluster size, as will be discussed later. These calculations, as before, are run for at least 400 vacancies per cluster. Results are shown in Figure 4.11.

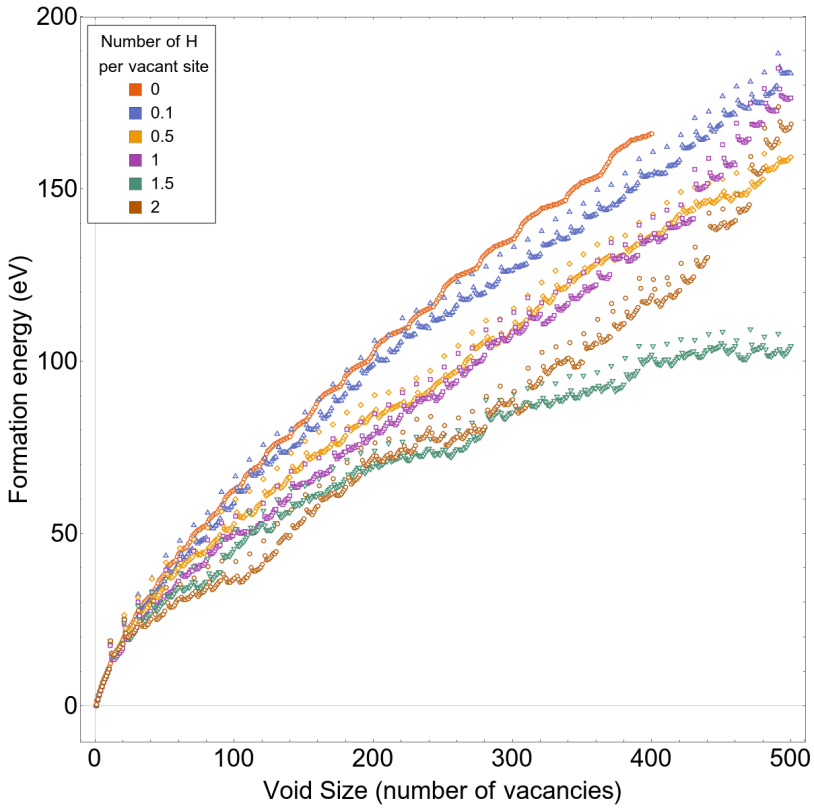

Figure 4.11: Formation energy for a range of ratios of H per vacancy with H being added after every 10 vacancies are added to the vacancy cluster.

In Figure 4.11, the formation energy decreases with increasing H per vacancy. It is noteworthy that at large cluster sizes, the formation energy curves for H per vacancy values

of one and greater appear to curve upward for large clusters. As shown in Figure 4.12 the clusters are more ordered, and more closely resemble the octahedral geometry of the bare vacancy cluster than those of the rapid H stabilization cases. The case of 0.1 H per vacancy is very similar to that of the 0 H octahedron, but slightly elongated, the 0.5 H per vacancy case is more oblate. In the higher H per vacancy cases, the structure is significantly elongated. These serpentine structures are surrounded in many sections by a dense H field, accommodating H in both interior vacancy sites as well as in neighboring octahedral sites. In the most extreme case, with two H per vacancy, the H field seems to form a hydride phase, as was observed in the two H per vacancy case at the higher rate of H addition.

The lower and no H structures are qualitatively distinct from those of the higher H clusters. In contrast, the higher H structures are all fairly similar, aside from the differences in their H fields. It it possible that this is due to a saturation of the H in and around the cluster as it grows. As a vacancy cluster becomes larger, the number of H sites per vacancy decreases. To understand the limiting H per vacancy for the cluster sizes studied here, we enumerate the number of sites as a function of number of vacancies for a perfect octahedral cluster. To do this, we note that the surface of an octahedral void is comprised of 8 equilateral triangular faces and 12 equal edges and 6 verticies. We then add up the number of vacancies on the interior of the faces, along the edges (excluding the verticies), and on each vertex as a function of integer edge length (number of vacancies on an edge) i.e.,

$$N_{surf} = \sum^{faces} N_{face} + \sum^{edges} N_{edge} + 6 = 8N_{face} + 12(l-2) + 6 \tag{4.2}$$

where N_{surf} is the number of surface vacancies in the cluster, N_{face} is the number of vacancies on the interior of a face, and $N_{edge} = (l-2)$ is the number of vacancies along an edge minus the vertex points where l is the integer edge length. The number of vacancies in the interior of a face is given by the $l-3$ triangle number and can be written as a binomial

coefficient, noting that the interior is comprised of a triangle with edge length of $l-3$, i.e.,

$$N_{face} = \binom{(l-3)+1}{2} = \frac{(l-3)((l-3)+1)}{2} \tag{4.3}$$

To understand the decrease in available sites, we note that each surface site contributes one interior vacancy site and seek to calculate the ratio $N_{surf}/N_{cluster}$, where $N_{cluster}$ is the total number of vacancies in the cluster. This number can be calculated for the octahedral cluster by noting that the octahedron is constructed from two stacked pyramids of edge length $l-1$ separated by a plane of edge length l. The number of lattice points in the pyramid is calculated by summing over the planes comprising the pyramid. This yields

$$N_{cluster} = l^2 + 2\sum_{i=1}^{l-1}(l-i)^2 \tag{4.4}$$

From Equations 4.2, 4.3, and 4.4, we now have an expression for the ratio of surface vacancies to total vacancies in a cluster as a function of the size (edge length). This is plotted in Figure 4.13 and provides a quantitative approach to evaluate the decrease in relative number of surface sites as a function of cluster size.

The blue point in Figure 4.13 corresponds to a vacancy cluster of about 500 vacancies. This gives a value for $N_{surf}/N_{cluster}$ of about 0.5, indicating that at a size of about 500 vacancies only around half of the vacancies contribute potential H sites. This is consistent with the formation energy results, indicating that for large sizes the formation energy begins to increase more rapidly. In addition, this supports the qualitative observation from this work that for high H per vacancy values, the H field around a void appears to saturate, leading to the growth of local hydride phases. While this cluster size exceeds the maximum cluster sizes in these simulations, we take this as an upper bound for the H per vacancy values which can be expected to provide reliable results. As such, we continue with calculations highlighting the regime of H per vacancy values less than or equal to 0.5.

In the last set of simulations, we calculate the formation energy for H per vacancy

values ranging from 0 to 1 in increments of 0.1. As in the previous calculations, this is run for the case where H is added after every 10th vacancy. Results are shown in Figure 4.14. The simulations for 0.5 H per vacancy and below show a consistent trend of decreasing cluster formation energy with increasing H. Above this value, the trend breaks down and appears noisy. In addition, the curves 'wiggle' more than in the lower H cases, indicating some external effect (e.g., H clustering outside the vacancy cluster). This is consistent with the above analysis, which indicates that values above about $0.5N_v$ for clusters around 500 vacancies may be over-saturated with H. Overall, this supports the analysis above and provides bounds for these simulations. The data obtained in this section can then be used to further understand the H effect on vacancy clustering. These data are analyzed in this context in the following sections, and connections are made to a nanovoid nucleation model at the mesoscale.

4.3 H effects on Nanovoid nucleation

As a means of quantifying H effects on void growth, we follow an analysis on the free energy of void growth due to radiation damage [87, 129]. Under irradiation conditions, vacancy (and interstitial) concentrations are very high relative to equilibrium concentrations and the driving force for the formation of voids is the vacancy supersaturation, given by

$$S_v = \frac{C_v}{C_v^0} \tag{4.5}$$

where C_v is the vacancy concentration and C_v^0 is the equilibrium vacancy concentration (which is a function of T). We apply this analysis noting that the vacancy production mechanisms which have been discussed in previous sections (collinear annihilation of loops and jog dragging) both result in high local vacancy concentrations, above the equilibrium values. While this approach may not fully represent the bulk behavior of such systems, it is capable of capturing the effect of the locally elevated vacancy concentration.

Accounting for voids, the Gibbs free energy for a system can be written [129]

$$G = G_0 + \sum \rho^0(n) G_n - k_B T \sum \ln \omega_n \tag{4.6}$$

where G_0 is the free energy of a perfect lattice, $\rho^0(n)$ is the distribution of void sizes, ω_n is the number of ways $\rho^0(n)$ voids of size n can be arranged (i.e., possible configurations), and G_n is the reversible work of void formation, given by

$$G_n = E_n + pV_n - TS_n \tag{4.7}$$

The last two terms respectively capture the 'PV' work (p is the hydrostatic pressure and V_n is the volume change due to n vacancies in a void) and the entropy change, S_n, due to the void formation. If, following Olander [129], we neglect the pressure and entropy dependence then $G_n \approx E_n$ is simply the internal energy of the system. It has been shown that for sufficiently large voids the energy is related to the surface energy, γ, [130] and generally we can take

$$E_n = 4\pi R_v^2 \gamma \tag{4.8}$$

where R_v is the void radius. For a spherical void, the radius is related to the number of vacancies through the expression

$$n = \frac{4\pi R_v^3}{3\Omega} \tag{4.9}$$

where Ω is the atomic volume. For a spherical void, γ can be thought of as an averaged value over the possible surface orientations, as opposed to the surface energy for only one specific crystallographic orientation. It should be noted here that the voids generated in the previous simulations are not spherical but instead tend to have an octahedral geometry. In the case of octahedral voids it should be expected that the formation energy should depend

on the surface energy of the faces (in our case $\{111\}$), and some contribution associated with the edges. We retain the spherical approximation in order to make a direct qualitative comparison, bearing in mind this discrepancy. Using this expression yields

$$E_n = (36\pi\Omega^2)^{1/3}\gamma n^{2/3} \tag{4.10}$$

Notably, the formation energy has a 2/3 power dependence on the number of vacancies comprising a void. Equation 4.10 provides a physically based starting point for analysis of the obtained formation energy data, with the limitation that this is an approximation for a spherical void and the observed voids are faceted. As such, there is expected to be some deviation in the calculated surface energies. Calculation of the H-affected surface energy using Equation 4.10 will be discussed in the following section.

This analysis continues with the calculation of the number of configurations of the system, ω_n, containing a distribution of voids $\rho^0(n)$ and N_0 lattice sites per unit volume, so that

$$\omega_n = \frac{n^{(\rho^0)}(N_0/n)}{(N_0/n-\rho^0)!(\rho^0)!} \tag{4.11}$$

To calculate the equilibrium distribution, we require that the system be in equilibrium with respect to the chemical potential

$$\mu_n = \left.\frac{\partial G}{\partial \rho^0}\right|_{T,p,n} \tag{4.12}$$

with the condition that the vacancy field be in chemical equilibrium with the void distribution, i.e.,

$$n\mu_v = \mu_n \tag{4.13}$$

Here, μ_v is the chemical potential of a single vacancy. Invoking Stirling's approximation

and differentiating, we obtain the expression

$$\mu_n = E_n + k_B T \ln\left(\frac{\rho^0}{N_0}\right) \tag{4.14}$$

For a single vacancy, this expression reduces to the form

$$\mu_v = E_v + k_B T \ln\left(\frac{C_v}{N_0}\right) \tag{4.15}$$

In the dilute limit, the equilibrium vacancy concentration is

$$C_v^0 = N_0 \exp\left(-\frac{E_v}{k_B T}\right) \tag{4.16}$$

where E_v is the formation energy of a single vacancy. Combining Equations 4.15 and 4.16 yields

$$\mu_v = k_B T \ln\left(\frac{C_v}{C_v^0}\right) = k_B T \ln(S_v) \tag{4.17}$$

From equations 4.14, 4.17, and 4.13 we obtain the void size distribution

$$\rho^0(n) = N_0 \exp\left(n \ln(S_v) - \frac{1}{k_B T} E_n\right) \tag{4.18}$$

and noting that $\rho^0 = N_0 \exp(-\Delta G_n^0 / k_B T)$ we can then write the change in free energy due to the formation of a spherical void containing n vacancies as

$$\Delta G_n^0 = -n k_B T \ln(S_v) + (36\pi\Omega^2)^{1/3} \gamma n^{2/3} \tag{4.19}$$

This expresses competition between two effects, the vacancy supersaturation driving the growth of the void by lowering the free energy of formation, and the cost of the surface formation energy. Balance between these two effects defines a threshold for the critical void size, after which void growth is favorable with respect to changes in the free energy.

The analysis presented in this section is intended to guide discussion on the H-affected surface energy and its role in void nucleation at the mesoscale. In the following section, discussion is focused on the estimation of γ from simulation data, the role of H on γ, and how H effect enter in equation 4.19.

4.3.1 Power laws for the nanovoid formation energy and the H-affected surface energy

Equation 4.10 provides a physically-based power law expression for the formation energy of spherical voids as a function of number of vacancies comprising the void. Material dependence enters through the atomic volume, Ω, and the surface energy, γ. In addition to this expression, void formation energies have recently been studied using an empirical model which takes the formation energy to be [126]

$$E_f = E_0(1 - An^{2/3}) \tag{4.20}$$

Here, E_0 and A are fitting parameters and we retain the 2/3 power scaling in n. The E_0 parameter may be related to the cohesive energy, but the relationship between A and the surface energy is unclear. While the parameter values do not have direct interpretations in terms of material parameters, this type of fitting provides the benefit that there is no assumption of spherical void geometries.

Perhaps a simpler way of relaxing the assumption that a void is spherical is to include a leading term in the energy that captures the effect of void geometry. Following the analysis above,

$$E_f = f\Omega^{2/3}\gamma n^{2/3} \tag{4.21}$$

where f is a geometric factor. In the simulation data for 0 H, the geometry is purely octahedral, with all surfaces all along $\{111\}$ planes. The value of f can then be determined by fitting Equation 4.21 to the 0 H data, taking $\gamma = \gamma_{\{111\}}$ to be the surface energy of

Table 4.1: Effective surface energies as a function of H atoms per vacancy

H per vacancy	$\gamma_{eff} \times 10^{19}(\mathrm{eV/m^2})$	$\gamma_{eff}(\mathrm{mJ/m^2})$
0	1.274	2042
0.1	1.202	1927
0.2	1.146	1837
0.3	1.099	1761
0.4	1.072	1719
0.5	1.050	1683

a $\{111\}$ plane. There are also edges present in the simulated structure which contribute to the energy; however, for simplicity we neglect this contribution and assume that this is captured in f. The obtained value of f can then be held fixed and used to model the H dependence of γ.

Simulation data are fit to both Equations 4.10 and 4.21. In the case of Equation 4.21, only γ is fit, retaining the leading factors for spherical voids. The data for cases from 0 to 1 H per vacancy in increments of 0.1 are used to perform fits. Recall that for H per vacancy values above about 0.5 the data are expected to be unrealistic, as the vacancy cluster is over-saturated with H atoms. There are more H present than there are sites available in the cluster. These data are retained, however, for the purpose of illustrating the breakdown in the trend with increasing H after this threshold. Curves and data for both fits are shown in Figure 4.15. Figure 4.15(c) plots the fit values for γ as a function of n_H/n, the ratio of the number of H atoms to the number for vacancies. Table 4.1 contains the values of γ in the ranges of 0 to 0.5 H per vacancy obtained by fitting Equation 4.10 in two sets of units (for ease of interpretation).

A consistent decrease in the surface energy with increasing H is evident from the simulation data. The surface energy as a function of the ratio n_H/n shows a uniform decrease until about 0.6, consistent with the argument for the number of available sites as a function of cluster size. For the data fit directly to Equation 4.10 the 0 H formation energy is 2042 mJ/m^2. Compared to the value of $\gamma_{\{111\}}$ for the interatomic potential [62] (1929 mJ/m^2),

this is high. The relative increase is likely due to the presence of edges in the octahedral geometry which are not considered explicitly in this fit. Fitting by Equation 4.10 or Equation 4.21 results in curves that are simply shifted relative to one another (Figure 4.15(c)). Since they are similar, we choose to use the simpler result provided by the Equation 4.10. As such, the γ values reported in Table 4.1 are for the fits obtained by Equation 4.10.

With these data in hand, we finish by investigating the role of H on the free energy change due to void nucleation. These curves are calculated by inserting γ values from Table 4.1 into Equation 4.10. Values of ΔG_n^0 are then plotted as a function of n and the maximum of these curves represents the critical void size. Data are shown in Figure 4.16. At the critical size, if the void either increases or decreases in size the free energy change decreases (the change is energetically favorable). If the void grows beyond the critical void size it then becomes favorable for the void to continue growing, and thus a void has been successfully nucleated. In Figure 4.16, as the number of H per vacancy increases, the maximum in the curves shifts to the left. This decrease in critical void size with increasing H indicates that H plays the role of decreasing the critical void size for nucleation, thereby promoting the formation of voids.

At high H concentrations the critical void size drops to about 2.5. With critical sizes this low void growth is effectively energetically favorable. If more than 2 vacancies coalesce to form a cluster it is then more favorable (has a lower energy cost) to add a vacancy to the cluster than to remove one. An implication of this at the macroscale is that, when H is present, void nucleation is spontaneous and therefore the evolution of the size and density of nanovoids is only driven by the growth kinetics.

To summarize, the effect of H on the surface energy is calculated by fitting the obtained simulation data to Equations 4.10. The γ values obtained from these fits indicate that H decreases the surface energy. This effect exhibits a consistent trend up to about 0.5 H per vacancy, consistent with the notion that larger clusters have fewer sites available for H to occupy. Decreasing surface energy has the additional effect of lower the critical void size

for nucleation. Thus we conclude that H acts to stabilize the formation of voids through a decrease in the critical size which results from a decrease in the H-affected surface energy. Under the simulation conditions the critical size for nucleation decreases from about five vacancies to three vacancies.

4.3.2 Nanovoid nucleation in continuum dislocation dynamics

Continuum Dislocation Dynamics (CDD) is a coarse grained dislocation dynamics method that relies on a statistical interpretation of the evolution equations for the dislocation density [131, 132, 133, 134]. In contrast to Discrete Dislocation Dynamics (DDD) [135, 136, 137], which treats dislocations as discrete lines, CDD casts the local dislocation density evolution as a field equation to be integrated over a mesh. This facilitates faster computations at high dislocation densities relative to DDD, for which computation time increases with increasing dislocation density. Within the EICEM program, CDD, has been used to study the evolution of dislocation structure with plastic strain and several additional modules have been built in, including one which tracks the production of vacancies by jog dragging [49].

Following the above framework, a nanovoid nucleation model, informed by the calculations presented here, can also be introduced in this CDD framework. Given the density of voids of size n

$$\rho_0(n) = N_0 \exp\left(-\frac{\Delta G_n^0}{k_B T}\right) \tag{4.22}$$

with ΔG_n^0 given by Equation 4.19, we can determine if a void will form. This is done by sampling the void size from the void size distribution, given a local value of C_v (or equivalently S_v). This is then compared to the critical void size, determined as in Figure 4.16. If n is greater than the critical void size, then we accept the nucleation and a small void is formed. This is done in each element taking into account the local vacancy concentration and the number of H per vacancy, which determines the value of γ. In this framework, the H effect is introduced through its role in reducing the surface energy leading to a reduction

in the critical void size for nucleation. This model, integrated with the H-affected surface energy, represents a novel approach to the introduction of H effects on nanovoid nucleation at the mesoscale.

This formulation can also guide continuum modeling efforts and further development of the CP-UMAT. At this higher length scale the model is relatively coarse and requires consideration of the distribution (and densities) of a collection of voids over a larger region. Along with this difference, the vacancy concentration model implemented in the CP-UMAT accounts for production of vacancies through the colinear annihilation of edge segments in channels along with the non-conservative jog dragging of screw segments. Qualitatively, the nucleation rate of voids when H is present is expected to be high because H lowers the critical void size, as shown in Figure 4.16. As such the density of nanovoids is expected to be directly related to the vacancy concentration. In regions where a high density of vacancies exist, nanovoids will nucleate in proportion to the local vacancy concentration and grow by trapping nearby vacancies. Additionally, while the CP-UMAT accounts for dislocation annihilation in vacancy production (and CDD only considers jog dragging) the two may produce similar results, since in both cases localization of high vacancy concentrations is critical in the void nucleation process.

In regions of high vacancy and H concentrations, high H-vacancy cluster densities will follow. These clusters can then grow to form large nanovoids, due to the decreased critical size for nucleation, and subsequently act as strong obstacles to the glide of dislocations. After a sufficiently high stress is reached, such that the collection of dislocations can free themselves from these obstacles, the dislocations resume motion. CDD can be used to inform these types of modeling in the CP-UMAT. With the integration of nanovoid nucleation, CDD can be used to estimate the distribution of void sizes as a function of H concentration and dislocation density. This, along with the assertion that nanovoids will nucleate in proportion to the vacancy concentration, provides an estimate of obstacle distribution and strength (size) at the continuum scale. In this way modeling starting at atomistic length

scales can be passed into the mesoscale for use in CDD, which can inform the bulk kinetics of dislocation-obstacle interaction at the macro scale to aid in development of additional modules for the CP-UMAT.

4.4 Overall summary

This chapter began by outlining two methods for computing the formation energy of small vacancy clusters with H. In one method, a MS-based approach is used which is fast but has significant constraints that may limit the validity of the simulation results. In the other, a full MC technique is used to compute the cluster formation energy, allowing for fewer constraints but at a much higher computational cost. It is observed in these simulations that H plays the role of decreasing the formation energy up to a threshold value of about 4 H per vacancy. Beyond this level, the formation energy appears to saturate. Following these approaches, we then discuss a hybrid MS/MC approach that balances the constraints of MS with some of the flexibility of a full MC to allow for faster computation times and larger cluster sizes. In this method, the system is driven toward an energy minimum by removal of the highest energy atom to grow the vacancy cluster. The H field is then allowed to relax around the cluster with a full MC calculation over the sublattice of H sites. Clusters tend towards octahedral geometries in these simulations, with surfaces along [111] planes.

Using relations between the cluster formation energy and the surface energy, a H-affected surface energy is calculated, showing the H decreases the surface energy. This decrease in surface energy results in a corresponding decrease in the critical void size for void nucleation, implying that H promotes void nucleation. At high H concentrations the critical void size is sufficiently small for nucleation to occur spontaneously. This implies that at the macroscale it can be assumed that voids will nucleate and only the growth process need be considered. In addition, an application of this data to a mesoscale void nucleation model was discussed. In the mesoscale simulations a void may be nucleated on any integration point. The distribution of void sizes (which depends on ΔG_n^0) is sampled at each

point to generate a distribution of void nuclei.

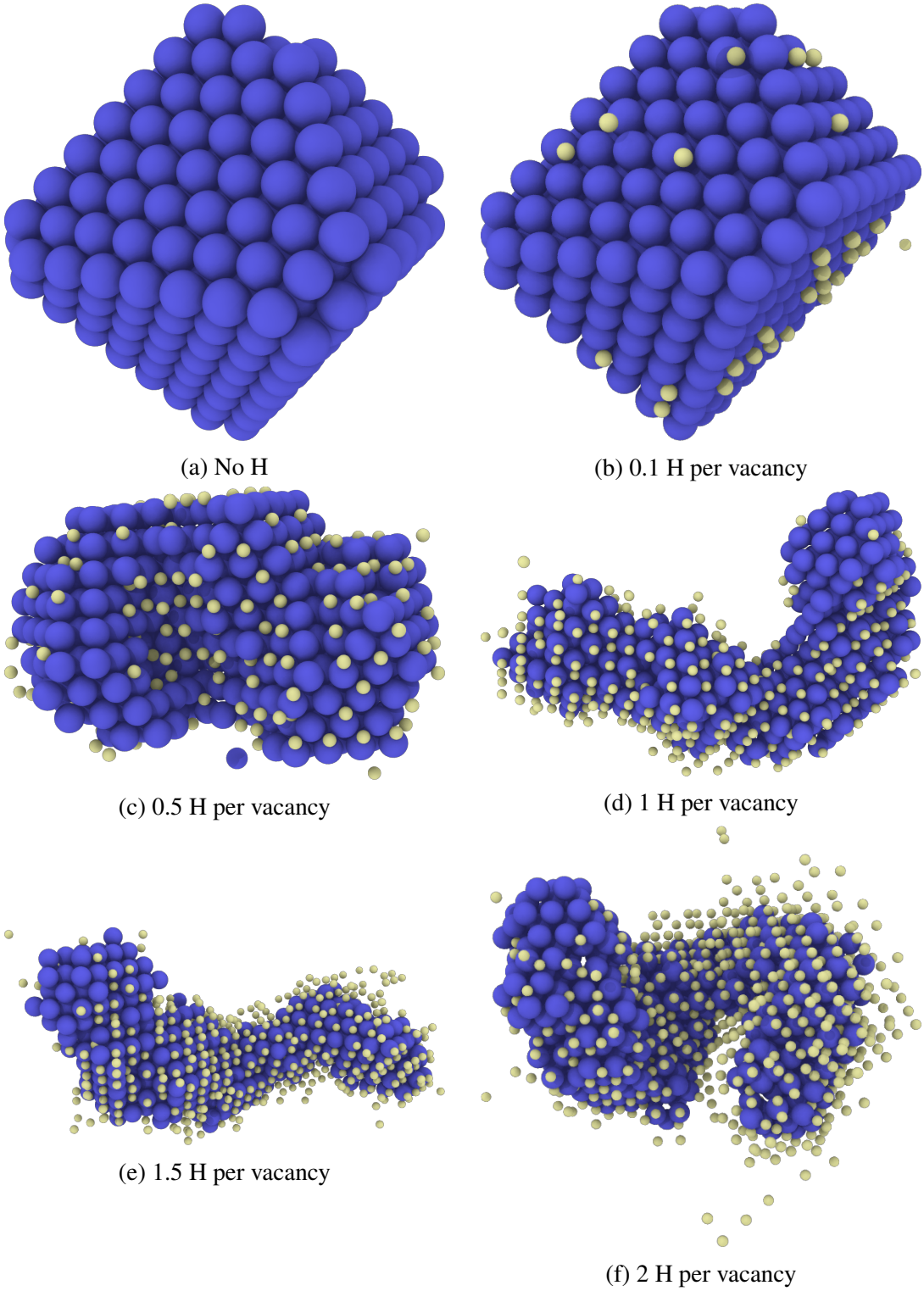

(a) No H

(b) 0.1 H per vacancy

(c) 0.5 H per vacancy

(d) 1 H per vacancy

(e) 1.5 H per vacancy

(f) 2 H per vacancy

Figure 4.12: Structures corresponding to the formation energy curves in Figure 4.11 illustrating the qualitative trend with increasing H concentration. All voids contain the same number of vacancies. Blue spheres are vacant lattice sites and H atoms are indicated by the light yellow spheres.

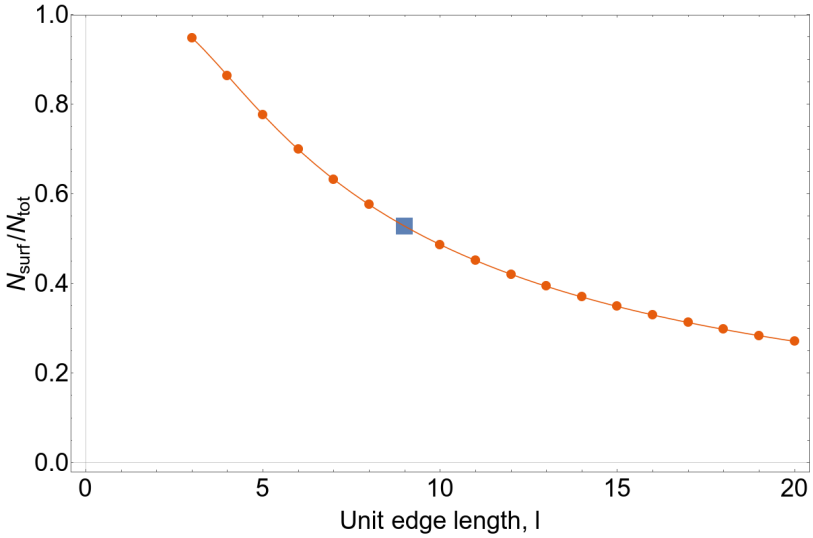

Figure 4.13: The ratio of surface vacancies to total vacancies in an octahedral cluster as a function of edge length. The blue rectangle corresponds to a cluster size of about 500 vacancies and is used as an upper bound for cluster sizes observed in these simulations.

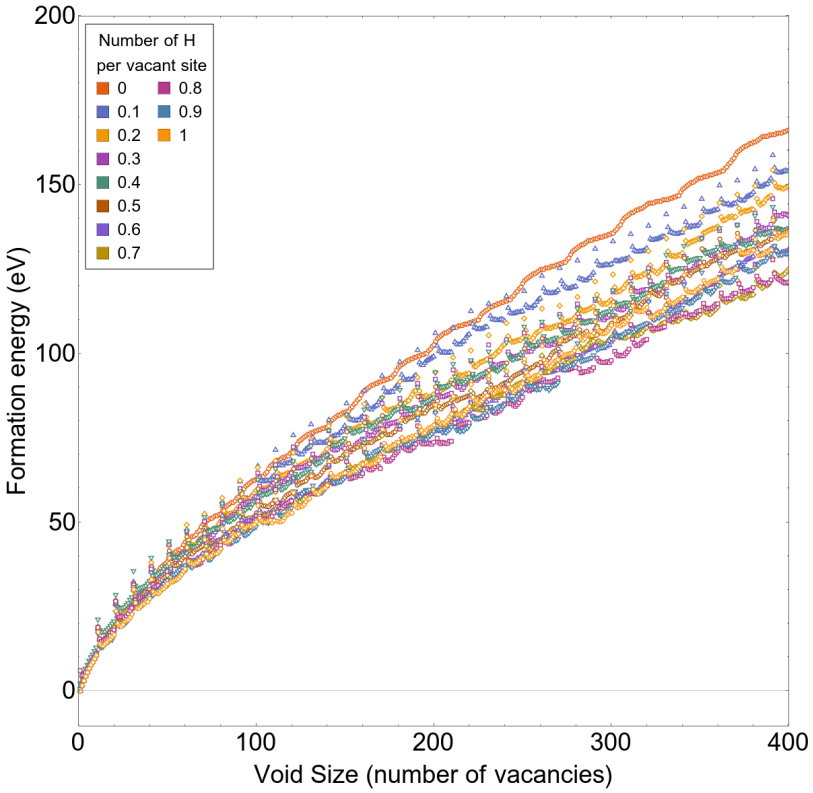

Figure 4.14: Formation energies as a function of void size for H per vacancy ratios of 1 or less.

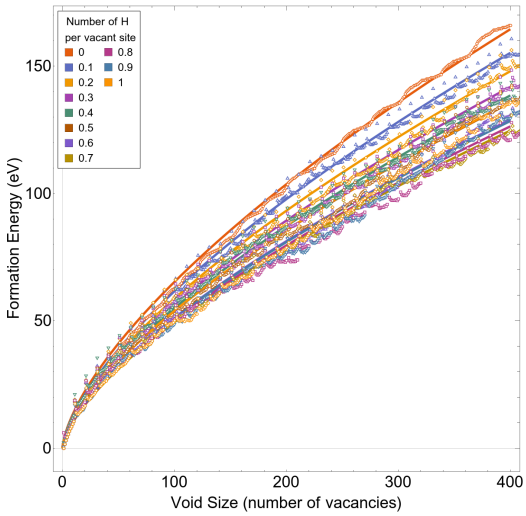

(a) Fits from equation 4.10

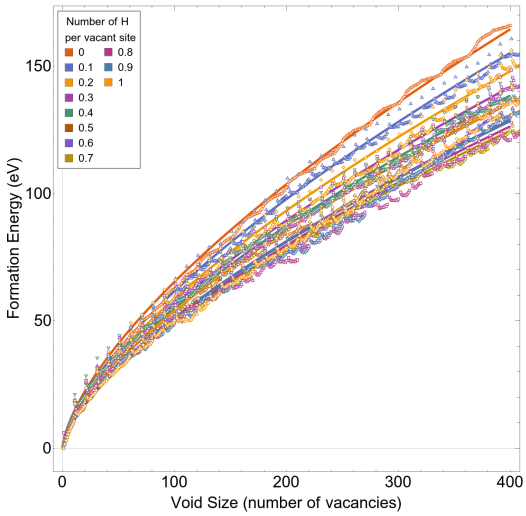

(b) Fits from equation 4.21

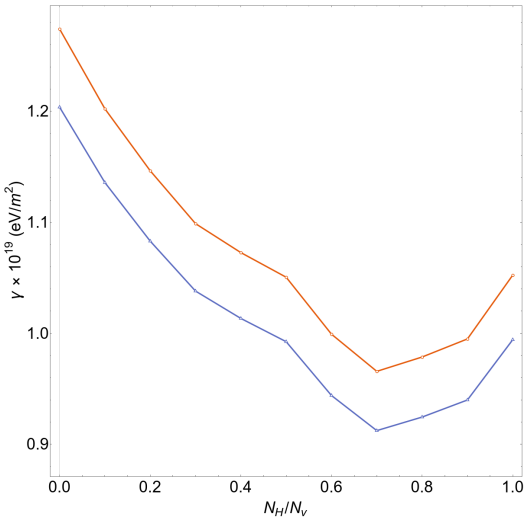

(c) γ values for each set of fits

Figure 4.15: Plots qualitatively illustrating the fits from (a) equations 4.10 and (b) equation 4.21. The values of γ obtained from each set of fits are shown in (c). The red curve corresponds to equation 4.10 and the blue curve to equation 4.21.

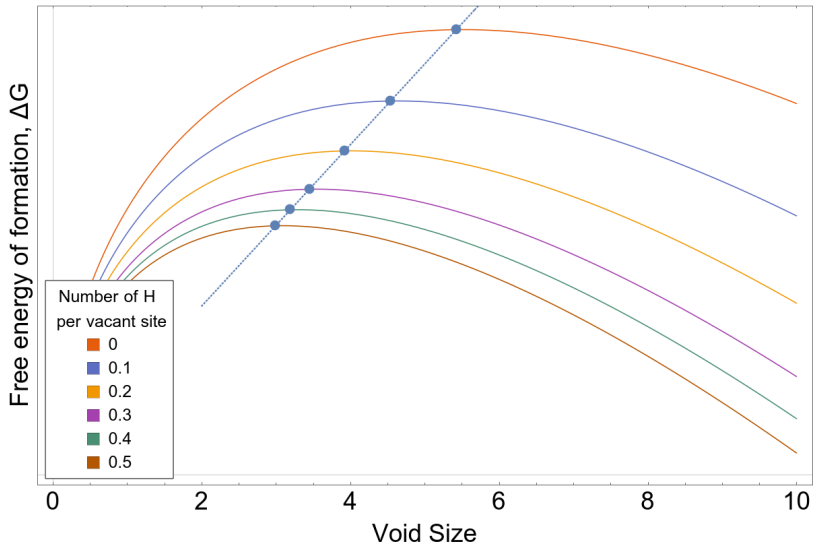

Figure 4.16: The free energy change due to void formation. Blue points indicate the maximum in ΔG, which corresponds to the critical void size.

REFERENCES

[1] W. H. Johnson, *On some remarkable changes produced in iron and steel by the action of hydrogen and acids*, 1875.

[2] C. Beachem, *Hydrogen Damage: Ed : C.D. Beachem*, ser. A metals science source book. 1977.

[3] I. M. Robertson, P. Sofronis, A Nagao, M. Martin, S Wang, D. Gross, and K. Nygren, "Hydrogen embrittlement understood," *Metallurgical and Materials Transactions B*, vol. 46, no. 3, pp. 1085–1103, 2015.

[4] S. Lynch, "Hydrogen embrittlement phenomena and mechanisms," *Corrosion Reviews*, vol. 30, no. 3-4, pp. 105–123, 2012.

[5] H. K. Birnbaum and P. Sofronis, "Hydrogen-enhanced localized plasticity—a mechanism for hydrogen-related fracture," *Materials Science and Engineering: A*, vol. 176, no. 1-2, pp. 191–202, 1994.

[6] D. Shih, I. Robertson, and H. Birnbaum, "Hydrogen embrittlement of α titanium: In situ tem studies," *Acta Metallurgica*, vol. 36, no. 1, pp. 111–124, 1988.

[7] P. Ferreira, I. Robertson, and H. Birnbaum, "Hydrogen effects on the interaction between dislocations," *Acta materialia*, vol. 46, no. 5, pp. 1749–1757, 1998.

[8] P. Ferreira, I. M. Robertson, and H. Birnbaum, "Influence of hydrogen on the stacking fault energy of an austenitic stainless steel," in *Materials Science Forum*, Aedermannsdorf, Switzerland: Trans Tech Publications, 1984-, vol. 207, 1996, pp. 93–96.

[9] R. Oriani, "A mechanistic theory of hydrogen embrittlement of steels," *Berichte der Bunsengesellschaft für physikalische Chemie*, vol. 76, no. 8, pp. 848–857, 1972.

[10] T. Lee, I. Robertson, and H. Birnbaum, "An hvem in situ deformation study of nickel doped with sulfur," *Acta Metallurgica*, vol. 37, no. 2, pp. 407–415, 1989.

[11] D. Xie, S. Li, M. Li, Z. Wang, P. Gumbsch, J. Sun, E. Ma, J. Li, and Z. Shan, "Hydrogenated vacancies lock dislocations in aluminium," *Nature Communications*, vol. 7, 2016.

[12] T. Ungár, E. Schafler, P. Hanák, S. Bernstorff, and M. Zehetbauer, "Vacancy production during plastic deformation in copper determined by in situ x-ray diffraction," *Materials Science and Engineering: A*, vol. 462, no. 1-2, pp. 398–401, 2007.

[13] E Schafler, G Steiner, E Korznikova, M Kerber, and M. Zehetbauer, "Lattice defect investigation of ecap-cu by means of x-ray line profile analysis, calorimetry and electrical resistometry," *Materials Science and Engineering: A*, vol. 410, pp. 169–173, 2005.

[14] M Nagumo, K Ohta, and H Saitoh, "Deformation induced defects in iron revealed by thermal desorption spectroscopy of tritium," *Scripta materialia*, vol. 40, no. 3, 1999.

[15] M. Nagumo and K. Takai, "The predominant role of strain-induced vacancies in hydrogen embrittlement of steels: Overview," *Acta Materialia*, vol. 165, pp. 722–733, 2019.

[16] M Nagumo, "Hydrogen related failure of steels–a new aspect," *Materials Science and Technology*, vol. 20, no. 8, pp. 940–950, 2004.

[17] M Nagumo, M Nakamura, and K Takai, "Hydrogen thermal desorption relevant to delayed-fracture susceptibility of high-strength steels," *Metallurgical and Materials Transactions A*, vol. 32, no. 2, pp. 339–347, 2001.

[18] Y. Fukai, Y. Ishii, Y. Goto, and K. Watanabe, "Formation of superabundant vacancies in pd–h alloys," *Journal of alloys and compounds*, vol. 313, no. 1, pp. 121–132, 2000.

[19] Y Fukai, Y. Shizuku, and Y Kurokawa, "Superabundant vacancy formation in ni–h alloys," *Journal of alloys and compounds*, vol. 329, no. 1, pp. 195–201, 2001.

[20] Y. Fukai, "Formation of superabundant vacancies in m–h alloys and some of its consequences: A review," *Journal of Alloys and Compounds*, vol. 356, pp. 263–269, 2003.

[21] W. Kohn and L. J. Sham, "Self-Consistent Equations Including Exchange and Correlation Effects," *Physical Review*, vol. 140, no. 4A, pp. 1133–1138, Nov. 1965.

[22] P. Hohenberg and W. Kohn, "Inhomogeneous Electron Gas," *Physical Review*, vol. 136, no. 3B, pp. 864–871, Nov. 1964.

[23] D. Frenkel and B. Smit, *Understanding molecular simulation: from algorithms to applications*. Elsevier, 2001, vol. 1.

[24] J Song and W. Curtin, "Mechanisms of hydrogen-enhanced localized plasticity: An atomistic study using α-fe as a model system," *Acta Materialia*, vol. 68, pp. 61–69, 2014.

[25] W. Barrows, R. Dingreville, and D. Spearot, "Traction–separation relationships for hydrogen induced grain boundary embrittlement in nickel via molecular dynamics simulations," *Materials Science and Engineering: A*, vol. 650, pp. 354–364, 2016.

[26] A Tehranchi, X Zhou, and W. Curtin, "A decohesion pathway for hydrogen embrittlement in nickel: Mechanism and quantitative prediction," *Acta Materialia*, vol. 185, pp. 98–109, 2020.

[27] W Cai, R. Sills, D. Barnett, and W. Nix, "Modeling a distribution of point defects as misfitting inclusions in stressed solids," *Journal of the Mechanics and Physics of Solids*, vol. 66, pp. 154–171, 2014.

[28] Y Mishin and J. Cahn, "Thermodynamics of cottrell atmospheres tested by atomistic simulations," *Acta Materialia*, vol. 117, pp. 197–206, 2016.

[29] J. Polák and M. Sauzay, "Growth of extrusions in localized cyclic plastic straining," *Materials Science and Engineering: A*, vol. 500, no. 1, pp. 122–129, 2009.

[30] P Nordlander, J. No, F. Besenbacher, S. Myers, *et al.*, "Multiple deuterium occupancy of vacancies in pd and related metals," *Physical Review B*, vol. 40, no. 3, p. 1990, 1989.

[31] N. K. Das, T. Shoji, T. Nishizumi, T. Fukuoka, T. Sugawara, R. Sasaki, T. Tatsuki, H. Yuya, K. Ito, K. Sakima, *et al.*, "First-principles calculations of hydrogen interactions with nickel containing a monovacancy and divacancies," *Materials Research Express*, vol. 4, no. 7, p. 076 505, 2017.

[32] R. Nazarov, T. Hickel, and J. Neugebauer, "Ab initio study of h-vacancy interactions in fcc metals: Implications for the formation of superabundant vacancies," *Physical Review B*, vol. 89, no. 14, p. 144 108, 2014.

[33] Y. Tateyama and T. Ohno, "Stability and clusterization of hydrogen-vacancy complexes in α- fe: An ab initio study," *Physical Review B*, vol. 67, no. 17, p. 174 105, 2003.

[34] G. M. Castelluccio and D. L. McDowell, "Mesoscale cyclic crystal plasticity with dislocation substructures," *International Journal of Plasticity*, vol. 98, pp. 1–26, 2017.

[35] P. Sofronis and H. K. Birnbaum, "Mechanics of the hydrogen-dislocation-impurity interactions—i. increasing shear modulus," *Journal of the Mechanics and Physics of Solids*, vol. 43, no. 1, pp. 49–90, 1995.

[36] R. Oriani and P. Josephic, "Equilibrium aspects of hydrogen-induced cracking of steels," *Acta Metallurgica*, vol. 22, no. 9, pp. 1065–1074, 1974.

[37] R. Dingreville and S. Berbenni, "On the interaction of solutes with grain boundaries," *Acta Materialia*, vol. 104, pp. 237–249, 2016.

[38] J. W. Cahn, Y. Mishin, and A. Suzuki, "Coupling grain boundary motion to shear deformation," *Acta materialia*, vol. 54, no. 19, pp. 4953–4975, 2006.

[39] D. L. Olmsted, S. M. Foiles, and E. A. Holm, "Survey of computed grain boundary properties in face-centered cubic metals: I. grain boundary energy," *Acta Materialia*, vol. 57, no. 13, pp. 3694–3703, 2009.

[40] D. L. Olmsted, E. A. Holm, and S. M. Foiles, "Survey of computed grain boundary properties in face-centered cubic metals—ii: Grain boundary mobility," *Acta materialia*, vol. 57, no. 13, pp. 3704–3713, 2009.

[41] E. R. Homer, S. M. Foiles, E. A. Holm, and D. L. Olmsted, "Phenomenology of shear-coupled grain boundary motion in symmetric tilt and general grain boundaries," *Acta Materialia*, vol. 61, no. 4, pp. 1048–1060, 2013.

[42] E. R. Homer, E. A. Holm, S. M. Foiles, and D. L. Olmsted, "Trends in grain boundary mobility: Survey of motion mechanisms," *Jom*, vol. 66, no. 1, pp. 114–120, 2014.

[43] M. Tschopp and D. McDowell, "Structures and energies of Σ 3 asymmetric tilt grain boundaries in copper and aluminium," *Philosophical Magazine*, vol. 87, no. 22, pp. 3147–3173, 2007.

[44] B. Kuhr, D. Farkas, and I. M. Robertson, "Atomistic studies of hydrogen effects on grain boundary structure and deformation response in fcc ni," *Computational Materials Science*, vol. 122, pp. 92–101, 2016.

[45] J. D. Eshelby, "The determination of the elastic field of an ellipsoidal inclusion, and related problems," in *Proceedings of the Royal Society of London A: Mathematical, Physical and Engineering Sciences*, The Royal Society, vol. 241, 1957, pp. 376–396.

[46] F Larché and J. W. Cahn, "A linear theory of thermochemical equilibrium of solids under stress," *Acta Metallurgica*, vol. 21, no. 8, pp. 1051–1063, 1973.

[47] F. Larché and J. W. Cahn, "A nonlinear theory of thermochemical equilibrium of solids under stress," *Acta Metallurgica*, vol. 26, no. 1, pp. 53–60, 1978.

[48] A Tehranchi, X Zhang, G Lu, and W. Curtin, "Hydrogen–vacancy–dislocation interactions in α-fe," *Modelling and Simulation in Materials Science and Engineering*, vol. 25, no. 2, p. 025 001, 2016.

[49] J. P. Hirth and J. Lothe, "Theory of dislocations," 1982.

[50] R. Sills and W Cai, "Solute drag on perfect and extended dislocations," *Philosophical Magazine*, vol. 96, no. 10, pp. 895–921, 2016.

[51] H Peisl, "Lattice strains due to hydrogen in metals," in *Hydrogen in metals I*, Springer, 1978, pp. 53–74.

[52] J. Straalsund and J. Bates, "Partial molar volumes and size factor data for alloy constituents of stainless steel," *Metallurgical Transactions*, vol. 5, no. 2, pp. 493–498, 1974.

[53] D. Ulmer and C. Altstetter, "Phase relations in the hydrogen-austenite system," *Acta metallurgica et materialia*, vol. 41, no. 7, pp. 2235–2241, 1993.

[54] Y Mishin, "Calculation of open and closed system elastic coefficients for multicomponent solids," *Physical Review B*, vol. 91, no. 22, p. 224 107, 2015.

[55] J. Cahn, "Thermodynamic aspects of cottrell atmospheres," *Philosophical magazine*, vol. 93, no. 28-30, pp. 3741–3746, 2013.

[56] D. Beshers, "On the distribution of impurity atoms in the stress field of a dislocation," *Acta Metallurgica*, vol. 6, no. 8, pp. 521–523, 1958.

[57] C. White and W. Coghlan, "The spectrum of binding energies approach to grain boundary segregation," *Metallurgical and Materials Transactions A*, vol. 8, no. 9, pp. 1403–1412, 1977.

[58] M. S. Daw and M. I. Baskes, "Embedded-atom method: Derivation and application to impurities, surfaces, and other defects in metals," *Physical Review B*, vol. 29, no. 12, p. 6443, 1984.

[59] J. Von Pezold, L. Lymperakis, and J. Neugebeauer, "Hydrogen-enhanced local plasticity at dilute bulk h concentrations: The role of h–h interactions and the formation of local hydrides," *Acta Materialia*, vol. 59, no. 8, pp. 2969–2980, 2011.

[60] F. Reif, *Fundamentals of statistical and thermal physics*. Mcgraw-Hill Kogakusha, 1965.

[61] P. Hirel, "Atomsk: A tool for manipulating and converting atomic data files," *Computer Physics Communications*, vol. 197, pp. 212–219, 2015.

[62] J. E. Angelo, N. R. Moody, and M. I. Baskes, "Trapping of hydrogen to lattice defects in nickel," *Modelling and Simulation in Materials Science and Engineering*, vol. 3, no. 3, p. 289, 1995.

[63] X. Zhou, J. A. Zimmerman, B. M. Wong, and J. J. Hoyt, "An embedded-atom method interatomic potential for pd–h alloys," *Journal of Materials Research*, vol. 23, no. 3, pp. 704–718, 2008.

[64] S. Plimpton, "Fast parallel algorithms for short-range molecular dynamics," *Journal of computational physics*, vol. 117, no. 1, pp. 1–19, 1995.

[65] A. Stukowski, "Visualization and analysis of atomistic simulation data with ovito–the open visualization tool," *Modelling and Simulation in Materials Science and Engineering*, vol. 18, no. 1, p. 015 012, 2009.

[66] P Sofronis and I. Robertson, "Transmission electron microscopy observations and micromechanical/continuum models for the effect of hydrogen on the mechanical behaviour of metals," *Philosophical Magazine A*, vol. 82, no. 17-18, pp. 3405–3413, 2002.

[67] A. Stukowski and K. Albe, "Extracting dislocations and non-dislocation crystal defects from atomistic simulation data," *Modelling and Simulation in Materials Science and Engineering*, vol. 18, no. 8, p. 085 001, 2010.

[68] Y. Tang and J. A. El-Awady, "Atomistic simulations of the interactions of hydrogen with dislocations in fcc metals," *Physical Review B*, vol. 86, no. 17, p. 174 102, 2012.

[69] G. Leyson, B. Grabowski, and J. Neugebauer, "Multiscale description of dislocation induced nano-hydrides," *Acta Materialia*, vol. 89, pp. 50–59, 2015.

[70] M Wen, A Barnoush, and K Yokogawa, "Calculation of all cubic single-crystal elastic constants from single atomistic simulation: Hydrogen effect and elastic constants of nickel," *Computer Physics Communications*, vol. 182, no. 8, pp. 1621–1625, 2011.

[71] A. C. Eringen, *Nonlocal continuum field theories*. Springer Science & Business Media, 2002.

[72] M. Lazar, "A non-singular continuum theory of point defects using gradient elasticity of bi-helmholtz type," *Philosophical Magazine*, pp. 1–39, 2019.

[73] K Takai, H Shoda, H Suzuki, and M Nagumo, "Lattice defects dominating hydrogen-related failure of metals," *Acta Materialia*, vol. 56, no. 18, pp. 5158–5167, 2008.

[74] I Kovács, "The mechanism of the work-hardening in fcc metals," *Acta Metallurgica*, vol. 15, no. 11, pp. 1731–1736, 1967.

[75] T. Ungár, "Subgrain size-distributions, dislocation structures, stacking-and twin faults and vacancy concentrations in spd materials determined by x-ray line profile analysis," in *Materials Science Forum*, Trans Tech Publ, vol. 503, 2006, pp. 133–140.

[76] J. Polák and J. Man, "Fatigue crack initiation–the role of point defects," *International Journal of Fatigue*, vol. 65, pp. 18–27, 2014.

[77] U Essmann and H Mughrabi, "Annihilation of dislocations during tensile and cyclic deformation and limits of dislocation densities," *Philosophical Magazine A*, vol. 40, no. 6, pp. 731–756, 1979.

[78] U Essmann, U Gösele, and H Mughrabi, "A model of extrusions and intrusions in fatigued metals i. point-defect production and the growth of extrusions," *Philosophical Magazine A*, vol. 44, no. 2, pp. 405–426, 1981.

[79] K Differt and U Essmann, "Dynamical model of the wall structure in persistent slip bands of fatigued metals i. dynamical model of edge dislocation walls," *Materials Science and Engineering: A*, vol. 164, no. 1-2, pp. 295–299, 1993.

[80] S. Brinckmann, R. Sivanesapillai, and A. Hartmaier, "On the formation of vacancies by edge dislocation dipole annihilation in fatigued copper," *International journal of fatigue*, vol. 33, no. 10, pp. 1369–1375, 2011.

[81] A. Cuitino and M Ortiz, "Ductile fracture by vacancy condensation in fcc single crystals," *Acta materialia*, vol. 44, no. 2, pp. 427–436, 1996.

[82] F. Frank and W. Read Jr, "Multiplication processes for slow moving dislocations," *Physical Review*, vol. 79, no. 4, p. 722, 1950.

[83] S. Xu, L. Xiong, Y. Chen, and D. L. McDowell, "An analysis of key characteristics of the frank-read source process in fcc metals," *Journal of the Mechanics and Physics of Solids*, vol. 96, pp. 460–476, 2016.

[84] K. M. Davoudi and J. J. Vlassak, "Dislocation evolution during plastic deformation: Equations vs. discrete dislocation dynamics study," *Journal of Applied Physics*, vol. 123, no. 8, p. 085 302, 2018.

[85] E Orowan, "Symposium on internal stresses in metals and alloys," *Institute of Metals, London*, vol. 451, 1948.

[86] J Polák and J Man, "Mechanisms of extrusion and intrusion formation in fatigued crystalline materials," *Materials Science and Engineering: A*, vol. 596, pp. 15–24, 2014.

[87] G. Was, *Fundamentals of Radiation Materials Science: Metals and Alloys*, ser. Springer ebook collection / Chemistry and Materials Science 2005-2008. Springer Berlin Heidelberg, 2007, ISBN: 9783540494713.

[88] S. Li, Y. Li, Y.-C. Lo, T. Neeraj, R. Srinivasan, X. Ding, J. Sun, L. Qi, P. Gumbsch, and J. Li, "The interaction of dislocations and hydrogen-vacancy complexes and its importance for deformation-induced proto nano-voids formation in α-fe," *International Journal of Plasticity*, vol. 74, pp. 175–191, 2015.

[89] E. Hart, "On the role of dislocations in bulk diffusion," *Acta Metallurgica*, vol. 5, no. 10, p. 597, 1957.

[90] K. Nakashima, R. E. Stoller, and H. Xu, "Recombination radius of a frenkel pair and capture radius of a self-interstitial atom by vacancy clusters in bcc fe," *Journal of Physics: Condensed Matter*, vol. 27, no. 33, p. 335 401, 2015.

[91] S. T. Chill, M. Welborn, R. Terrell, L. Zhang, J.-C. Berthet, A. Pedersen, H. Jonsson, and G. Henkelman, "Eon: Software for long time simulations of atomic scale systems," *Modelling and Simulation in Materials Science and Engineering*, vol. 22, no. 5, p. 055 002, 2014.

[92] G. Henkelman and H. Jónsson, "Long time scale kinetic monte carlo simulations without lattice approximation and predefined event table," *The Journal of Chemical Physics*, vol. 115, no. 21, pp. 9657–9666, 2001.

[93] L. Xu and G. Henkelman, "Adaptive kinetic monte carlo for first-principles accelerated dynamics," *The Journal of chemical physics*, vol. 129, no. 11, p. 114 104, 2008.

[94] G. Henkelman and H. Jónsson, "A dimer method for finding saddle points on high dimensional potential surfaces using only first derivatives," *The Journal of chemical physics*, vol. 111, no. 15, pp. 7010–7022, 1999.

[95] A. Heyden, A. T. Bell, and F. J. Keil, "Efficient methods for finding transition states in chemical reactions: Comparison of improved dimer method and partitioned rational function optimization method," *The Journal of chemical physics*, vol. 123, no. 22, p. 224 101, 2005.

[96] J. Kästner and P. Sherwood, "Superlinearly converging dimer method for transition state search," *The Journal of chemical physics*, vol. 128, no. 1, p. 014 106, 2008.

[97] H. Eyring, "The activated complex in chemical reactions," *The Journal of Chemical Physics*, vol. 3, no. 2, pp. 107–115, 1935.

[98] C. Z. Hargather, S.-L. Shang, Z.-K. Liu, and Y Du, "A first-principles study of self-diffusion coefficients of fcc ni," *Computational materials science*, vol. 86, pp. 17–23, 2014.

[99] A. R. Wazzan, "Lattice and grain boundary self-diffusion in nickel," *Journal of Applied Physics*, vol. 36, no. 11, pp. 3596–3599, 1965.

[100] K Maier, H Mehrer, E Lessmann, and W Schüle, "Self-diffusion in nickel at low temperatures," *Physica status solidi (b)*, vol. 78, no. 2, pp. 689–698, 1976.

[101] G. Love, "Dislocation pipe diffusion," *Acta Metallurgica*, vol. 12, no. 6, pp. 731–737, 1964.

[102] T. E. Volin, K. Lie, and R. Balluffi, "Measurement of rapid mass transport along individual dislocations in aluminum," *Acta metallurgica*, vol. 19, no. 4, pp. 263–274, 1971.

[103] M. Legros, G. Dehm, E. Arzt, and T. J. Balk, "Observation of giant diffusivity along dislocation cores," *Science*, vol. 319, no. 5870, pp. 1646–1649, 2008.

[104] M Wuttig and H. Birnbaum, "Self-diffusion along edge dislocations in nickel," *Physical Review*, vol. 147, no. 2, p. 495, 1966.

[105] S. Soltani, N. Abdolrahim, and P. Sepehrband, "Molecular dynamics study of self-diffusion in the core of a screw dislocation in face centered cubic crystals," *Scripta Materialia*, vol. 133, pp. 101–104, 2017.

[106] Y Yagodzinskyy, T Saukkonen, H Hänninen, F Tuomisto, S Barannikova, and L Zuev, "Effect of hydrogen on plastic strain localization in single crystals of nickel and austenitic stainless steel," in *Proceedings of the 2008 International Hydrogen Conference*, 2009, pp. 97–104.

[107] K. E. Atkinson and W. Han, *Elementary numerical analysis*. Wiley New York, 1985.

[108] J Lépinoux and L. Kubin, "Dislocation mechanisms and steady states in the cyclic deformation of facecentred cubic crystals," *Philosophical Magazine A*, vol. 54, no. 5, pp. 631–649, 1986.

[109] S. Xu, L. Xiong, Y. Chen, and D. L. McDowell, "Sequential slip transfer of mixed-character dislocations across $\Sigma 3$ coherent twin boundary in fcc metals: A concurrent atomistic-continuum study," *npj Computational Materials*, vol. 2, p. 15 016, 2016.

[110] W. M. Kays, *Convective heat and mass transfer*. Tata McGraw-Hill Education, 2012.

[111] W. Kays, M. Crawford, and B. Weigand, *Convective Heat & Mass Transfer W/ Engineering Subscription Card*, ser. McGraw-Hill series in mechanical engineering. McGraw-Hill Companies,Incorporated, 2005, ISBN: 9780072990737.

[112] J Čížek, M Janeček, T Vlasák, B Smola, O Melikhova, and D. SV, "The development of vacancies during severe plastic deformation," *Materials transactions*, vol. 60, no. 8, pp. 1533–1542, 2019.

[113] D. Setman, E. Schafler, E. Korznikova, and M. J. Zehetbauer, "The presence and nature of vacancy type defects in nanometals detained by severe plastic deformation," *Materials Science and Engineering: A*, vol. 493, no. 1-2, pp. 116–122, 2008.

[114] D. Raabe, *Computational Materials Science: The Simulation of Materials, Microstructures and Properties*. Wiley, 1998, ISBN: 9783527295418.

[115] J. R. Rice, "Tensile crack tip fields in elastic-ideally plastic crystals," *Mechanics of Materials*, vol. 6, no. 4, pp. 317–335, 1987.

[116] P. Sofronis and R. M. McMeeking, "Numerical analysis of hydrogen transport near a blunting crack tip," *Journal of the Mechanics and Physics of Solids*, vol. 37, no. 3, pp. 317–350, 1989.

[117] R. M. Latanision and R. H. Jones, *Chemistry and physics of fracture*. Springer Science & Business Media, 2012, vol. 130.

[118] Y. Fukai and H. Sugimoto, "Formation mechanism of defect metal hydrides containing superabundant vacancies," *Journal of Physics: Condensed Matter*, vol. 19, no. 43, p. 436 201, 2007.

[119] A Taylor and S. McDonald, "Void formation in proton and nickel irradiated 304 stainless steel," in *Radiation-Induced Voids in Metals*, USAEC Technical Information Center Oak Ridge, Tenn, 1972, p. 499.

[120] H. Brager, J. Straalsund, J. Holmes, and J. Bates, "Irradiation-produced defects in austenitic stainless steel," *Metallurgical Transactions*, vol. 2, no. 7, pp. 1893–1904, 1971.

[121] J. Stiegler, "Void formation in neutron irradiated metals," Oak Ridge National Lab., Tech. Rep., 1971.

[122] D. Tanguy, Y. Wang, and D. Connétable, "Stability of vacancy-hydrogen clusters in nickel from first-principles calculations," *Acta Materialia*, vol. 78, pp. 135–143, 2014.

[123] G. Leibfried and N. Breuer, *Point defects in metals I: introduction to the theory*. Springer, 2006, vol. 81.

[124] N. Metropolis, A. W. Rosenbluth, M. N. Rosenbluth, A. H. Teller, and E. Teller, "Equation of state calculations by fast computing machines," *The journal of chemical physics*, vol. 21, no. 6, pp. 1087–1092, 1953.

[125] W. K. Hastings, "Monte carlo sampling methods using markov chains and their applications," 1970.

[126] D. Vizoso, C. Deo, and R. Dingreville, "Scaling laws and stability of nano-sized defect clusters in niobium via atomistic simulations and statistical analysis," *Journal of Materials Science*, vol. 54, no. 22, pp. 14 002–14 028, 2019.

[127] M Ponga, M Ortiz, and M. Ariza, "A comparative study of nanovoid growth in fcc metals," *Philosophical Magazine*, vol. 97, no. 32, pp. 2985–3007, 2017.

[128] J. W. Corbett and L. C. Lanniello, *Radiation-induced voids in metals*. Atomic Energy Commission, 1972.

[129] D. Olander, U. S. E. Research, D. A. D. of Reactor Development, and Demonstration, *Fundamental Aspects of the Performance of Nuclear Reactor Fuel Elements*, ser. Fundamental Aspects of the Performance of Nuclear Reactor Fuel Elements. U.S. Energy Research and Development Administration, Office of Public Affairs, Technical Information Center, 1976.

[130] D. R. Mason, D. Nguyen-Manh, M.-C. Marinica, R. Alexander, A. E. Sand, and S. L. Dudarev, "Relaxation volumes of microscopic and mesoscopic irradiation-induced defects in tungsten," *Journal of Applied Physics*, vol. 126, no. 7, p. 075 112, 2019.

[131] I. Groma, "Link between the microscopic and mesoscopic length-scale description of the collective behavior of dislocations," *Physical Review B*, vol. 56, no. 10, p. 5807, 1997.

[132] A. El-Azab, "Statistical mechanics treatment of the evolution of dislocation distributions in single crystals," *Physical Review B*, vol. 61, no. 18, p. 11 956, 2000.

[133] S. Xia and A. El-Azab, "Computational modelling of mesoscale dislocation patterning and plastic deformation of single crystals," *Modelling and Simulation in Materials Science and Engineering*, vol. 23, no. 5, p. 055 009, 2015.

[134] S. Xia and A El-Azab, "A preliminary investigation of dislocation cell structure formation in metals using continuum dislocation dynamics," in *IOP Conference Series: Materials Science and Engineering*, IOP Publishing, vol. 89, 2015, p. 012 053.

[135] J Lepinoux and L. Kubin, "Dynamic organization of dislocation structures: A simulation," *Scr. Metall.;(United States)*, vol. 21, no. 6, 1987.

[136] N. M. Ghoniem and R Amodeo, *Computer simulaltion of dislocation pattern formation*. Trans Tech Publ, 1988, vol. 3.

[137] L. Kubin, *Dislocations, mesoscale simulations and plastic flow*. Oxford University Press, 2013, vol. 5.